Long-term evaluation of an organic-carbon permeable reactive barrier remediating mine-impacted groundwater and the potential of emulsified vegetable oil to increase treatment performance

by

Austin J. Miller

A thesis
presented to the University of Waterloo
in fulfillment of the
thesis requirement for the degree of
Master of Science
in
Earth Sciences

Waterloo, Ontario, Canada, 2024

© Austin J. Miller 2024

Author's Declaration

I hereby declare that I am the sole author of this thesis. This is a true copy of the thesis, including any required final revisions, as accepted by my examiners.

I understand that my thesis may be made electronically available to the public.

Abstract

Degradation of water resources by acid mine drainage (AMD) and metal contaminants from the oxidation of mine wastes that are improperly managed is a global environmental concern. An established economical and passive method for managing the transport of oxidation products in groundwater is the installation of an organic-carbon permeable reactive barrier (PRB) to promote the growth of sulfate reducing bacteria (SRB) and dissimilatory sulfate reduction (DSR) *in situ*. A detailed biogeochemical evaluation was conducted on a PRB remediating AMD from an abandoned Ni-Cu mine after 26 years of treatment, providing the first long-term evaluation of this technology. Pore-water concentrations of Ni decreased from 97μg L^{-1} to < 25 μg L^{-1} while Fe decreased by 402 mg L^{-1} (77% of mean influent) through the PRB. Pore-water SO_4 decreased by 1,243 mg L^{-1} (70% of mean influent) coinciding with an increase in alkalinity and pore-water $\delta^{34}S_{SO_4}$, suggesting DSR is actively occurring. There are distinctly different populations of putative SRB present within the sampled PRB material compared to the surrounding aquifer material. Low abundances of S and Fe oxidizing prokaryotes were detected, which may oxidize Fe-sulfide phases; re-mobilizing Fe and S or result in the formation of Fe(III) (oxy)hydroxide phases. A preponderance of S immobilized within the PRB is in the form of acid volatile sulfur with mineralogical investigations identifying FeS phases often replacing organic carbon in plant cellular material and framboidal pyrite. These results demonstrate that the PRB is still operating as designed with complex organic carbon compounds supporting a diverse microbial community that sustain rates of DSR to effectively precipitate Fe sulfides, decrease the acid potential of groundwater and immobilize contaminants. Column experiments were designed to evaluate the incorporation of emulsified vegetable oil (EVO) into solid-phase organic carbon through soaking and injection to promote and sustain treatment performance. Column effluent compositions demonstrate soaking organic-carbon in EVO resulted in high levels of Fe removal for the duration of observation (315 days). Moreover, an EVO injection re-established treatment after removal rates declined, providing a viable alternative to PRB replacement to maintain effective treatment system performance and extend PRB lifespan.

Acknowledgements

First and foremost, I would like to thank my advisors, Dr. David Blowes and Dr. Carol Ptacek, for this opportunity. Over the years I have appreciated your unwavering support and direction during challenges in research. Developing as a geochemist under your guidance has been incredibly empowering and something I will forever be grateful for. I would also like to thank my committee members; Dr. Laura Hug, Dr. Jenine McCutcheon, Dr. Thai Phan for your interest in my research and recommendations to improve my thesis.

It goes without saying that this thesis would not have been possible without the incredible group of talented people that make up GGR. To those who I have not met and come before me researching the Nickel Rim North site and PRBs, your work has been fundamental in shaping my research and provided countless solutions to problems I faced. Jeff Bain, I am grateful for the time you spent teaching me and our thoughtful conversations on how to make the science better. Dr. Eva Pakostova, the microbiology component of this project would not have been possible without you and I am thankful for all your time spent on the analyses and answering my questions. Sara Fellin, thank you for your support and guidance in the lab when I felt lost or I was trying to resurrect methods that had long been forgotten. Dr. David Wilson, thanks for the help in the field and everything else you did to support my work behind the scenes. Lisa Kester, Nikki Bell, and Meredith Miller, thank you for the administrative support. Joy Hu, thank you helping me find my way in 5007 and all for the analytical support. To all the graduate students, PDFs and CO-OPs who spent the time to offer guidance or had a hand in the many components of this project, I cannot thank you enough. In the greater TERRE-NET community I'd like to thank Dr. Joyce Mcbeth and Dr. Valerie Schoepfer at the University of Saskatchewan for being generous with their synchrotron time and teaching about data processing. I would also like to thank Samantha McGarry and Glencore for all the support of field and research efforts working on the Nickel Rim North PRB.

While COVID lockdowns stymied a traditional graduate school experience, many of you made my second stint in Canada as great as the first. I will always remember the welcoming and supportive community I experienced during my time at the University of Waterloo and I am grateful for the friendships I developed along the way. Finally, I would like to thank my family for their steadfast support in helping me to pursue my passion for geochemistry. Mom and Dad thank you for all the love and support. To my partner Emily, I am grateful every day for your devotion, patience, and the years of adventuring by my side that keep me grounded.

Table of Contents

Author's Declaration ii

Abstract iii

Acknowledgements iv

List of Figures vii

List of Tables xiv

List of Abbreviations xvi

Chapter 1 : *Introduction* 1

1.1 The Challenge of Acid Mine Drainage 1

1.2 Nickel Rim North Site Background 2

1.3 Bioremediation of Acid Mine Drainage Using Organic-Carbon Permeable Reactive Barriers 5

1.4 Secondary Mineral Phases Contributing to Contaminant Immobilization 10

1.5 Research Objectives 11

1.6 Experimental Approach 13

Organization 13

Chapter 2 : *Geochemistry and microbiology of a permeable reactive barrier for metal contaminants and acid mine drainage: 26 years of performance* 15

2.1 Introduction 17

2.1.1 Nickel Rim North Field Site Description 19

2.2 Methodology 20

2.2.1 Piezometer Installation 20

2.2.2 Sample Collection 20

2.2.3 Groundwater Analysis 21

2.2.4 Bulk Material Characteristics 22

2.2.5 DNA Extraction and Analysis 23

2.2.6 Total Carbon and Sulfur Analysis and Selective Sulfur Extraction 24

2.2.7 Mineralogy 24

2.2.8 Data Analysis 26

2.3 Results and Discussion 27

2.3.1 Treatment Performance of the Nickel Rim North PRB 27

2.3.2 Microbial Community Response to an Aging PRB 32

2.3.3 Long-term Mechanisms of Contaminant Immobilization and Stability.....39
2.3.4 Conclusions and Implications 44
Chapter 3 : Incorporation of Emulsified Vegetable Oil into Organic-Carbon Permeable Reactive Barriers for Treatment of Mine-Impacted Groundwater: Column Experiments 46
3.1 Introduction 48
3.2 Methodology 50
3.2.1 Column Design and Experimental Setup 50
3.2.2 Sample Collection 54
3.2.3 Analytical Methods 56
3.2.4 Microbial Characterization.....57
3.2.5 Solid-Phase Characterization 58
3.2.6 Data Interpretation.....59
3.3 Results 60
3.3.1 Column Flow Characteristics and EVO Mobility 60
3.3.2 Geochemical Conditions 60
3.3.3 Column Microbiology Characterization and Comparison 72
3.3.4 Solid-Phase Characterization 76
3.4 Discussion 80
3.4.1 Column Flow Conditions and EVO Mobility 80
3.4.2 Geochemical Conditions 81
3.4.3 Sulfur Biogeochemistry.....84
3.4.4 Metal Removal Mechanism 89
3.5 Implications.....91
Chapter 4 : *Conclusions and Recommendations*.....92
References 98
Appendix A : *Additional Data and Information Presented for Chapter 2* 115
Appendix B : *Additional Data and Information Presented for Chapter 3*.....139

List of Figures

Figure 1.1. A) Nickel Rim North field site location. B) Plan view map of the tailings impoundment and PRB in relation to Moose Lake. Transect B-B' is the location of research conducted in this thesis. C) Cross-section view of A-A' transect depicting the groundwater flow path through the PRB and areas of surface discharge. 4

Figure 2.1. Groundwater aqueous chemistry contours plots from Fall 2021 showing concentrations of SO_4, Fe, and Ni along the B'-B transect. Potential acidity was calculated for each water sampling point. Water sampling points measured and used for contouring are illustrated as open circles. 29

Figure 2.2. Groundwater chemistry contours from Fall 2021 of measured pH, alkalinity, DOC, and Eh in the Nickel Rim North PRB and surrounding aquifer along the B'-B transect. Water sampling points used for contours are illustrated as open circles. 31

Figure 2.3. A) Proportion of total reads for sulfate and/or sulfur reducing bacteria (SRB) and sulfur (SOP) and/or iron oxidizing prokaryotes (IOP) for cored material. B) Acid volatile sulfides concentration in dry sampled material from cores sampled in 2021. 36

Figure 2.4. A) Groundwater isotopic composition contour plots for both $\delta^{34}S_{SO_4}$ and $\delta^{34}S_{SO_4}$ from Fall 2021 sampling along the B-B' transect. B) Cross-plots of $\delta^{34}S_{SO_4}$ *vs.* $\delta^{34}S_{SO_4}$, $\delta^{34}S_{SO_4}$ *vs.* SO_4 and $\delta^{34}S_{SO_4}$ *vs.* SO_4. A simple linear regression for $\delta^{18}O_{SO_4}$ *vs.* $\delta^{34}S_{SO_4}$ was conducted with the line of best fit illustrated as a solid line and 95% confidence bands as dashed lines. The point in red is considered to be in 'apparent equilibrium phase' and not included in the linear regression. Standard delta notation reported as per mil (‰) deviations from Vienna Standard Mean Ocean Water (VSMOW) and Vienna Cañon Diablo Troilite (VCDT). 37

Figure 2.5. Bulk S XANES. A) S K-edge XANES of standards used for LCF fitting with vertical lines representing the maximum peaks of each standard. B) S K-edge XANES of sampled material. The vertical dashed lines correspond to the lines in A to allow for fingerprinting. 42

Figure 3.1. Schematic diagram of column experiment setup and design. Influent was pumped into the bottom of each column in an anaerobic glovebox. Profile pore-water and solid-phase

sampling ports were used to sample the columns over the course of the experiment. The lowest water sampling port was also used for EVO injection in EVOI. 53

Figure 3.2. pH, Eh, alkalinity, Ca, SO_4 and sulfide versus pore volumes (PV) in influent and effluent of the four column experiments. The dashed line at 40 PV indicates when the second injection of EVO occurred in the EVOI column. The influent and column effluents are differentiated by shape and color. 62

Figure 3.3. pH, Eh, alkalinity, and Ca in pore-water samples from CC, EVOI, EVOS1, and EVOS2 during three sampling events. The three sampling events are labeled according to the approximate pore volume (PV) of sampling and differentiated by different color shade and shape. Distance 0 cm represents the influent concentration and distance 40 cm represents the effluent concentration. 63

Figure 3.4. Concentrations of dissolved organic carbon (DOC), acetate, propionate, and formate in column influent and effluent. 64

Figure 3.5. Pore-water SO_4, sulfide, and $\delta^{18}O_{SO_4}$ and $\delta^{34}S_{SO_4}$ measurements from pore-water SO_4. Samples were collected along the length of each column during three sampling events with each plot representing a different geochemical parameter for each column. The sampling events for each column, labeled according to the approximate PV during sampling, are differentiated by both color and shape. Distance 0 cm represents the influent and 40 cm represents the effluent. 67

Figure 3.6. Influent water and column effluent Fe, potential acidity, and Ni. A positive potential acidity would indicate a net-acid potential with surface discharge while negative values indicate net-acid consuming potential. Each plot is a measured or calculated parameter with influent and effluents from each column differentiated by shape and color. 70

Figure 3.7. Pore-water Fe and Ni concentrations collected along the length of each column during three sampling events with each plot representing a different geochemical parameter and column. The sampling events for each column, labeled according to the approximate PV

during sampling, are differentiated by both color shade and shape. Distance 0 cm represents the influent and 40 cm represents the effluent. 71

Figure 3.8. A) Major phyla proportion of total reads (relative abundance >0.5 % of total reads) of samples collected at week 12. B) 2-dimensional non-metric multidimensional scaling (2D-NMDS) plots based on unweighted UniFrac and weighted UniFrac. In these plots the distance between any two points represents the difference between the two communities..... 74

Figure 3.9. A) Proportion of total reads of sulfate reducing bacteria (SRB) at the genus level. An asterisks indicates when genus level identification was not possible and merged higher taxa are used. Minor SRB < 0.5 % of total reads. B) Proportion of total reads of iron-(IOM)/ sulfur-(SOM) oxidizing microorganisms at the genus level. Minor IOM/SOM < 0.05 % of total reads. A solid black line represents the mean relative abundance of IOM/SOM in each column with 1 standard deviation from the mean indicated by dashed lines in A and B. C) Proportion of total reads of methanogens and methylogens at the genus level. Samples were collected at week 12. 75

Figure 3.10. Solid phase analyses of C and S from samples taken at the end of the experiment. Each analysis is differentiated by shape with the color used to differentiate columns and aid in comparison to water chemistry data. The mean concentrations are plotted when measured in replicate with error bars representing 1 standard deviation from the mean to provide an estimate of sample heterogeneity and analytical error. 77

Figure 3.11. Measured Bulk S K-edge X-ray adsorption near edge structure (XANES) of solid material collected after 12 weeks of treatment. Standards on the left were used in linear combination fitting. The max peak (whiteline position) is illustrated as a dashed line for FeS (a), pyrite (b), elemental S (c), cysteine (d), Na-sulfite (e), Na-thiosulfate (f), K-tetrathionate (g), gypsum (h), and ferrous sulfate (h). 79

Figure A1. The B-B' cross-section transecting the PRB and illustrating the groundwater sampling and core locations. The location of the PRB and sand material was constrained by lithologic characterization of the cored material and recorded dimensions during installation. Not illustrated is the bentonite clay cover above the PRB. 116

Figure A2. Heatmap of calculated charge balance percent error and saturation indices using PHREEQC and WATEQ4F database for potential reaction products. Groundwater samples are in order based on well nest location along the transect and depth in each well nest. Samples with no S^{2-} measurement are marked with an X in the sulfide species as these species are unconstrained. 117

Figure A3. Proportions of total reads of major genera (relative abundance > 0.5% of total reads) in duplicate samples. Higher taxa are marked with an asterisk. 118

Figure A4. Total sulfur, total reducible sulfur (TRS), acid volatile sulfur (AVS) total carbon and inorganic carbon measured in sub-sampled core material from the upgradient aquifer, PRB and downgradient aquifer. Samples where more than one measurement was made for a parameter, the mean is plotted and error bars represent one standard deviation. 124

Figure A5. Proportions of total reads of major phyla (relative abundance > 1.0% of total reads). Legend: [1]upstream aquifer, [2]PRB, [3]downstream aquifer. Mean relative abundance of unclassified bacteria on the phylum level accounted for 13.3% of the total amplicons. Archaeal DNA constituted for only 2.5 % of the total amplified 16S rRNA genes. 126

Figure A6. Proportions of total reads of major genera (relative abundance > 1.0% of total reads). Legend: [1]upstream aquifer, [2]PRB, [3]downstream aquifer. Higher taxa are marked with an asterisk when identification to the genus level was not possible. 127

Figure A7. Optical mineralogy and SEM of organic material. A) backscatter image of organic carbon material with reflective region along plant cell wall; B) elemental map of S in this region showing accumulation in plant cell wall and nodules likely indicative of pyrite framboids; C) elemental map of Fe showing accumulation along plant cell wall and nodules; D) SEM-EDX spectrum from a location along plant cell wall, and E) Pictomicrograph showing distribution of FeS phases concentrated along plant cell walls and pyrite framboids within organic material in a similar location. 132

Figure A8. Location of interest examined with XRF maps at SXRMB and S and Ni K-edge μXANES spectra. Elemental heat maps are shown with three zoomed in regions indicating hotspots and

locations where S and Ni μXANES spectra were collected. The S and Ni μXANES spectra are shown in the left and right below. Vertical lines in the S μXANES correspond to standards in Figure 2.6 A. Ni standards used in LCF fitting are shown. Region 3 had S phases mapped at different energies and full elemental maps developed for only a portion of the region. 133

Figure A9. Bulk Fe K-edge XANES. Standard spectra used for LCF are illustrated on the left (A) with vertical lines identifying for prominent peaks in these standards. Sample spectra are illustrated on the right (B) with the same vertical lines to allow for fingerprinting. 135

Figure A10. Optical mineralogy and SEM-EDX of S and Fe phases identified. Pictomicrograph (A) and backscatter image (B) illustrating the relationship between pyrite and an Fe-oxide phase as identified by EDX analysis (Fe-oxide phase (E) & pyrite phase (F)). Elemental maps of this same location are shown for S (C) and Fe (D). Below is a picotomicrograph (G) and backscatter image (H) of another location where FeS is present within the extracellular matrix in close association with organic carbon material. The elemental composition was confirmed with EDX (I). 137

Figure B1. A) Comparison of major phyla in duplicate samples from each column (relative abundance > 0.5 % of total reads). B) comparison of sulfate reducing bacteria total reads in duplicate samples from each column.....142

Figure B2. A) Cumulative discharge for each column measured gravimetrically over the experiment duration. B) measured Br tracer test breakthrough curves and influent concentrations for each column along with CXTFIT modeled results. 147

Figure B3. A) EVOI column after 50 ml EVO-influent mixture injected at beginning of the experiment. B) EVOI column after 100 ml EVO-influent mixture injected at the beginning of the experiment. Note the preferential flow through the column. C) Rapid migration of EVO to the upper portion of the EVOI column ~12 hours after injection. D) The EVOI effluent sample collection vessel with EVO clearly in the effluent after 1 day. 149

Figure B4. Column profile acetate concentrations. The sampling events for each column, labeled according to the approximate PV during sampling, are differentiated by both color shade and shape. Distance 0 cm represents the influent and 40 cm represents the effluent. 150

Figure B5. Profile sampling event pore-water SO_4 *vs.* residence time (t). These results were fit with different types of models to determine bulk SO_4 removal rates. The coefficient of determination describes (R^2) the fit of each model. 151

Figure B6. Raw counts of bulk S XANES spectra of samples collected from the column experiments during the experiment. 154

Figure B7. Saturation indices calculated for column effluent and influent samples using PHREEQC and the Minteq V4 database for secondary reaction products. Columns and influent are differentiated by color and shape. Samples with percent error > 20% (n = 5) and SI = -999.999 were not plotted. 155

Figure B8. Influent and effluent sample saturation indices calculated using the PHREEQC database and Minteq V4 database for siderite, gypsum, elemental S and sulfide phases. The columns and influent are differentiated by different colors and shape. Samples with percent error > 20% (n = 5) and SI = -999.999 were not plotted. 156

Figure B9. Column profile sampling saturation indices calculated using PHREEQC and Minteq V4 database for secondary reaction products. The three profile sampling events are plotted for each column and geochemical parameter. Within each plot sampling events are differentiated by shape and color shade. Samples with percent error > 20% (n = 5) and SI = -999.999 were not plotted. 157

Figure B10. Column profile sampling saturation indices calculated using PHREEQC and Minteq V4 database for reaction products. The three profile sampling events are plotted for each column and geochemical parameter. Within each plot sampling events are differentiated by shape and color shade. Samples with SI=-999.999 were not plotted. 158

Figure B11. Column profile sampling saturation indices calculated using PHREEQC and Minteq V4 database for sulfide phases. The three profile sampling events are plotted for each column and

geochemical parameter. Within each plot sampling events are differentiated by shape and color shade. Samples with SI = -999.999 were not plotted.....159

Figure B12. ($\delta^{34}S+10^3$)/($\delta^{34}S_O+10^3$) *vs.* fraction of remaining SO_4. $\delta^{34}S_O$ and $\delta^{34}S$ are the $\delta^{34}S$ of the influent and pore-water samples taken along the column length, respectively. The best-fit curves are used to calculate the instantaneous fractionation factor (α; Guo & Blowes, 2009). 160

Figure B13. Aqueous sulfate $\delta^{34}S$ and $\delta^{18}O$ cross-plots of samples collected from influent effluent and pore-water. Samples from CC, EVOI and EVOS columns are grouped in individual plots for comparison. Each column profile sampling event is represented by a different color and shape. Each sampling event was fit with a simple linear regression and equations of these fits are shown. 163

List of Tables

Table 3.1. Column experiment composition of the solid phase reactive material by volume %. The amount of solid phase reactive material (including bacterial inoculum) and EVO is indicated for each column. The reactive material density was determined from the solid phase reactive material mass (wet) and volume determined from the volume of material in the column. 51

Table 3.2. Influent solution aqueous geochemical composition. 54

Table A1. Total numbers of raw and effective sequences, OTU (operational taxonomic unit) counts, and alpha-diversity indices (Good's coverage, Chao's and Gini-Simpson's indexes). 120

Table A2. CRS and AVS standard recoveries. 123

Table A3. Bulk removal rates for SO_4 and Fe based on aqueous concentrations and estimated residence times. 125

Table A4. Mean proportions of total reads for genera of interest. Genera are separated into; sulfate reducing bacteria (SRB), sulfur- (SOP) and iron-oxidizing prokaryotes (IOP). 128

Table A5. Total reducible sulfur (TRS) bulk accumulation rates. 130

Table A6. Bulk S K-edge XANES Linear Combination Fitting. 131

Table A7. Linear combination fitting of S K-edge μXANES of samples collected. 134

Table A8. Bulk Fe K-edge XANES Linear Combination Fitting on sampled material from the PRB an downgradient aquifer. 136

Table A9. Ni K-edge μXANES LCF fittings of locations shown in figure A8. 138

Table B1. Mean moisture content of the reactive material components measured in triplicate..... 140

Table B2. Total numbers of raw and effective sequences, operational taxonomic unit (OTU). 144

Table B3. Sulfur XANES liner combination fitting results. 146

Table B4. Column experiment duration, flow parameters, and gravimetric pore volume measurements. 147

Table B5. CXTFIT modeling fits *vs.* observed values and calculated pore-water velocity, pore volume, porosity, residence time, and total pore volumes. 148

Table B6. Mean proportions of total reads of sulfate reducing bacteria in each test condition. EVOS1 and EVOS2 are combined into EVOS. 152

Table B7. Column moisture content summary statistics. 153

Table B8. Comparing the best linear combination fitting (LCFs) results of S XANES spectra for samples where pyrite was included in the best fit results. Spectra for standards used in LCF fitting are shown in Figure 3.11. 161

Table B9. Calculated instantaneous fractionation factor (α) and enrichment factor (ε) for different column pore-water sampling events using Rayleigh fractionation model (Guo & Blowes, 2009). The goodness-of-fit is described by the coefficient of determination (R^2). 162

List of Abbreviations

AMD	acid mine drainage
AMOVA	analysis of molecular variance
AVS	acid volatile sulfides
BAC	bacterial and archaeal community
CC	control column
CDE	convection dispersion equation
CF-EA-IRMS	continuous flow mass spectrometer
CLS	Canadian Light Source
CRS	chromium reducible sulfur
DNA	deoxyribonucleic acid
DOC	dissolved organic carbon
DSR	dissimilatory sulfate reduction
EDX	energy dispersive X-ray spectroscopy
EVO	emulsified vegetable oil
EVOI	EVO injection column
EVOS	EVO soaked columns (EVOS1 and EVOS2)
EVOS1	EVO soaked column 1
EVOS2	EVO soaked column 2
HDPE	high-density polyethylene
ICO-OES	inductively coupled plasma optical emission spectrometry
ICP-MS	inductively coupled plasma mass spectrometry
ID	inner diameter
IOM	iron-oxidizing microorganisms
LCF	linear combination fitting
LCFA	long chain fatty acids
OC	organic carbon
OTU	operational taxonomic unit
PE	polyethylene
PP	polypropylene
PRB	permeable reactive barrier
PV	pore volume
rRNA	ribosomal ribonucleic acid
SALP	slope of apparent linear phase
SEM	scanning electron microscope
SOM	sulfur-oxidizing microorganisms
SRB	sulfate reducing bacteria
SRBR	sulfate reducing bioreactor

SS	silica sand
SXRMB	soft x-ray microcharacterization beamline
TRS	total reducible sulfur
US EPA	United States Environmental Protection Agency
VCDT	Vienna Cañon Diablo Troilite
VSMOW	Vienna Standard Mean Ocean Water
XANES	X-ray adsorption near edge spectroscopy
XRF	X-ray fluorescence

Chapter 1: *Introduction*

1.1 The Challenge of Acid Mine Drainage

Mining is a cornerstone in the economic development of Canada and nations around the globe. Juxtaposing the benefits of jobs, community building and critical raw materials is an insidious legacy of water-resource contamination. Acid mine drainage (AMD) and the release of metal contaminants to groundwater and surface water bodies are a principal environmental concern associated with mining sulfide ore deposits for precious and base metals (Verburg et al., 2009). Mining sulfide ore deposits results in a massive accumulation of waste material in tailings impoundments and waste-rock piles containing residual ore and gangue sulfide minerals (Blowes et al., 2014). The accelerated oxidation of sulfide minerals by abiotic and biotic processes, when exposed to air and water, releases SO_4 and leaches metal(loids) into the pore-water. These oxidation products can then be transported into local groundwater and surface-water bodies (Lindsay et al., 2015).

Once AMD has begun it is challenging to mitigate, resulting in contamination until exhaustion of one or more of the reactants — a process that can persist for decades to centuries (España et al., 2005; R. H. Johnson et al., 2000; Moncur et al., 2014). Acid mine drainage mitigation strategies that limit exposure of mine wastes to oxidants, including O_2-gas diffusion barriers (*e.g.*, elevated water tables or soil covers), are most effective when applied prior to the onset of oxidation (Blowes et al., 2014). For abandoned mines, where oxidation is extensive, a transition to controlling contaminant fate and treating the AMD is often more pragmatic than source control methods (Blowes et al., 2014).

The cost to remediate abandoned and orphaned mines is estimated in the tens of billions of U.S. dollars in North America alone (Verburg et al., 2009). Treatment of AMD can be divided into active and passive approaches. Active treatment technologies employed to remediate AMD, such as chemical neutralization and pump-and-treat of contaminated groundwater, have high operating costs, limiting their wide-scale application to abandoned and orphaned mine sites (D. B. Johnson & Hallberg, 2005). Implementation of passive treatment systems has become an established approach to reduce cost and improve efficacy for mine site remediation while also reducing the environmental footprint of cleanup efforts (Adams et al., 2014). In the 1990s, permeable reactive barrier (PRB) technology was applied to sites with mine impacted groundwater and showed promise to be a long-term economic solution to prevent AMD (Benner et al., 1997). Study of this technology has continued with its increased use in remediation efforts over the last 26 years.

This chapter provides background information on the Nickel Rim North PRB, the first PRB installed at a mine site to treat AMD. More broadly, it examines the current state of research on PRB technology treating AMD at other sites. The chapter concludes with an overview of the research objectives of this thesis and its organization.

1.2 Nickel Rim North Site Background

The abandoned Nickel Rim North tailings impoundment is approximately 35 km northeast of Sudbury, Ontario in the eastern range of the Sudbury Igneous Complex (**Figure 1.1**). The local climate is predominantly cool and humid with a mean annual temperature of 4.1±1.0°C (mean ± standard deviation) and mean annual precipitation of 903.3 mm a^{-1} from 1981 to 2010. The Cu-Ni mine operated intermittently between 1929 and 1958, with mill tailings production and disposal occurring from 1953 to 1958 in a nearby lake and several narrow glacial valleys forming elevated tailings impoundments (R. H. Johnson et al., 2000).

Field studies were conducted that focused on the largest tailings impoundment and surrounding aquifer (**Figure 1.1)**. R. H. Johnson et al. (2000) characterized the pore-water geochemistry and mineralogy of the tailings. Ribet et al. (1995) characterized the mineralogy of the tailings and mobility of metals in oxidized tailings under different redox conditions. McGregor and Blowes (2002) focused on characterizing the hardpan layers found within the oxidized tailings from secondary mineral phases. Microbial populations within the tailings and aquifer were evaluated using most probable number (MPN) determinations (Benner et al., 2000). Bain (1996) characterized the contaminant plume within the aquifer. Bain et al. (2000) developed a reactive transport model of the tailings and aquifer to validate the proposed geochemical conceptual models and predict future plume development. Doerr et al. (2005) characterized the aquifer materials and the distribution of metals.

The Nickel Rim North tailings impoundment pore-water has zones with acidic or circumneutral pH, attributed to carbonate mineral dissolution and acid neutralization (R. H. Johnson et al., 2000). Total S in unoxidized tailings varies by an order of magnitude from 0.5 to 5 wt. % (mean of 4.5 wt. %). Pyrrhotite ($Fe_{(1-x)}S$) is the dominant sulfide mineral (> 98%) with most containing Ni (R. H. Johnson et al., 2000; Ribet et al., 1995). Minor amounts of chalcopyrite ($CuFeS_2$), pentlandite $(Fe,Ni)_9S_8$, pyrite (FeS_2) and marcasite (FeS_2) are also present (R. H. Johnson et al., 2000; Ribet et al., 1995) and can leach toxic metal constituents incorporated into their structure into pore-water upon dissolution.

Vertical groundwater recharge and oxygen diffusion gradients have resulted in oxidative weathering and distinct geochemical zones that are controlled by biotic and abiotic processes (Lindsay et al., 2015). Pyrrhotite can be abiotically and microbially oxidized (Benner et al., 2000; Lindsay et al., 2015). The complete oxidation of pyrrhotite by O_2 can be expressed by the reaction (Nicholson & Scharer, 1994):

$$Fe_{(1-x)}S + (2 - \frac{1}{2}x)O_2 + xH_2O \rightarrow (1-x)Fe^{2+} + SO_4^{2-} + 2xH^+ \quad [1]$$

In the acidic conditions found in the upper portion of the tailings at Nickel Rim, Fe(III) remains soluble and becomes the primary oxidant of pyrrhotite (Janzen et al., 2000; Lindsay et al., 2015):

$$Fe_{(1-x)}S + (8 - 2x)Fe^{3+} + 4H_2O \rightarrow (9-3x)Fe^{2+} + SO_4^{2-} + 8H^+ \quad [2]$$

In the presence of excess O_2, which occurs in the near surface environment, Fe(II) can be oxidized and undergo hydrolysis precipitating Fe(III) (oxy)hydroxides ($Fe(OH)_3$; Lindsay et al., 2015):

$$Fe^{2+} + \frac{1}{4}O_2 + \frac{5}{2}H_2O \rightarrow Fe(OH)_{3(s)} + 2H^+ \quad [3]$$

Biotic and physiochemical processes can also influence the rate of Fe sulfide oxidation. Biotic oxidation of Fe and S can greatly increase the rate of oxidation and the release of metal(oid)s into pore-water (Blowes et al., 2014; Lindsay et al., 2015). An abundance of S-oxidizing microorganisms and Fe-oxidizing microorganisms have been detected in the Nickel Rim North tailings (Benner et al., 2000). The extensive precipitation of secondary minerals gypsum ($CaSO_4 \cdot 2H_2O$), goethite (α-FeO(OH)) and jarosite ($KFe_3(SO_4)_2(OH)_6$) have resulted in discontinuous hardpan layers. These layers can limit O_2 diffusion and water infiltration due to their reduced permeability (McGregor & Blowes, 2002).

The H^+ released through oxidation reactions is neutralized by dissolution and precipitation of primary and secondary minerals as groundwater flows downward and laterally through the tailings impoundment. From the surface to the active zone of sulfide oxidation, pore-water has low pH values between 2.1 to 3.5 attributed to the dissolution of jarosite to ferrihydrite or goethite (R. H. Johnson et al., 2000). In a vertical profile of the tailings there are abrupt transitions in pH, with approximate values of 3.0, 4.1, 5.6, 6.7 (R. H. Johnson et al., 2000). Between each transition, stable pH zones controlled by the sequential dissolution of acid-neutralizing minerals Fe(III) (oxy)hydroxides, gibbsite ($Al(OH)_3$), siderite ($FeCO_3$), and calcite ($CaCO_3$; R. H. Johnson et al., 2000). Together these dissolution and precipitation reactions control the concentrations of dissolved metals that are released to the underlying aquifer. These pH fronts migrate in the direction of groundwater flow over time (R. H. Johnson et al., 2000).

The tailings impoundment was deposited in a bedrock valley over an unconfined aquifer composed of glacio-fluvial deposits of silty fine quartz-feldspar sand with localized pockets of gravel- to boulder-sized material and peat. The aquifer is continuous beneath the waste-rock tailings dam and extends 130 m downgradient to Moose Lake (**Figure 1.1B**). Hydrogeologic modeling suggests that downstream of the waste-rock tailings dam, 50% of the water derived from the tailings impoundment is discharged to the surface where AMD is observed (Bain et al., 2000). The remaining water forms a contaminant plume which is migrating through the narrow bedrock valley. Groundwater velocities are ~15-16 m a^{-1} (Bain, 1996; Benner et al., 1997). Previous investigations of the groundwater plume flowing from the tailings into the aquifer identified high concentrations of SO_4 (2,500-5,200 mg L^{-1}), Fe (250-1,350 mg L^{-1}), and Ni (0.12-30 mg L^{-1}) with a pH of 2.8-5.9, and <1 to 60 mg L^{-1} alkalinity (as $CaCO_3$; Bain, 1996; Benner et al., 1999).

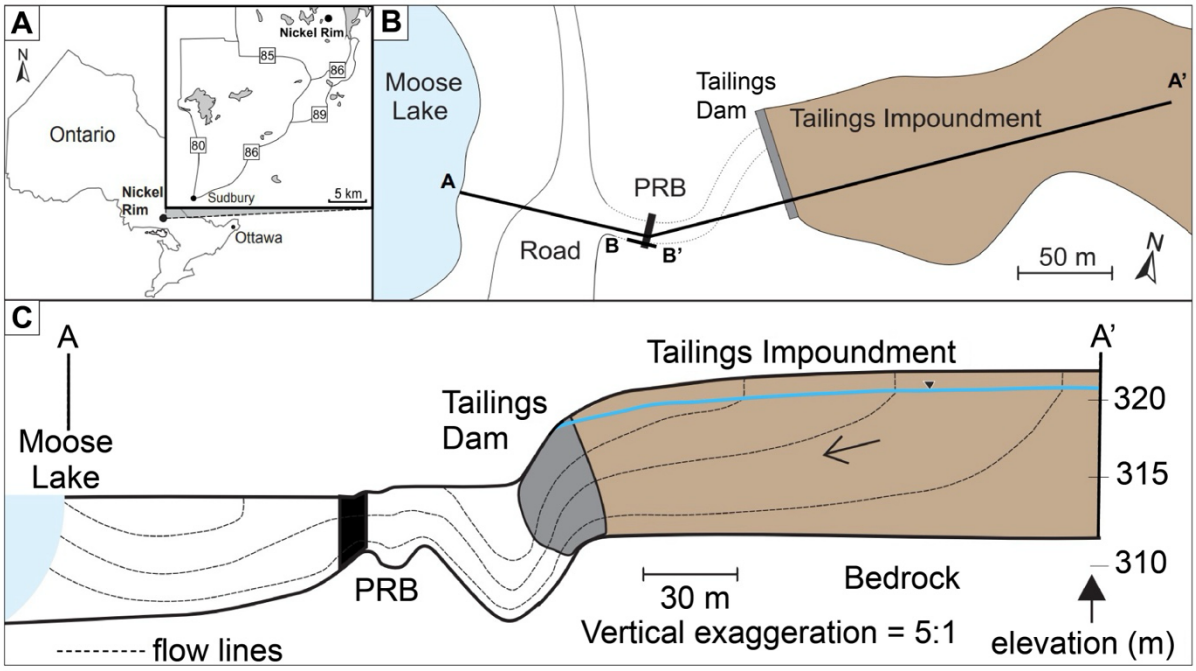


Figure 1.1. A) Nickel Rim North field site location. B) Plan view map of the tailings impoundment and PRB in relation to Moose Lake. Transect B-B' is the location of research conducted in this thesis. C) Cross-section view of A-A' transect depicting the groundwater flow path through the PRB and areas of surface discharge.

1.3 Bioremediation of Acid Mine Drainage Using Organic-Carbon Permeable Reactive Barriers

In the summer of 1995, the first field-scale PRB treating mine impacted groundwater was installed within Nickel Rim North aquifer to treat this contaminant plume (Benner et al., 1997). Permeable reactive barriers treating AMD are often designed to make use of the natural hydrogeologic gradient and promote biologically mediated sulfate reduction *in situ* through the installation of a zone of permeable organic carbon intersecting the contaminant plume migration pathway (Blowes et al., 2000). Sulfate reducing bacteria (SRB) rely on the anaerobic metabolic process of dissimilatory sulfate reduction (DSR) which couples the oxidation of organic carbon with the reduction of sulfate to sulfide for metabolic growth (Rabus et al., 2013). The diverse assemblage of bacteria that are capable of DSR rely on a variety of low-molecular-mass organic compounds or H_2. For instance, the simplified expression for DSR using lactate, a common growth medium, can be represented as (Rabus et al., 2013):

$$2CH_3CHOHCOO^- + 3SO_4^{2-} + 2H^+ \rightarrow 6HCO_3^- + 3H_2S \qquad [3]$$

As identified by Tuttle et al. (1969), AMD remediation systems can rely on the microbial production of S^{2-} species in the presence of dissolved Fe(II) to rapidly precipitate insoluble Fe sulfide mineral phases (Herbert et al., 2000):

$$H_2S + Fe^{2+} \rightarrow FeS + 2H^+ \qquad [4]$$

Similar sulfide precipitation reactions may occur with other metal contaminants including As, Cd, Cu, Ni, Pb, and Zn (Benner et al., 1999). The increase in alkalinity from DSR can result in the precipitation of carbonate minerals in the PRB or downgradient aquifer which improves the buffering capacity of the aquifer (Benner et al., 1999; Doerr et al., 2005).

In situ treatment exploits the decoupled nature of AMD generation and results in contaminant plume treatment prior to Fe(II) oxidation. This technology can improve treatment efficiency due to pH conditions more conducive to microbial sulfate reduction compared to other passive remediation systems that rely on DSR after surface discharge (*i.e.,* anaerobic wetlands, bioreactors). Moreover, *in situ* treatment is less susceptible to seasonal temperature swings in colder climates that can greatly affect the rate of DSR and treatment performance (Angai, 2020; Benner et al., 2002).

The Nickel Rim North PRB was installed ~70 m downgradient from the tailings impoundment in a narrow zone of the bedrock valley. This location was selected to minimize the cost of material for installation and optimize treatment of mine-impacted groundwater (Benner et al., 1997). A trench was excavated to bedrock using a cut-and-fill technique and refilled with a homogenized mixture of gravel

(50 % by vol.) and organic carbon composed of leaf compost (20% vol.), municipal compost (20% vol.), and wood chips (10% vol.; Benner et al., 1997).

Investigations of the Nickel Rim North PRB observed high rates of removal of SO_4 (2,000-3,000 mg L^{-1}), Fe (270-1,300 mg L^{-1}), and Ni (30 mg L^{-1}) over the first 22 months of operation (Benner et al., 1997, 1999). Enumeration of the microbial populations in the aquifer and PRB using most probable number (MPN) determinations revealed elevated populations of SRB within the PRB and downgradient aquifer compared to the aquifer material upgradient (Benner et al., 2000). Further indications of treatment through DSR include the concomitant increase in dissolved S^{2-} and enrichment in pore-water $\delta^{34}S_{SO_4}$, which accompanied the decrease in dissolved SO_4 concentration (Benner et al., 1999).

Permeable reactive barriers composed of solid phase organic carbon have a finite treatment lifespan. Over the first three years, the Nickel Rim North PRB rate of SO_4 removal decreased by 30% and the rate of Fe removal decreased by 50%. These decreases were attributed to a decrease in the availability of labile organic carbon (Benner et al., 2002). Depletion of the reactive organic component is often cited as the cause of performance loss in treating AMD using bioremediation and occurs well before the theoretical capacity of the treatment system (Benner et al., 2002; Blowes et al., 2000; Guo & Blowes, 2009; Neculita et al., 2007). Although the mass of organic carbon included in the Nickel Rim North could theoretically sustain treatment on the order of centuries (Benner et al., 1999), an initial estimate for the treatment system lifespan of the Nickel Rim North PRB was conservatively placed at 15 years based on the long-term performance of column experiments (Benner et al., 1999, Waybrant et. al, 2002).

The Nickel Rim North PRB utilizes a mixture of organic carbon of varying complexity. Wood chips, composed of cellulose, were included to provide a long-term source of organic carbon for DSR (Benner et al., 1997). Sulfate reducing microorganisms cannot utilize complex organic carbon such as cellulose and lignin directly. Growth of SRB and the rate of DSR can be limited by depletion of the initial pools of low molecular weight organic compounds (Hemsi et al., 2005; Logan et al., 2005). As a result, SRB require synergistic relationships with a microbiome of methanogens, fermenters and cellulolytic anaerobes that degrade macromolecular structures to provide the substrate for SRB to perform DSR and sustain treatment (Logan et al., 2005). In a series of column experiments the long-term rate limiting step in treatment was determined to be cellulolysis (Logan et al., 2005). Similarly, the population of fermentive acid producing bacteria was found to be small compared to the population of SRB when the performance of an organic carbon treatment column decreased (Guo &

Blowes, 2009). Extrapolating the results from column experiments may not be valid due to the complexities associated with implementation in a field setting. Given differences in temporal and spatial scale of a field-based PRB, the microbial communities present after decades of treatment need to be evaluated to determine if DSR is still the primary terminal electron accepting pathway and if the availability of labile carbon has limited treatment.

The current conceptual model of how a PRB operates is that SO_4 reduction is a uni-directional process resulting in the production of sulfide and precipitation of sulfide minerals. In a biologically mediated system, the interplay of reactions utilizing Fe, S, C and other toxic metals is complex. Studies in other natural environments have revealed that the S^{2-} from DSR is often cycled back to SO_4 through various pathways (Findlay & Kamyshny, 2017; Mills et al., 2016). Abiotic and biotic S oxidation can result in a great variety of S intermediate species that have rapid turnover rates making their quantification challenging (Findlay & Kamyshny, 2017). Determining if S cycling is occurring in a PRB has important implications for the refinement of the biogeochemical conceptual model of treatment and understanding of the mechanisms of contaminant immobilization and mineral stability.

One tool that has gained favor in tracking cryptic S cycling is the paired use of O and S isotopes from aqueous SO_4 (Antler et al., 2013; Mills et al., 2016). Intermediate S species can exchange O isotopes with water or if sulfide is re-oxidized to SO_4, the O molecules incorporated are to some degree in isotopic equilibrium with water (Mills et al., 2016). Comparisons of the relative change in $\delta^{34}S_{SO_4}$ to $\delta^{18}O_{SO_4}$ can indicate the importance of these back reactions (Mills et al., 2016). In the ideal condition of a PRB, there is limited to no S cycling and $\delta^{34}S_{SO_4}$ increases due to DSR with limited increase in $\delta^{18}O_{SO_4}$. If all S is recycled back to SO_4, then $\delta^{18}O_{SO_4}$ would increase while $\delta^{34}S_{SO_4}$ would remain consistent. Conditions within a PRB may be between these two end-members if only some S cycling is occurring.

At present the number of case studies on PRBs treating groundwater containing high concentrations of dissolved metals and SO_4 consistent with an AMD environment is limited. Studies on the treatment performance of the PRBs installed have demonstrated mixed results with inadequate treatment in systems with high groundwater velocities. An organic carbon PRB, installed at a historic ore concentrate storage facility in Vancouver, British Columbia, Canada was very effective at removing Cd, Cu, Ni and Zn over the first 21 months of monitoring (Ludwig et al., 2002). Higher rates of removal were observed in the lower portion of the PRB where SO_4 reducing conditions were more effectively maintained. A pilot scale mixed ZVI-organic carbon PRB was installed at a former phosphate fertilizer plant with a contaminant plume characterized by low pH, high concentrations of

SO_4, and metal contaminants from unspent pyrite used for sulfuric acid generation (Ludwig et al., 2009). The PRB was still very effective after 42 months with near complete removal of Al, As, Cd, Fe, Ni, Pb, and Zn (Ludwig et al., 2009).

Poor site hydraulic characterization prior to installation has been observed to be a common mechanism of failure in PRBs (Henderson & Demond, 2007). In Aznalcóllar, Spain a series of organic carbon PRB modules were installed to remediate both acidity and metals entering the groundwater after an accidental spill of AMD and pyritic sludge (Gibert et al., 2011). Study of this PRB system over the first 36 months revealed the development of preferential flow which limited treatment performance. In addition, further study of the surrounding aquifer demonstrated the initial stratigraphic conceptual model was over-simplified and the PRB failed to intercept the entirety of the contaminated aquifer. Sulfate reducing conditions were observed in the lower portion of the PRB where groundwater retention times were longer. However, preferential groundwater flow through the upper portion primarily composed of limestone likely limited treatment. Moreover, the thickness of the PRB was limited in relation to the groundwater flow velocity resulting in a residence time of 1-2 days, which may have hindered contaminant remediation using DSR. In areas where groundwater flowed through the PRB, the geochemical results suggest a proclivity for neutralizing pH and sequestering heavy metals with mean removal percentages for Al, Zn, and Cu being 80%, 47%, and 76% respectively (Gibert et al., 2011).

In Shilbottle, Northumberland UK an organic carbon PRB was installed as part of a larger treatment system remediating contaminated acidic groundwater containing high concentrations of dissolved Fe, Al, and SO_4 from mine waste piles (Jarvis et al., 2006). The PRB removed 50% of the Fe and 40% of the SO_4 during the first 24 months of operation. There was limited increase in pH and the PRB did not neutralize the acidic influent (Caraballo et al., 2010). Study of the Shilbottle PRB over five years revealed limited precipitation of reduced species with observed Fe phases primarily being goethite, schwertmannite ($Fe_{16}(OH, SO_4)_{12\text{-}13}O_{16}\cdot 10\text{-}12H_2O$) and pyrite (Caraballo et al., 2010). Limited residence time (10 to 40 hours) within the PRB was considered to be the primary limitation on the development of reducing conditions (Caraballo et al., 2010).

Sites with AMD often require remediation to continue for decades to meet environmental compliance requirements. Review of published organic carbon PRB case studies reveals the current temporal scale of observations is short compared to the treatment system lifespans. Long-term study will help determine mechanisms of failure that can be addressed to improve future design iterations. While early investigations were successful in demonstrating the utility of the PRB technology treating

AMD, the overall success and commercial value of this technology is a direct result of its long-term performance.

Evaluations of organic carbon PRBs on a longer timescale are needed to make more accurate estimates of treatment system lifespan at future sites. Machinery mobilization, reactive material, material emplacement and the proper disposal of used reactive material can add significant life-cycle costs (ITRC, 2011). Lifespan estimates are needed to more accurately predict the frequency of material replacement or replenishment to meet remediation goals. This information will help constrain the overall cost of a treatment system for a more balanced comparison to other remediation technologies.

Decades of research have been conducted to identify reactive organic carbon sources that can sustain long-term treatment performance. For passive systems, research has primarily focused on solid phase reactive media such as plant material, manure, and ZVI where the reactive media will eventually be exhausted from microbial consumption (Neculita et al., 2007). Another method of PRB treatment is through the injection of soluble substrates comprised of simple labile organic carbon (*e.g.,* lactate, butyrate, propionate, acetate, molasses, and refined sugars) that can be replenished to sustain treatment performance (ITRC, 2011). The use of these substrates is inherently a more costly and active approach due to the need for regular injections. These treatment systems can be susceptible to issues of clogging or heterogenous treatment zones where treatment is limited to the injection site due to its rapid utilization by microbes (Li et al., 2009).

The use of vegetable oil has shown great promise in anaerobic bioremediation of organic contaminants, nitrate, U and AMD (Hunter, 2001; Lindow & Borden, 2004; Watson et al., 2013). Injections of emulsified vegetable oil (EVO) can provide a complex organic carbon source that can migrate before being broken down for bioremediation. Column experiments have demonstrated EVO is very effective in treating AMD when injected into tailings material as an organic amendment (Lindow & Borden, 2004) but its effectiveness when combined with other organic carbon sources in a PRB has not been fully evaluated. In addition, while used at some sites as a method of prolonging PRB treatment lifespan (ITRC, 2011), there are no published studies on the ability of EVO to re-establish and sustain treatment performance in an older PRB system. Application of EVO to PRB technology treating AMD may provide a viable method to sustain treatment performance over the long-term without incurring the high cost of more active injection systems or complete barrier replacement.

1.4 Secondary Mineral Phases Contributing to Contaminant Immobilization

Immobilization of metal contaminants within an organic carbon PRB is primarily the result of precipitation reactions. Precipitation of sparingly soluble sulfide minerals under anaerobic conditions results in low dissolved metal concentrations, providing a stable mechanism of contaminant immobilization (Blowes et al., 2000). Herbert et al. (2000) found that during the first two years of treatment acid-volatile sulfides, an operationally defined group of amorphous Fe monosulfides, mackinawite (FeS) and greigite ($Fe^{2+}Fe^{3+}{}_2S_4$), were the primary sulfide mineral phases within the PRB at Nickel Rim North. X-ray diffraction revealed disordered mackinawite had precipitated within the barrier (Herbert et al., 2000). Chemical extractions to quantify different Fe sulfide species suggest the accumulation of pyrite made up less than 25% of the total reduced inorganic S and was more prominent in the front of the PRB where oxidizing agents may have contributed to pyrite formation (Herbert et al., 2000).

The mineralogical characteristics of Fe sulfides present within a PRB have important implications for the long-term stability of immobilized contaminants. Mackinawite is often viewed as a precursor to greigite and pyrite (Guo & Blowes, 2009; Jambor et al., 2005). Changes in the biogeochemistry of the PRB over time and cycling of S and Fe may drive this transition through a variety of pathways (Hunger & Benning, 2007; Rickard & Luther, 2007; Wan et al., 2017) that may or may not result in continued retention of toxic metal contaminants (Swanner et al., 2019).

A secondary Fe sink is thought to be the precipitation of siderite as thermodynamic calculations of early aqueous geochemical data from the Nickel Rim PRB and column experiments also suggest siderite is near saturation (Amos et al., 2004; Benner et al., 1999; Waybrant et al., 2002). Reactive transport modeling of organic PRB column experiments revealed that siderite may outcompete the precipitation of mackinawite due to a faster rate of precipitation when calcite is present within the reactive material (Amos et al., 2004). Compared to Fe sulfide minerals, precipitation of siderite is a less desirable immobilization mechanism due to its relatively higher solubility and dissolution susceptibility to changes in pH, Fe, or carbonate concentration.

A mineralogical study for the Nickel Rim PRB six years after installation identified Fe sulfides replacing organic carbon and framboidal pyrite with minor components of iron oxides and native Fe. A notable difference compared to earlier inferences is the lack of secondary carbonate minerals. Siderite was only observed incorporated into fragmented Fe(III) (oxy)hydroxides (Jambor et al., 2005). Studies that have investigated other PRBs have observed Fe(III) (oxy)hydroxides and calcite precipitation as primary mechanisms of contaminant attenuation in environments in which sulfate

reduction is not thermodynamically favorable (Caraballo et al., 2010; Gibert et al., 2011). The Nickel Rim North PRB mineralogy appears to be dynamic as a result of the biogeochemical conditions, requiring long-term evaluation to refine conceptual models.

Application of new spectroscopic techniques will allow for a refined understanding of the controlling mechanisms for Ni immobilization. Geochemical modeling of early aqueous geochemical results from the Nickel Rim North PRB suggest slightly supersaturated conditions with respect to millerite (NiS; Benner et al., 1999). Similar mineral saturation conditions were found for Cu and Zn, likely resulting in the precipitation of chalcopyrite and sphalerite (ZnS), respectively. Nickel can also be incorporated into the Fe sulfide mineral structure during precipitation and be immobilized (Morse & Arakaki, 1993). Mineralogical observations identified Ni within the Nickel Rim North PRB is primarily found as native Ni (Ni) with occasional association of an Fe-bearing Ni sulfate and Ni sulfate-phosphate phases (Jambor et al., 2005). The actual processes of immobilization of Ni within an organic carbon PRB remain unresolved.

The initial contaminant attenuation mechanisms within the Nickel Rim North PRB may give way to other geochemical reactions that result in the long-term immobilization of contaminants in more stable forms or release back into the environment. Further investigation of the mineralogy within the PRB is important to determine the mineralogical phases present within the PRB and the contaminant stability after 26 years of treatment.

1.5 Research Objectives

The primary goals of this thesis are to use a multi-faceted approach to evaluate the current performance, biogeochemistry and long-term contaminant control mechanisms in the PRB at Nickel Rim North and evaluate different methods of incorporating EVO into an organic carbon PRB to extend the effective treatment lifespan. The working hypotheses and research objectives have been organized based on the following research questions:

1. Is the Nickel Rim North PRB treating AMD effectively after 26 years and if not, what are the mechanisms of failure?
2. What biogeochemical processes are occurring within the PRB?
3. How are the contaminants immobilized within an organic carbon PRB and will they remain stable?

4. Will the addition of EVO through soaking or injection into the reactive organic mixture improve treatment performance of the PRB or affect the mechanisms of contaminant immobilization and microbial communities present?
5. Can PRB treatment performance be re-established with an injection of EVO?

The working hypothesis for question one, is that the PRB at Nickel Rim North has become ineffective in treating AMD because of preferential flow through the PRB and a decreased rate of DSR. The effectiveness of the PRB will be evaluated using traditional geochemical measurements. Potential failure through preferential flow and decreased treatment rate will be tested through the development of cross-contour plots and bulk treatment rate calculations, respectively.

The working hypothesis for question two is that heterogenous flow has resulted in localized redox gradients throughout the PRB as a result of active cycling of S and Fe. The objective of this thesis component is to refine the biogeochemical conceptual model of the PRB treating AMD. Bacterial and archaeal communities will be interrogated through the extraction of microbial DNA followed by 16S mRNA high throughput amplicon sequencing and statistical approaches. Biogeochemical processes will be identified using traditional aqueous geochemistry and isotopic measurements of S and O in aqueous SO_4.

The working hypothesis of question three is that contaminants will be immobilized within Fe(III) (oxy)hydroxides and pyrite that should remain stable. Primary mechanisms of metal immobilization within the PRB will be identified using a combination of solid-phase bulk geochemical analysis, extractions, optical mineralogy, and spectroscopic techniques. The spatial distribution of immobilized contaminants and mineralogical phases throughout the PRB will be determined. The stability of mineralogical phases will be evaluated using saturation indices calculated using geochemical speciation modeling of the aqueous geochemical results.

The working hypothesis for question four is that additions of EVO to the organic reactive mixture through both injection and soaking will improve treatment performance. Changes to the microbial communities are expected with the addition of EVO but the mechanisms of contaminant immobilization are expected to remain consistent with what has been observed in solid-phase organic carbon PRBs. The addition of EVO will be investigated through four treatment column experiments with evaluation focused on treatment performance, microbial response, characterization of contaminant immobilization mechanisms, and EVO mobility.

The working hypothesis for question five is that an injection of EVO into the reactive media will re-establish treatment performance. This will be investigated through a second EVO injection after treatment performance declines in the EVO injection column and monitoring the effluent aqueous geochemistry.

1.6 Experimental Approach

The Nickel Rim North PRB study was initiated with the development of a sampling plan informed by a literature review of the previous studies conducted on the PRB and surrounding aquifer (Bain et al., 2000; Benner et al., 1997, 1999, 2000, 2002; Herbert et al., 1998, 2000; Jambor et al., 2005; Mayer et al., 2006; Williams et al., 2007). An initial coring investigation, conducted by others in 2018, determined the location of the PRB within the aquifer. A set of core samples was collected for microbial and mineralogical analysis in 2019 along with the installation of several well nests. Work resumed on-site after delays and site closures due to the COVID-19 pandemic in fall 2021. With a better understanding of the PRB boundaries from previous coring efforts, geologic cores were collected and drive point piezometers were installed to develop a sampling network that traversed the PRB. Pore-water was sampled and analyzed to characterize the changes in geochemical conditions through the PRB, biogeochemical processes occurring, and treatment efficacy. These aqueous geochemical results were used for geochemical modeling using PHREEQC. Solid phase material from the cores was sampled and analyzed for microbiology, geochemistry, and mineralogy.

The EVO column experiment study began with a literature review on methods to prolong treatment performance in PRBs. Four column experiments were designed to evaluate the potential treatment performance benefits of incorporating EVO through soaking and injection in an organic carbon PRB. A second injection of EVO was applied to the EVO injection column after breakthrough in Fe was observed in column effluent to evaluate the potential for re-establishing treatment performance in an organic carbon PRB. Pore-water and effluent samples were analyzed to evaluate treatment performance and the geochemical conditions within the columns. These data were used in geochemical modeling with PHREEQC. Reactive material from these columns was investigated to compare the microbiology, mineralogy and geochemistry under different treatment conditions.

Organization

The thesis is composed of four chapters including; an introduction, two separate research chapters organized as research papers that address the main research objectives, and a concluding chapter

which summarizes the research results. Chapter two focuses on the field-based investigation to evaluate the Nickel Rim North PRB. The chapter describes the fieldwork completed, aqueous geochemistry, solid phase geochemical and microbial characterization of the treatment system. Chapter three describes four column experiments evaluating the incorporation of EVO into an organic carbon PRB through soaking and injection. The chapter describes the aqueous geochemical results from both pore-water and effluent, solid-phase geochemical analyses, and microbial community characterization for different test conditions. Chapter four concludes the thesis with a summation and synthesis of the research findings and recommendations for future work.

Chapter 2: *Geochemistry and microbiology of a permeable reactive barrier for metal contaminants and acid mine drainage: 26 years of performance*

Executive Summary

The long-term performance of an organic-carbon permeable reactive barrier (PRB), treating mine-impacted groundwater from an abandoned Ni-Cu mine, was evaluated 26 years after installation. Groundwater concentrations of Ni decreased from up to 255 μg L^{-1} (104 μg L^{-1} mean) to < 25 μg L^{-1} while Fe concentrations decreased by 402 mg L^{-1} (77% of mean influent) through the PRB. Groundwater SO_4 concentrations decreased by 1,243 mg L^{-1} (70% of mean influent) coinciding with an increase in groundwater SO_4 $\delta^{34}S$, suggesting dissimilatory sulfate reduction (DSR) is actively occurring. Groundwater removal rates of Fe and SO_4 are comparable to removal rates after 38 months of treatment suggesting very little, if any, decline in treatment performance occurred over two decades of treatment. Groundwater geochemical results suggest the treatment system lifespan estimate requires readjustment beyond an initial prediction of 15 years. Microbial community characterization using 16 rRNA DNA extraction indicates the presence of distinctly different populations of putative sulfate reducing bacteria (SRB) within the sampled PRB material compared to the surrounding aquifer material. Low abundances of S- and Fe-oxidizing prokaryotes were detected, which may contribute to re-mobilization of Fe and S or formation of Fe(III) (oxy)hydroxide phases. Solid phase geochemical extractions and mineralogical evaluation of sampled PRB material identified FeS precipitation as the dominant mechanism for contaminant immobilization with minor components of Fe(III)-oxide phases and framboidal pyrite (FeS_2). The close association and incorporation of FeS in more complex organic carbon structures suggests these reactive materials serve a dual purpose in both promoting the continued growth and activity of DSR and maintaining long-term contaminant stability.

2.1 Introduction

Low-cost, long-term passive treatment technologies are indispensable to remediate the insidious legacy of water contamination and acid mine drainage (AMD) from orphaned and abandoned mine sites. Unmanaged waste rock piles and tailings deposits can expose sulfide minerals to water and oxygen resulting in both abiotic and biotic oxidation (Blowes et al., 2014). For instance, pyrite (FeS_2) oxidation expressed as (Nordstrom, 1982):

$$FeS_2 + \frac{7}{2}O_2 + H_2O \rightarrow Fe^{2+} + 2SO_4^{2-} + 2H^+ \qquad [1]$$

results in the generation of acidic pore-water and the release of SO_4, Fe(II), and toxic elements incorporated in the mineral structure. The oxidation of secondary metal sulfides such as millerite (NiS), chalcopyrite ($CuFeS_2$) and arsenopyrite (FeAsS) can also contribute to the generation of low-quality mine drainage (Blowes et al., 2014; Lindsay et al., 2015). As contaminated pore-water is transported through the unoxidized mine waste, it can undergo a series of acid neutralization and precipitation reactions before leaching into the surrounding geological materials (R. H. Johnson et al., 2000). The net result are contaminant plumes characterized by circumneutral pH and high concentrations of SO_4, Fe(II) and other dissolved metal(loid)s.

Iron(II) can be further oxidized and precipitate Fe(III) (oxy)hydroxides upon surface discharge of the contaminant plume (Nicholson & Scharer, 1994):

$$Fe^{2+} + \frac{1}{4}O_2 + \frac{5}{2}H_2O \rightarrow Fe(OH)_{3(s)} + 2H^+ \qquad [2]$$

This reaction results in AMD— solubilizing toxic elements and negatively impacting the riparian biome (DeNicola & Stapleton, 2002; Warner, 1971).

A well-studied approach to AMD remediation is through the inclusion of a suitable organic carbon source to promote the growth and activity of sulfate reducing bacteria (SRB; Neculita et al., 2007; Tuttle et al., 1969). These microorganisms promote the anaerobic metabolic process of dissimilatory sulfate reduction (DSR) which couples the oxidation of organic carbon, such as lactate, with the reduction of sulfate to sulfide for metabolic growth (Rabus et al., 2013):

$$3\,SO_4^{2-} + 2CH_3CHOHCOO^- \rightarrow 6HCO_3^- + 3HS^- + H^+ \qquad [3]$$

Contaminant immobilization occurs through sorption processes or precipitation reactions with the predominant reaction being the precipitation of low solubility Fe-sulfide phases (Herbert et al., 2000):

$$H_2S + Fe^{2+} \rightarrow FeS + 2H^+ \qquad [4]$$

An established passive approach to promote the growth and activity of SRB to remediate AMD is the use of a permeable reactive barrier (PRB) which involves constructing a zone of permeable organic

carbon that intercepts the pathway of a groundwater contaminant plume. A PRB utilizes the natural hydraulic gradient and removes contaminants as groundwater traverses the reactive media and increases the alkalinity within the PRB and downgradient aquifer (Blowes et al., 2000).

In 1995, the first field-scale organic carbon PRB to treat AMD was installed at Nickel Rim North, Ontario, Canada. This PRB was very effective at passively removing AMD contaminants and increasing the alkalinity as indicated by initial observations during the first 38 months after installation (Benner et al., 1997, 1999, 2002). Case studies of more recent installations of organic carbon PRBs treating groundwater containing high concentrations of dissolved metals have had varying levels of treatment success. Several installations have demonstrated PRBs can effectively remove Cd, Cu, Ni, Fe, U, and Zn up to 42 months after installation (Ludwig et al., 2002, 2009; Naftz et al., 2002). Other systems have shown insufficient removal of metals attributed to low rates of DSR and short residence times within the PRB (Gibert et al., 2011; Jarvis et al., 2006). An organic carbon PRB treatment lifespan is ultimately limited by the availability of sufficient labile organic carbon to sustain DSR. These previous studies provide an indication of short-term performance and modes of failure. Early estimates of the Nickel Rim North PRB, predicated on the results of column experiments, suggested effective treatment would occur for ~15 years (Benner et al., 1999; Waybrant et al., 2002), however the long-term efficacy of a well-operating PRB remediating AMD and treatment system lifespan at the field scale remained unconstrained.

Early mineralogical investigations of the Nickel Rim North PRB revealed the precipitation of mackinawite (FeS) and that S accumulation primarily occurred as acid volatile sulfides (AVS) in the PRB and in the downgradient aquifer (Doerr et al., 2005; Herbert et al., 2000). Geochemical modeling suggested siderite ($FeCO_3$) precipitation as a potential secondary Fe sink (Benner et al., 1999). After six years of treatment, a mineralogical study revealed the presence of pyrite framboids, greigite ($Fe^{2+}Fe^{3+}{}_2S_4$), and some instances of Fe(III) (oxy)hydroxides (Jambor et al., 2005).

As a PRB ages the organic carbon becomes progressively more refractory, which can profoundly affect microbial community structure and activity and the pore-water geochemistry. In turn, these changes could affect mineral precipitation reactions, mineral solubility and contaminant stability. For example, contaminant immobilization appears to be primarily driven by the precipitation of Fe(III) (oxy)hydroxides and sorption reactions in systems with limited rates of SO_4 reduction (Caraballo et al., 2010; Gibert et al., 2011). Conceptual models of treatment systems utilizing DSR often consider the process as uni-directional. However, recent observations indicated that biotic and abiotic S cycling are important processes in a variety of natural systems and can be identified through the

paired use of S and O isotopic ratios from pore-water SO_4 (Antler et al., 2013; Fotherby et al., 2021; Gomes & Johnston, 2017; Mills et al., 2016). Understanding the mineralogy and microbiology after decades of treatment is needed to refine conceptual models of the treatment system and determine if PRB removal is needed at end of treatment life to prevent recontamination of a site.

The current study revisits the Nickel Rim North PRB 26 years after installation to determine if the treatment system remains effective. Microbial community characterization is combined with groundwater geochemical measurements and mineralogical characterization to gain insight into the impact of the microbial community structure on the geochemical dynamics and potential for active S cycling within the PRB and downgradient sediments. The mechanisms of contaminant immobilization and mineral stabilization under current geochemical conditions are evaluated using a combination of sequential extractions, mineralogical characterization and geochemical modeling approaches. This study provides the first long-term comprehensive investigation of PRB treatment technology applied to AMD and metal contaminants.

2.1.1 Nickel Rim North Field Site Description

The abandoned Nickel Rim North tailings impoundment is approximately 35 km northeast of Sudbury, Ontario (**Figure 1.1**). The Cu-Ni mine began operation in 1928 and operated intermittently until 1958. Mill tailings production and disposal occurred from 1953 to 1958. Tailings were deposited in a nearby lake and several narrow glacial valleys forming elevated impoundments, the largest of which was the focus of previous hydrogeochemical investigations (Bain, 1996; Bain et al., 2000; Doerr et al., 2005; R. H. Johnson et al., 2000; McGregor & Blowes, 2002; Ribet et al., 1995) and the current study. A contaminant plume migrates through the tailings impoundment into a shallow glaciofluvial aquifer deposited in a shallow glacially carved bedrock valley. Groundwater travels ~130 m through the aquifer material before discharging into Moose Lake (**Figure 1.1**). Flow modeling suggests that 50% of precipitation recharge water is discharged to the ground surface at the toe of the dam developing acidic surface water flow while 50% contributes to groundwater flow (Bain, 1996; Bain et al., 2000). The PRB was installed ~70 m downgradient from the tailings impoundment where the bedrock valley narrows to ~20 m wide to minimize cost of installation and ensure groundwater flow is directed through the PRB. The PRB was constructed using a cut-and-fill technique across the entire width of the valley and is 3.6 m deep and 4 m wide in the direction parallel to groundwater flow (Benner et al., 1997).

The PRB is composed of a mixture of various materials including: municipal compost (20% by vol.), leaf compost (20% vol.) and wood chips (10% vol.), homogenized with pea gravel (49% vol.), and a minor component of limestone (1% vol.; Benner et al., 1997). The materials for the PRB were chosen on the basis of column experiment results and optimized for cost, local availability, permeability, and potential to provide labile organic carbon for DSR over long time periods (Benner et al., 1997; Waybrant, 1995; Waybrant et al., 2002). Above and below the PRB, along the hydraulic gradient, is a 1 m wide sand buffer zone to improve groundwater flow uniformity (Benner et al., 1997). Acidic surface water infiltrates the aquifer on both the up and down gradient sides of the PRB, but is prevented from entering directly above the PRB by a clay cap which also limits O_2 diffusion and oxidation of the organic carbon (Benner et al., 1999).

2.2 Methodology

2.2.1 Piezometer Installation

Monitoring well nests were installed along the expected groundwater flow path in 2018, 2019 and 2021 (Transect B-B'; **Figure A1**; Supplement A1). Examination of the lithology of cores collected in 2018 and 2019 identified the PRB and informed monitoring well locations installed in 2021. Lithologic evaluation and design dimensions supported the development of the new B-B' cross-section. Monitoring well locations were limited to the southern portion of the PRB due to the presence of a mine road, which was constructed following the PRB installation.

2.2.2 Sample Collection

2.2.2.1 Core Collection

Geologic core samples were collected using the drive point piston sampler method in Fall 2019 and 2021 at seven locations (**Figure A1**; Starr & Ingleton, 1992). Each core was collected in a 5.1 cm inner diameter (ID) aluminum tube, measured to determine the compression factor and sectioned. Core sections were capped with polyethylene (PE) caps then sealed to limit O_2 exposure and water loss. Cores were transferred to the University of Waterloo and stored frozen at -20 °C until sampled.

2.2.2.2 Groundwater Sampling and Handling

Piezometers were conditioned prior to groundwater sampling. Samples were collected in 50 mL Luer Lock polypropylene (PP) syringes using a peristaltic pump and PE tubing that was rinsed in deionized

water. Measurements of pH, Eh, alkalinity and total dissolved H_2S were conducted immediately in the field. Groundwater was filtered (0.45 µm nylon membrane) and split into high-density polyethylene (HDPE) bottles for anion, cation, trace element and SO_4 isotope analysis and amber borosilicate glass bottles for dissolved organic carbon (DOC) determinations. Samples collected for cation and trace element analysis were preserved at pH <2 with trace metal grade HNO_3 and for samples for DOC determinations with A.C.S. reagent grade H_2SO_4. All samples were stored on ice in the field and during transport to the University of Waterloo where they were refrigerated at 4°C until analysis.

2.2.2.3 Solid-Phase Sampling

Core sections were thawed and then sub-sectioned and split lengthwise using a circular saw. These sub-sections were quickly sealed in plastic wrap and re-frozen. The halved core sub-sections were thawed in an anaerobic chamber (Coy Laboratory products) in which the atmospheric O_2 content was confirmed to be anaerobic using indicator strips (BR0055B, Oxoid Ltd.) daily. Samples taken from pre-determined intervals were homogenized and clasts larger than medium pebble removed by hand. Samples for microbiological characterization using 16S ribosomal ribonucleic acid (rRNA) sequencing were taken directly from the core prior to homogenization using a sterilized spoonula and stored in sterilized PP centrifuge tubes at -80 °C. Other splits of sampled material were re-frozen at -20 °C until further analysis.

2.2.3 Groundwater Analysis

During groundwater sampling, fresh sample was repeatedly measured for both pH (Orion 3 Star meter with an Orion triode temperature compensating gel filled pH probe) and Eh (Orion 3 Star meter with Orion 9678 BN redox electrode with Orion 900001 filling solution, corrected to the standard hydrogen electrode) until stability was achieved. Calibration for the pH probe and the redox electrode response was checked throughout the sampling session. Re-calibration of the pH probe occurred if the buffer 7 solution used as an initial calibration verification and as a continuing calibration verification came back >0.02 units from the temperature adjusted value or the Nernst slope was < 95% or > 102%.

Alkalinity and total dissolved aqueous sulfide (S^{2-}) were measured on fresh filtered (0.45 µm nylon membrane) samples. Alkalinity was measured in duplicate or triplicate using a digital titrator and the bromocresol green/methyl red indicator and standardized H_2SO_4 (Hach Method #8203). Concentrations of S^{2-} were determined using a Hach spectrophotometer (DR1900) and the methylene

blue method (Hach Method #8131) with samples prepared in glass syringes to prevent volatilization of H_2S prior to measurement. Due to high Eh and low pH conditions, S^{2-} measurements were not performed on groundwater samples collected from the upgradient aquifer.

Groundwater samples were analyzed for anions (Dionex DX6000 ion chromatograph), major cations (Thermo Scientific iCap 6000, ICP-OES), trace elements (Thermo Scientific X-series 2 ICP-MS), and DOC (Aurora 1030W TOC Analyzer). The accuracy of major ion analysis was estimated through calculations of the charge balance percent error using PHREEQC (v. 3.6.2.15100; Parkhurst & Appelo, 2013) with a maximum variance from the electro-neutral condition of 10.8% (**Figure A2**).

A subset of groundwater samples was analyzed for both $\delta^{34}S_{SO_4}$ and $\delta^{18}O_{SO_4}$ from groundwater SO_4. The $BaSO_4$ was precipitated at the University of Waterloo (Supplement A2) and analyzed at the University of Calgary Isotope Science Laboratory - Applied Geochemistry Group for both S and O isotopic ratios. Ratios of $^{34}S/^{32}S$ were measured using a combustion/ reduction reactor (Carlo Erba NA 1500® elemental analyzer) interfaced (via a Conflo-III® device) to a continuous flow mass spectrometer (CF-EA-IRMS; Thermo Delta+XL®). Ratios of $^{18}O/^{16}O$ were measured using a high temperature reactor (Heka High temperature oxygen analyzer) and interfaced (via a Conflo-III® open split/interface) to a CF-EA-IRMS (Thermo Delta+XL®). Isotopic compositions for O and S are reported in standard delta notation as per mil (‰) deviations from Vienna Standard Mean Ocean Water (VSMOW) and Vienna Cañon Diablo Troilite (VCDT) respectively. Precision and accuracy as σ of 10 laboratory standards is 0.5‰ for $\delta^{18}O_{SO_4}$and 0.3‰ for $\delta^{34}S_{SO_4}$.

2.2.4 Bulk Material Characteristics

The moisture content for each sample was determined by the difference in mass of samples before and after freeze drying during sample preparation. After drying, the inorganic grains >2.36 mm were removed by sieve (No.8) with the mass of the retained fraction recorded to correct for the unreactive component in the moisture content calculations. Approximately 20% of the samples were run in duplicate with a mean relative percent difference of 3.7% and a maximum of 17.7%.

The dry bulk density of reactive organic carbon within the PRB was determined by measuring the volume of water displaced by the core piece in a water bath and subtracting the volume of gravel and aluminum core shell. The dried mass of the organic carbon component was determined after drying at 105 °C for 48 hours and was used to calculate the corrected dry bulk density without gravel for accumulation rate calculations.

2.2.5 DNA Extraction and Analysis

Bacterial and archaeal diversity was analyzed for 34 samples from cored material using high throughput amplicon sequencing of 16S rRNA genes. Over ten percent of samples were run in duplicate (5 samples) to assess variation in results due to sampling and analysis. This number of duplicates was deemed sufficient based on the similarity in duplicate results. Total genomic material was extracted from samples using Sox DNA isolation kit (v. 14.7; Metagenome Bio Inc.) following manufacturer methods for samples with high humic acid content. Extracted DNA was stored at -80 °C before 16s rRNA gene amplicon sequencing (Metagenome Bio Inc.; Toronto, ON). The V4 region of 16s rRNA genes was amplified followed by illumina MiSeq Sequencing using the modified universal primers 515F/806R (Walters et al., 2016). Sequencing data was processed using the Mothur program (v.1.48.0, updated: 18/03/2022; Schloss et al., 2009) and Mothur MiSeq standard operating procedure (from 17/06/2022; Kozich et al., 2013). Chimeric sequences were discarded based on predictions by vsearch referencing the Silva database for 16S rRNA gene sequences (release 132 for Mothur, downloaded 18/03/2019).

Initially, unmerged duplicate samples were used in data processing to allow for the comparison of populations on the phylum and genus level, then merged for further inquiry due to their high level of similarity (**Figure A3**). Taxonomic investigations utilized clustering of the operational taxonomic units (OTUs) at a 97% similarity level using a *de novo* OTU picking process. The Silva database was used as reference for taxonomic annotation with several taxa (unknown, mitochondria, eukaryotes) discarded for further analysis. Cyanobacteria were kept for further processing. A control sample was used and the minor contaminants detected (~45 sequences) were removed from all samples.

Relative abundances of SRB, iron-oxidizing (IOM) and sulfur-oxidizing microorganisms (SOM) were obtained by screening the taxonomy file for prokaryotic genera (or in a few instances higher taxa when identification to the genus level was not possible) containing at least one species with the investigated metabolic trait. Prokaryotic diversity was investigated in the data set with unmerged duplicate samples. Good's coverage was used to assess how representative the samples were of the environments from which they were taken. The Gini-Simpson's diversity index (1-D) and Chao richness estimator were chosen to measure the microbial α-diversity for each library. An overview of 16S rRNA gene sequence data statistics is provided in Supplementary Information A3 and **Table A1**.

2.2.6 Total Carbon and Sulfur Analysis and Selective Sulfur Extraction

The distribution of total C and S content in sampled core material was analyzed using Eltra CS 2000 C/S determinator equipped with an induction and resistance furnace. Samples from the PRB cores underwent further comminution using a ball mill to reduce the larger organic material pieces to fine flour (< 40 nm). To determine the inorganic C content, a split of prepared sample was heated in a muffle furnace to 500 °C for 1 hour to burn off all the organic C with the difference in mass recorded. The muffle furnaced material was also analyzed for C content from which the % inorganic C content was calculated.

Selective extractions were employed to evaluate the solid phase S species within the reactive material. The AVS and chromium reducible sulfur (CRS) extractions have been applied to PRB and wetland treatment systems to characterize S species with good success (He et al., 2008; Herbert et al., 1998; Machemer et al., 1993). A hot 6N HCl with $SnCl_2$ extraction was conducted to quantify the AVS fraction (Rice et al., 1993) and the CRS (Canfield et al., 1986) method was used to quantify the total reducible sulfur (TRS) fraction. Details on the extraction methods, standards used, and their recoveries are provided in in the Supplementary Information A4.

2.2.7 Mineralogy

2.2.7.1 Optical Mineralogy, SEM and EDX Analysis

Freeze-dried core material collected in 2019 was prepared as double-sided-polished thin sections by mounting sample material with Krazy Glue® onto a Suprasil 2A quartz plate (Spectrum Petrographics; Vancouver, Washington) for synchrotron-based μX-ray fluorescence (μXRF). The mineralogy was characterized by examining the thin sections using both reflected and transmitted light on a polarized light microscope (Nikon Eclipse LV100N POL). Areas of interest were further analyzed using a scanning electron microscope (SEM; FEI Quanta FEG 250) with energy dispersive X-ray spectroscopy (EDX; Oxford X-ACT) to develop elemental area maps and determine the percentage of elements at specific locations of interest.

2.2.7.2 Synchrotron Analyses

Bulk S K-edge X-ray absorption near-edge structure (XANES) spectra were collected on the soft x-ray micro-characterization beamline (SXRMB) at the Canadian Light Source (CLS) in August, 2022. Freeze-dried samples were powdered in the glovebox and transported to the beamline in an anaerobic cannister. Samples and standards were prepared for analysis by spreading thin layers of powdered

material on double-sided tape and mounted on a copper plate. Samples were analyzed under vacuum. Spectra were collected between 2,442 eV and 2,552 eV with a 2.0 eV step size from 2,442 to 2,466 eV, a 0.1 eV step size from 2,466 eV to 2,492 eV and a 0.8 eV step size from 2,492 eV to 2,552 eV.

Analytical μXRF maps were collected on the SXRMB at the CLS in September 2021 to depict the spatial distribution of S, Ni, and Fe in areas of interests, and determine locations of Ni and S μ-XANES spectra for mineral phase identification. Sulfur phase maps were collected at 2,469.6 eV, 2,472.4 eV, and 2,481.4 eV in some locations. Thin sections were mounted to a sample holder under vacuum. The μXRF maps were collected using a 10 μm x 10 μm beam size, an excitation energy of 8,354 eV (above Ni K-edge) and a 7-element silicon drift detector (RAYSPEC SGX Sensortech LTD.). S K-edge μ-XANES were collected over the same energy region and steps as the bulk S K-edge XANES at SXRMB. Ni K-edge μ-XANES spectra were collected between 8,303 eV and 8,463 eV with a 2.0 eV step size from 8,303 to 8,327eV, a 0.4 eV step size from 8,327 eV to 8,363 eV and a 0.8 eV step size from 8,363 eV to 8,463 eV.

Bulk Fe K-edge XANES were collected on the SXRMB at the CLS in August 2022. Spectra were collected between 7,082 eV and 7,262 eV with a 1.0 eV step size from 7,082 to 7,106 eV, a 0.35 eV step size from 7,106 eV to 7,137 eV and a 0.75 eV step size from 7,137 eV to 7,262 eV.

Multiple scans of all XANES and μ-XANES were collected and merged prior to data processing to improve the signal-to-noise ratio and enhance data analysis. Data processing including: energy calibration, multiple scan averaging, and normalization, was conducted using Larch (Newville, 2013). Reference spectra used in linear combination fitting (LCF) of S, Ni and Fe K-edge spectra were collected during the same experimental runs or from previously collected standards with E^0 correction of samples and standard spectra with common reference materials like gypsum. All samples used the same set of standards for LCF and the best-fit LCF results are reported based on constituents in the fit and minimized χ^2. S XANES standards used for LCF fitting were collected previously (ESRF, 2023; He et al., 2010; Liu et al., 2016). Ni XANES standards used for LCF fitting include: millerite, $Ni(OH)_2$, $NiSO_4$, Ni foil, NiO, NiS_2, and Ni sorbed to ferrihydrite ($Fe_2O_3 \cdot 0.5H_2O$). Fe XANES standards used for LCF fitting include: mackinawite (Wilkin & Beak, 2017), pyrite (He et al., 2010), pentlandite $(Fe,Ni)_9S_8$, siderite ($FeCO_3$; Lee & Wilkin, 2010), magnetite (Fe_3O_4), FeO, Fe_2O_3, ferrihydrite, and goethite (α-FeO(OH)).

2.2.8 Data Analysis

Saturation indices were determined using the geochemical modeling software PHREEQC (v. 3.6.2.15100; Parkhurst & Appelo, 2013) using the WATEQ4F thermodynamic database (Ball & Nordstrom, 1991) with a heatmap produced using Python Pandas and Seaborn (Waskom, 2021). Volatile organic acids were not included in the geochemical modeling due to the low concentrations (< 5 mg L^{-1}). Exclusion of volatile organic acids allowed for the use of the WATEQ4F database which is preferred over MINTEQ V4 due to a higher level of internal consistency and validity of results. Redox couples were determined using pe (converted from Eh) values for each sample.

2.3 Results and Discussion

2.3.1 Treatment Performance of the Nickel Rim North PRB

Analyses of the chemical composition of pore-water samples indicate the contaminant plume in the upgradient aquifer continues to have the potential to produce acidity and has elevated concentrations of metals, requiring continued remediation (**Figure 2.1**). Groundwater SO_4 in the upgradient aquifer is consistently elevated with a mean of 1,787 ± 88 mg L^{-1} (mean ± standard deviation). The groundwater SO_4 is likely regulated by gypsum precipitation as it is near saturation in all upgradient wells (**Figure A2**). The mean groundwater Fe concentration is 516 ± 67 mg L^{-1} with a maximum of 635 mg L^{-1} observed immediately upgradient of the PRB (monitoring well nest: NR2018-5). Upgradient aquifer groundwater Fe concentrations remained consistent with observations 26 years ago (Benner et al., 1999). Groundwater Ni is variable, but generally elevated, with a mean of 103 ± 79 μg L^{-1}. An observed concentration of 1,723 μg L^{-1} in surface water may indicate groundwater Ni concentrations will continue to increase over time. The calculated potential acidity is > 15 meq L^{-1} in every upgradient well, suggesting a strong likelihood of AMD production if the contaminant plume discharges to the surface without treatment.

After 26 years of treatment there is still a marked improvement in water quality through the Nickel Rim North PRB. Groundwater SO_4 decreases by 70% through the PRB to a mean of 544 ± 79 mg L^{-1} in the immediate downgradient aquifer (monitoring well nest: PRB2019-2). Higher removal rates occur in the upper half of the upgradient PRB, whereas little removal is observed in the lower half of the NR2018-7 well nest. As a result, lower concentrations occur along the flow path with a minimum observed concentration of 302 mg L^{-1} in PRB2019-1 at 1.04 m. In a similar pattern to SO_4, groundwater Fe decreases by 77% to a mean of 114 ± 12 mg L^{-1} immediately downgradient of the PRB (monitoring well nest: PRB2019-2). A minimum of 18 mg L^{-1} Fe was observed in conjunction with the SO_4 minimum within the PRB. These low concentrations in Fe and SO_4 do not extend downgradient, which may indicate an area of lower groundwater flow rates that allow for a greater residence time and higher levels of removal. The presence of Fe in all sampling locations and a maximum measured S^{-2} concentration of 13 μg L^{-1} in the downgradient aquifer with little (≤ 5 μg L^{-1}) to no measurable S^{-2} in the PRB suggests the rate of DSR is insufficient to completely remove Fe and produce excess S^{-2}. The potential acidity of the groundwater decreases through the PRB resulting in net acid-consuming conditions in monitoring wells further downgradient of the PRB.

Comparing the influent to effluent Ni concentrations suggests removal within the PRB as concentrations are below the United States Environmental Protection Agency (US EPA) maximum contaminant level of 25 μg L^{-1} immediately downgradient of the PRB. However, there are Ni concentration maximums dispersed throughout the PRB with a maximum of 2,062 μg L^{-1} observed. This may suggest Ni is being released in some zones of the PRB and re-immobilized in others.

Improved groundwater conditions are observed in the downgradient aquifer except in the area where there is surface water influence (monitoring well nest: PRB2019-3) which results in low pH, high Fe, high Ni, and increased potential to produce acidity. This surface water influence is based on field observations of areas with acidic surface water present, which was variable along the B-B' transect. The overall decrease in SO_4, metal concentrations and a reduction in the potential acidity would suggest the PRB is still primarily operating as designed with DSR driving the precipitation of Fe sulfides in accordance with reactions 3 and 4.

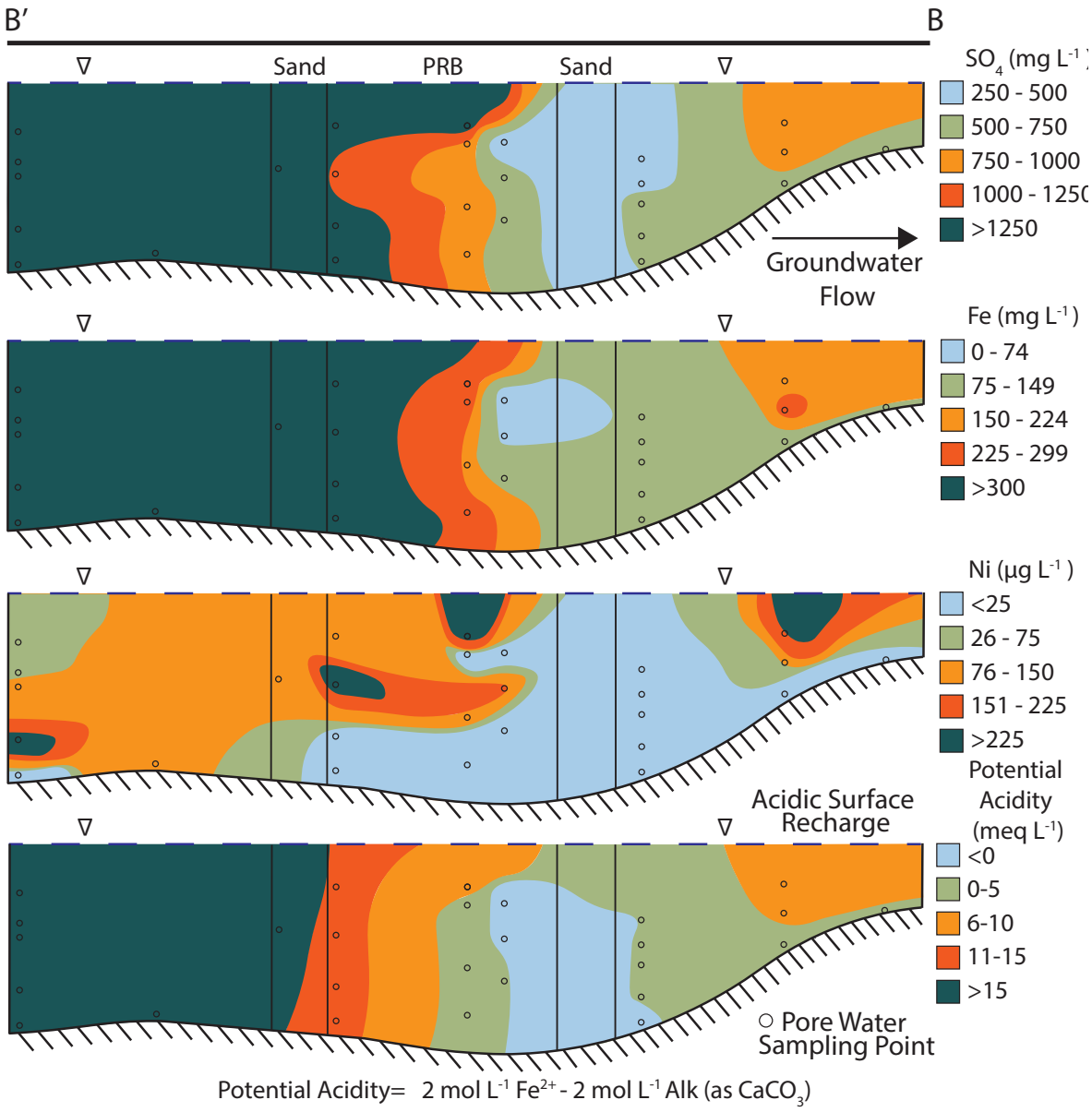


Figure 2.1. Groundwater aqueous chemistry contours plots from Fall 2021 showing concentrations of SO_4, Fe, and Ni along the B'-B transect. Potential acidity was calculated for each water sampling point. Water sampling points measured and used for contouring are illustrated as open circles.

The observed aqueous geochemical conditions are consistent with a SO_4 reducing microbial environment. In the aquifer, pH increases with depth are likely driven by acid neutralization reactions (**Figure 2.2**). The groundwater is undersaturated with respect to the carbonate minerals and aluminum hydroxide phases initially present in the aquifer material (**Figure A2**) which is in agreement with limited inorganic carbon measured in the upgradient aquifer material (**Figure A4**). The dissolution of these minerals neutralizes acidity as the groundwater migrates through the aquifer. The upgradient aquifer has circumneutral pH with a mean of 5.9 ± 0.3. Measured pH increases along the groundwater flow gradient through the PRB to a mean of 6.55 ± 0.14. This increase in pH is attributed to bicarbonate buffering that is generated during DSR and often observed in treatment mediated by DSR (Lefticariu et al., 2015; Lindsay et al., 2009; Waybrant et al., 2002). Measured alkalinity in the upgradient aquifer was low (mean of 53 ± 34 mg L^{-1} as $CaCO_3$). The highest concentrations observed were in the PRB and downgradient aquifer with a maximum concentration of 875 mg L^{-1} as $CaCO_3$. This increase in alkalinity is consistent with an increase in bicarbonate concentration as a product of DSR in the PRB. The increasing DOC and decreasing Eh suggest the reactive media is continuing to supply labile organic carbon and supporting conditions suitable for DSR. The highest DOC concentrations were observed in the lower portion of the PRB (maximum 173.19 mg L^{-1} as C). Concentrations of volatile organic acids were measured at each sampling point with no appreciable concentration of lactate, formate, propionate, or acetate detected which may be indicative of rapid turnover, if produced. The decline in DOC concentration occurs in the same portion of the PRB where decreases in SO_4 and Fe concentrations were observed, suggesting DOC is being utilized through anaerobic processes and continues to promote DSR. Groundwater Eh decreases with depth in the aquifer material and through the PRB. Mean value in the upgradient aquifer is 233 ± 65 mV and reaches a low of 39 mV in the PRB and downgradient aquifer. Wells with surface water influence in the downgradient aquifer (monitoring well nest: PRB2019-3) have low pH, low alkalinity, low DOC, and high Eh.

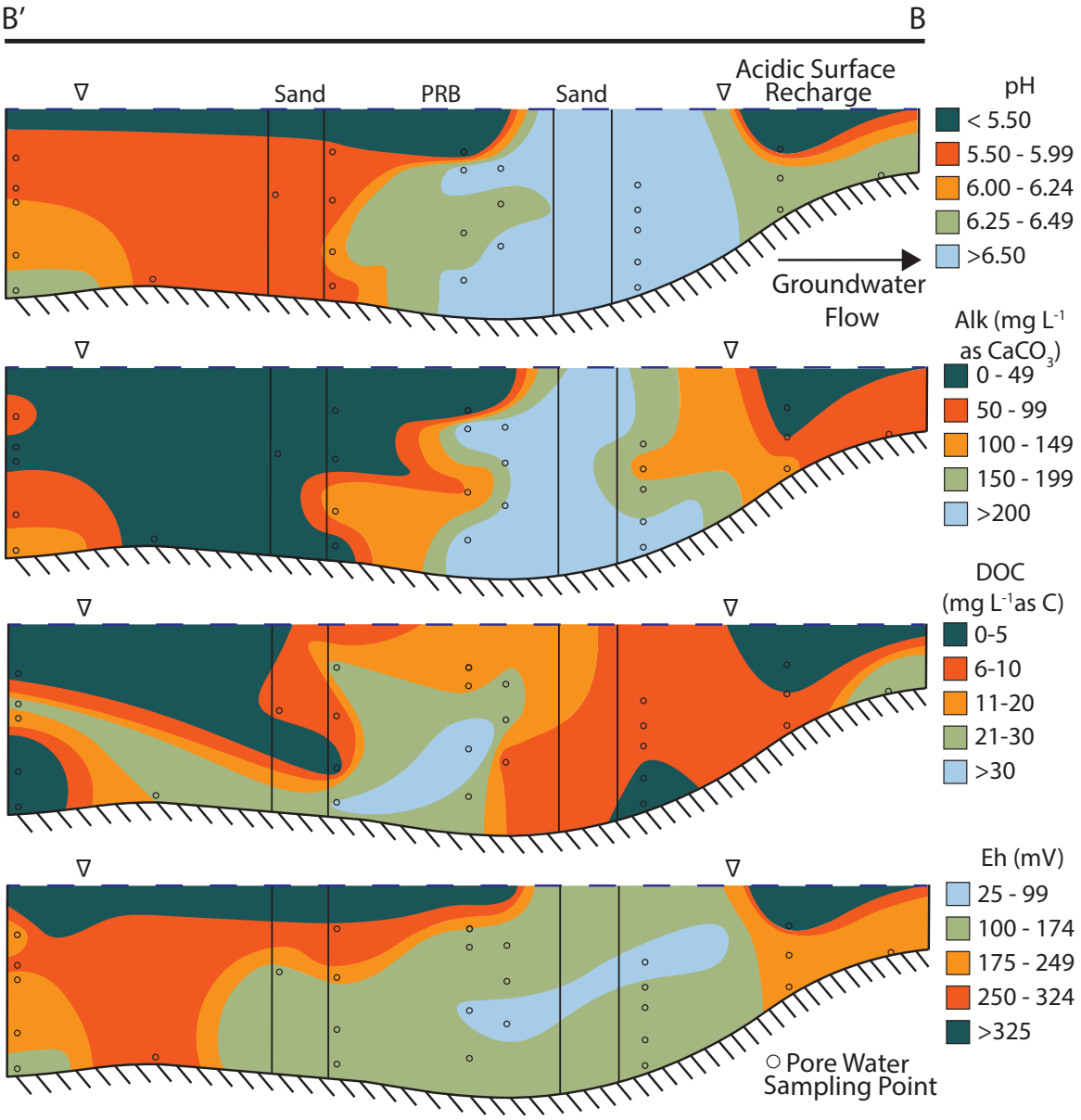


Figure 2.2. Groundwater chemistry contours from Fall 2021 of measured pH, alkalinity, DOC, and Eh in the Nickel Rim North PRB and surrounding aquifer along the B'-B transect. Water sampling points used for contours are illustrated as open circles.

Along the B'-B transect through the PRB, the mean bulk removal rate of SO_4 was 4,970 mg L^{-1} a^{-1} (51 mmol L^{-1} a^{-1}) and Fe was 1,610 mg L^{-1} a^{-1} (28.8 mmol L^{-1} a^{-1}) assuming a similar 90 day residence time as previous estimates (**Table A3**). A rapid decline in the rate of SO_4-removal was observed during the first three months after the installation of the PRB, followed by a more gradual decline over the first three years (Benner et al., 2002). During the first three years, the rate of SO_4-removal decreased by 30% to 5,090 mg L^1 a^{-1} (53 mmol L^{-1} a^{-1}) and the rate of Fe-removal decreased by 50% to 1,790 mg L^{-1} a^{-1} (32 mmol L^{-1} a^{-1}). The decline in SO_4-removal rate was attributed to a loss of organic carbon reactivity (Benner et al., 2002). Current removal rates of Fe and SO_4 are similar to those measured after 38 months of treatment suggesting very little, if any, decline in treatment performance after more than 20 years. A gap in data collection between 38 months of treatment and this study prevents further temporal evaluation in treatment performance. The most recent results suggest the reactivity of the OC and longevity of the PRB exceed initial estimates of long-term treatment capacity and the framework supporting these estimates and treatment system lifespan should be revisited.

The current SO_4- and Fe-removal rates are based on groundwater velocity values presented by Benner et al. (2002). The current SO_4 and Fe concentration measurements were near the margin of the PRB, and a more refined understanding of the hydrogeologic flow regime through this section of the PRB is required to provide rigorous estimates of removal rates within the PRB. Benner et al. (2002) observed preferential flow pathways along other transects through the PRB which were attributed to slight differences in the ratio of organic carbon to gravel. Discharge through these preferential flow zones leads to ineffective treatment. Improved installation techniques to achieve a more consistent ratio of gravel to organic carbon throughout the PRB were used to mitigate this concern in subsequent installations (*e.g.,* Ludwig et al., 2009). Regardless, the groundwater geochemistry results presented here demonstrate the reactive media has sustained bioremediation of Fe, Ni and AMD on a multi-decadal timescale.

2.3.2 Microbial Community Response to an Aging PRB

Characterization of the microbial communities present in the Nickel Rim North PRB provides insight into the microbial dynamics contributing to the long-term treatment performance. 16S rRNA amplicon sequencing of sampled solid phase material revealed the most abundant phylum were Firmicutes (35.8%) followed by Proteobacteria (14.8%), Chloroflexi (8.4%), Actinobacteria (5.0%), Acidobacteria (3.6%) and Bacteroidetes (2.5%; **Figure A5**). The distribution of bacteria is similar in

many respects to what has been found in other long-term evaluations of lignocellulose-based organic carbon sulfate-reducing bioreactors (SRBRs) treating mine-influenced water (Baldwin et al., 2015; Drennan et al., 2016; Nielsen et al., 2018). The most dominant prokaryotic groups could not be identified on the genus level but were dominated by unclassified *Bacillales* and *Bacteria* (**Table A4**). These two unclassified groups were a large amalgam of unclassified sequences and improved taxonomic annotation would further elucidate important relationships in the microbial communities present within the aquifer and PRB. Variation in the overall community structure was observed between the upgradient aquifer, the PRB, and the downgradient aquifer (**Figure A5 & A6**).

Utilization of complex mixtures of lignocellulose-based organic carbon for AMD treatment can require diverse microbial community compositions due to the reliance of SRB on cellulose degraders and fermenters to provide a long-term supply of labile organic carbon (Drennan et al., 2016; Hiibel et al., 2011). Firmicutes and Bacteroidetes have been proposed as indicator clades in anaerobic digestors and SRBRs due to their importance in organic carbon mineralization (Chen et al., 2016; Drennan et al., 2017; Mirjafari & Baldwin, 2016). While the Firmicutes phyla is diverse in metabolic function, a taxa capable of anaerobic lignocellulose degradation in the Nickel Rim PRB is Ruminococcaceae which has been observed in SRBRs (Baldwin et al., 2015; Drennan et al., 2016; Mirjafari & Baldwin, 2016). Drennan et al. (2017) identified a higher ratio of Firmicutes to Bacteroidetes coincided with metal sulfide precipitation within a SRBR. Mirjafari and Baldwin (2016) suggested that a decline in fermentative species in Firmicutes and Bacteroidetes may be indicative of declining treatment performance. Similarly, Aoyagi et al. (2018) found a decline in abundance of Firmicutes and Bacteroidetes under unstable conditions for SO_4 reduction due to shorter residence times in SRBRs. In the Nickel Rim North PRB there is a greater relative abundance of Firmicutes to Bacteroidetes, but they make up a much lower proportion of the total microbial abundance than what is commonly observed in functioning SRBRs (Drennan et al., 2017).

The mixture of organic carbon in the Nickel Rim North PRB was selected to provide varying degrees of reactivity. More labile organic carbon (*e.g.*, leaf mulch) was included in the reactive mixture to promote the rapid initiation of DSR. These components of the reactive media were consumed rapidly resulting in a high initial SO_4-removal rate followed by a decline in the rate of SO_4 reduction (Benner et al., 2002). In a set of column experiments, Logan et al. (2005) suggested labile organic carbon availability for SRB, due to low rates of cellulose hydrolysis, greatly impacted treatment performance. Long-term SRB growth and activity, in many environments, is rate-limited by synergetic interactions with microbes capable of hydrolytic degradation of macromolecules to

mineralize more complex organic carbon, such as cellulose, into low molecular weight organic compounds suitable for SRB (Arndt et al., 2013). Clostridium, Clostridiales, Ruminiclostridium and Ruminococcaceae are observed to be present in the PRB and capable of degrading cellulose. Hydrolyzing complex structures can require a variety of enzymes and if one is limited or missing it can produce a so-called 'speed bump' or 'barricade' that impedes organic carbon availability to the greater microbial community (Arnosti, 2011). In effect, the enzymatic degradation of more complex organic carbon becomes the rate-limiting step in treatment performance. Some of these limitations may be overcome, at the field scale, through more suitable geochemical conditions for cellulose hydrolysis, a larger more diverse microbial community, and/or transport processes that result in higher sustained rates of DSR.

Sulfate reducing bacteria were detected in the upgradient aquifer, PRB, and downgradient aquifer with no statistical difference in the abundances between sample types (t-test: $p > 0.05$; **Figure 2.3**). Within the PRB and aquifer material, the putative sulfate reducing genera detected were diverse (**Table A4**). The presence of SRB throughout the study area suggests conditions suitable for SO_4 reduction were ubiquitous. While the modest abundance of SRB within the PRB may indicate declining treatment performance, previous studies of SRBRs have found no correlation between relative abundance of SRB taxa and the rate of SO_4 reduction or other performance parameters (Drennan et al., 2016; Mirjafari & Baldwin, 2016). Rather, the overall microbial diversity has been found to be higher in lignocellulose-based treatment systems resulting in a lower relative abundance of SRB (Hiibel et al., 2011). There were distinct differences in the SRB communities with *Desulfobacteraceae* as the abundant group in the PRB sub-samples while *Desulfobacca* was the most abundant in the aquifer material analyzed. *Desulfobacteraceae* have been found to make up a notable proportion of the active microbial community in lignocellulose-based SRBRs (Burns et al., 2012; Rezadehbashi & Baldwin, 2018). Members of *Desulfobacteraceae* can completely oxidize acetate along with various other forms of organic carbon (Rabus et al., 2015). The abundance of *Desulfobacca*, a bacteria genera that oxidizes acetate (Göker et al., 2011), in downgradient aquifer samples where no acetate was measured, suggests migration of acetate from the PRB into the downgradient aquifer and rapid acetate utilization. *Desulfosporosinus* are commonly found in SRBRs (Habe et al., 2020), but are found in greater abundance in the downgradient aquifer compared to the PRB at Nickel Rim North. These bacteria are found in AMD environments under low pH conditions (Church et al., 2007; Sánchez-Andrea et al., 2011, 2014). While *Desulfosporosinus* have been shown to support bioremediation via DSR (Habe et al., 2020; Sánchez-Andrea et al., 2014), a greater

abundance of these bacteria in treatment systems may indicate challenging environmental conditions which limit cellulose degraders and fermenters– impacting long-term treatment performance when more complex organic carbon is used.

Many abiotic and biotic redox processes can impart a S isotope fractionation (Canfield & Thamdrup, 1994; Pellerin et al., 2019; Rees, 1973; Sim et al., 2011). Abiotic sulfate reduction is predicted to be kinetically limited under the environmental conditions of the PRB (Rickard & Luther, 2007). The pre-eminent process that fractionates S isotopes in a PRB is DSR (Gibson et al., 2011; Guo & Blowes, 2009). Fractionation of S during DSR occurs over a multi–step reversible pathway that results in the preferential incorporation of ^{32}S into sulfides and more positive $\delta^{34}S_{SO_4}$ measurements in the remaining dissolved SO_4 (Brunner et al., 2005; Wing & Halevy, 2014). Groundwater $\delta^{34}S_{SO_4}$ increased from 4.9 ± 0.5 ‰ in the upgradient aquifer to a mean of 21.4 ± 13.1 ‰ in the PRB and downgradient aquifer (**Figure 2.4**). The increase in $\delta^{34}S_{SO_4}$ coincides with a decrease in groundwater SO_4 concentration. The maximum $\delta^{34}S_{SO_4}$ measured was 50.1‰ which coincided with the lowest measured groundwater SO_4. When $\delta^{34}S_{SO_4}$ measurements are viewed in conjunction with the aqueous geochemical results and microbial community analysis provide strong evidence of DSR actively occurring in the PRB.

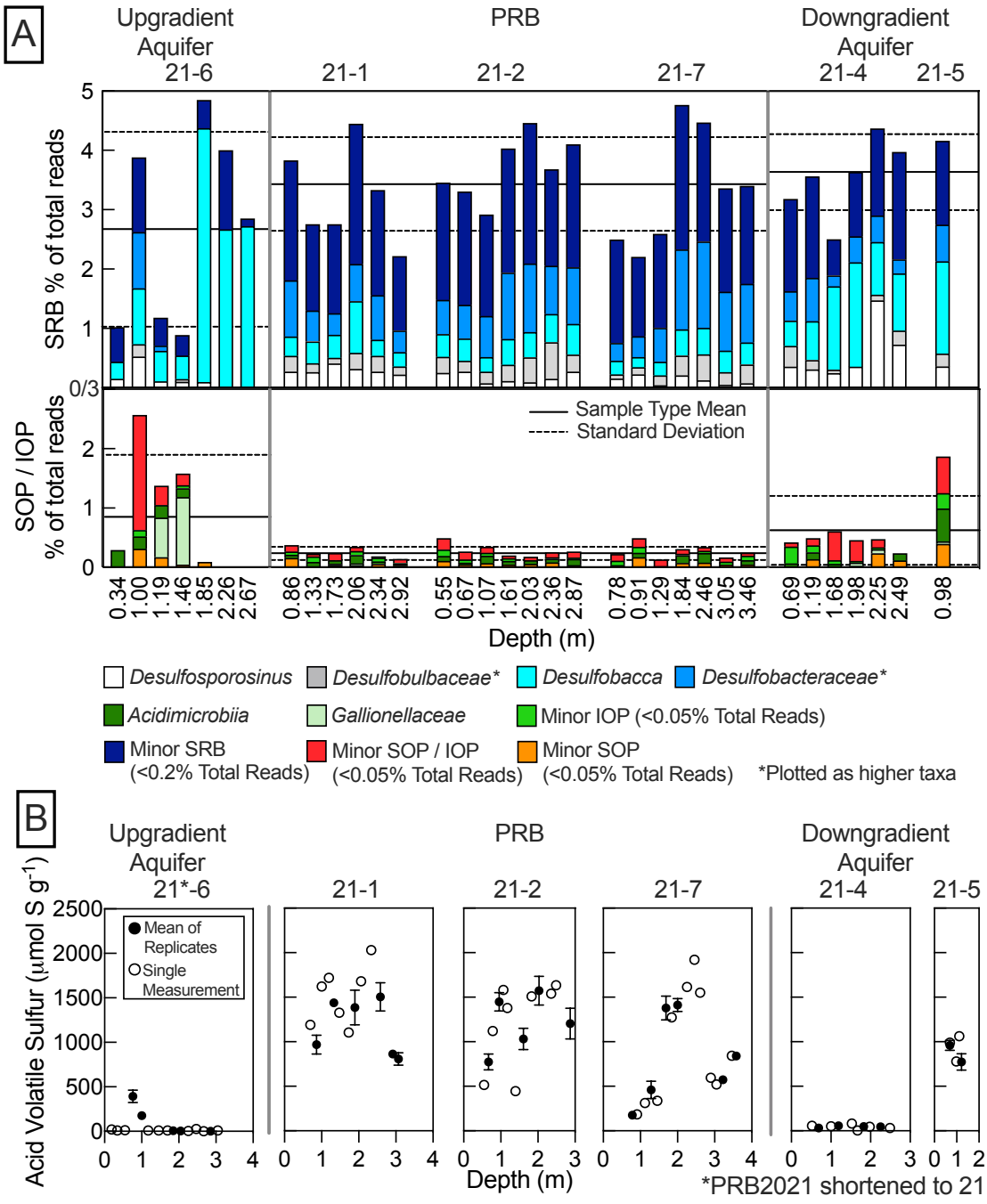


Figure 2.3. A) Proportion of total reads for sulfate and/or sulfur reducing bacteria (SRB) and sulfur (SOP) and/or iron oxidizing prokaryotes (IOP) for cored material. B) Acid volatile sulfides concentration in dry sampled material from cores sampled in 2021.

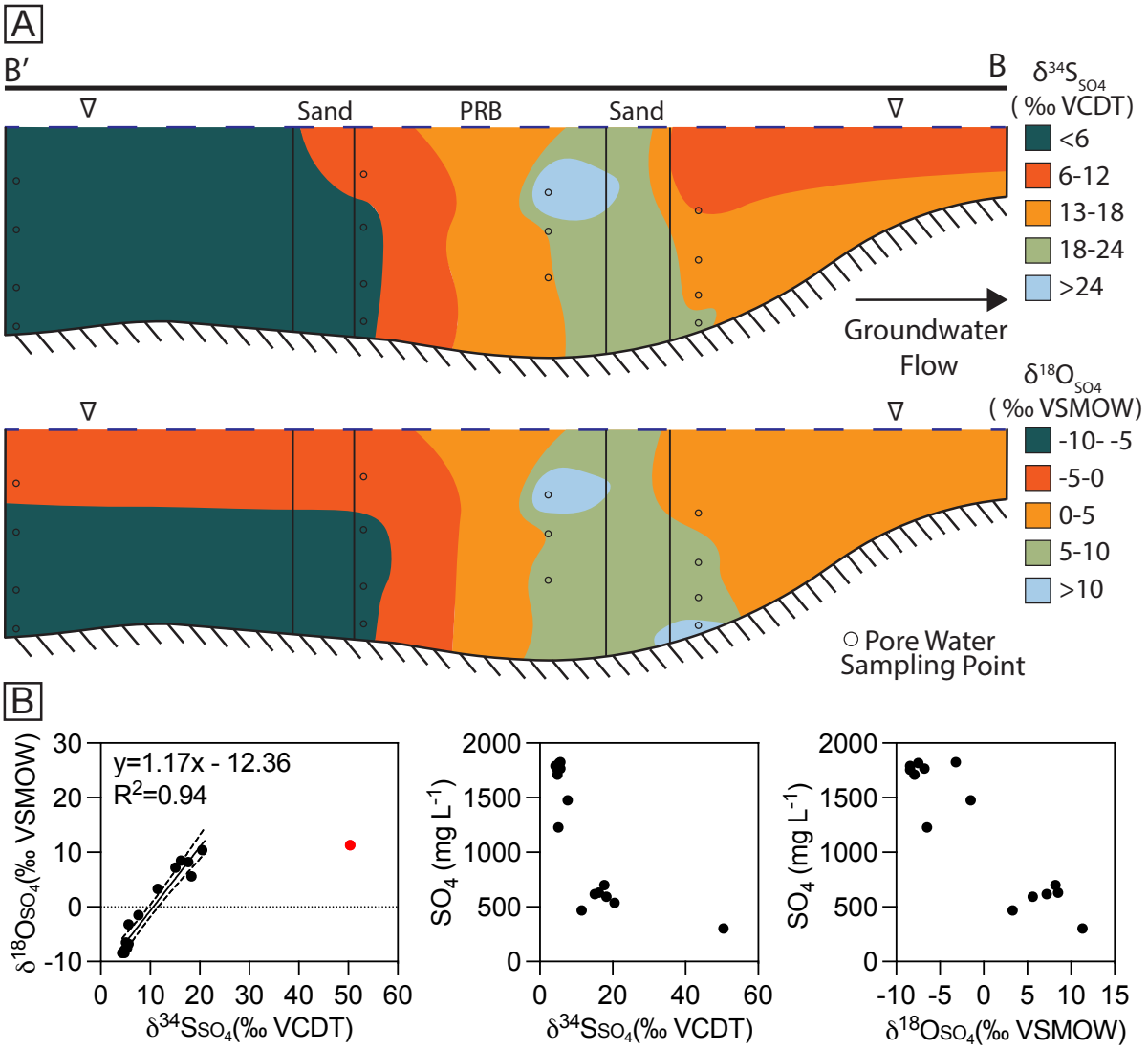


Figure 2.4. A) Groundwater isotopic composition contour plots for both $\delta^{34}S_{SO_4}$ and $\delta^{34}S_{SO_4}$ from Fall 2021 sampling along the B-B' transect. B) Cross-plots of $\delta^{34}S_{SO_4}$ *vs.* $\delta^{34}S_{SO_4}$, $\delta^{34}S_{SO_4}$ *vs.* SO_4 and $\delta^{34}S_{SO_4}$ *vs.* SO_4. A simple linear regression for $\delta^{18}O_{SO_4}$ *vs.* $\delta^{34}S_{SO_4}$ was conducted with the line of best fit illustrated as a solid line and 95% confidence bands as dashed lines. The point in red is considered to be in 'apparent equilibrium phase' and not included in the linear regression. Standard delta notation reported as per mil (‰) deviations from Vienna Standard Mean Ocean Water (VSMOW) and Vienna Cañon Diablo Troilite (VCDT).

The dynamics of the S cycle within a PRB are likely to increase in complexity over time due to lower availability of reactive organic material. The paired use of $\delta^{34}S_{SO_4}$ and $\delta^{18}O_{SO_4}$ have been applied to natural environments to compare the sulfate reduction rate between sites (Antler et al., 2013) and identify S cycling (Gomes & Johnston, 2017; Mills et al., 2016). Like ^{32}S, ^{16}O is preferentially distilled during the enzymatic steps in DSR (Brunner et al., 2005). Two critical processes are the equilibrium isotope exchange between sulfoxy intermediates (*i.e.,* sulfite) and water which concentrates ^{18}O in the S intermediate species which can then undergo reoxidation returning the isotopically altered SO_4 back to the extracellular environment. New O atoms would likely be incorporated from and/or undergo a similar equilibrium effect with water during re-oxidation of sulfides (Brunner et al., 2005; Mills et al., 2016). Importantly, the O isotope exchange between SO_4 and water is slow under normal groundwater conditions, allowing it to track these altered isotopic signatures (Lloyd, 1968). In some environments, $\delta^{18}O_{SO_4}$ increases initially until it reaches a so-called "oxygen isotope equilibrium" value (Antler et al., 2013). The relative initial change of $\delta^{18}O_{SO_4}$ *vs.* $\delta^{34}S_{SO_4}$ can be indicative of how often these back reactions and/or reoxidation are occurring. A more shallow slope of the apparent linear phase (SALP) is expected to result from high SO_4 reduction rates with limited back reaction and/or reoxidation (Antler et al., 2013; Mills et al., 2016)– the ideal condition of a PRB.

The groundwater $\delta^{18}O_{SO_4}$ values show a similar trend to $\delta^{34}S_{SO_4}$ increasing through the PRB with a maximum increase of 19.7 ‰. There is a strong positive linear relationship when $\delta^{18}O_{SO_4}$ is plotted *vs.* $\delta^{34}S_{SO_4}$ (**Figure 2.4**). The SALP is 1.17, calculated using a simple linear regression where one point was left out as it was attributed to being in 'apparent equilibrium phase' (Antler et al., 2013) based on the relatively large change in $\delta^{34}S_{SO_4}$ compared to $\delta^{18}O_{SO_4}$. Other possibilities that may result in a large increase in $\delta^{34}S_{SO_4}$ compared to $\delta^{18}O_{SO_4}$, in which the 'apparent equilibrium phase' is not reached include: high localized SO_4 reduction rates occurring in the area in which this monitoring well is located or a longer residence time. Both a higher rate of SO_4 and a longer residence time would allow for increased DSR and change in $\delta^{34}S_{SO_4}$ without a notable shift in $\delta^{18}O_{SO_4}$. Treating this point as an outlier is appropriate given the consistency of the other data within the PRB. In ocean sediments, SALP were measured between 0.35-1.7 with higher values measured in deep sea sediments with slow SO_4-reduction rates (Antler et al., 2013). The Nickel Rim North PRB results

suggest slow to moderate SO_4-reduction rates and/or a high propensity for S cycling. The variation of $\delta^{18}O_{SO_4}$ for locations with similar SO_4 concentration may provide some evidence of limited S cycling.

The difference in the abundance of sulfur oxidizing (SOP) and iron oxidizing prokaryotes (IOP) among different sample types (upstream aquifer, PRB, downstream aquifer) was not statistically significant (t-test: $p > 0.05$). However, there was a discernable increase in population of (predominantly acidophilic) SOP/IOP in areas with surface water influence (PRB2021-6, PRB2021-5; **Figure 2.3**). Sulfur oxidizing prokaryotes and iron oxidizing prokaryotes were also observed in the PRB together with SRB during the initial microbial study of the Nickel Rim North PRB (Benner et al., 2000). These divergent metabolic processes found together were reconciled through the proposition of disparate redox micro-environments with advective and diffusive transport processes allowing for a mutualistic microbial relationship (Benner et al., 2000). The more recent paradigm shift in recognizing thermodynamics does not always lead to competitive exclusion and zonation in anaerobic environments (Bethke et al., 2011) may allow for SRB and SOP/IOP to have a mutual relationship in the same localized area within a PRB.

2.3.3 Long-term Mechanisms of Contaminant Immobilization and Stability

The long-term production of sulfide in the presence of reduced Fe from the contaminant plume has resulted in an appreciable accumulation of Fe sulfide phases within the PRB. The maximum concentration of AVS in core PRB2021-1, 2 and 7 were 2,029, 1,634, and 1,921 μmol S g^{-1} respectively (**Figure 2.3**). Geochemical extractions of sub-sampled cored material from the PRB and aquifer reveal little difference in the abundance of AVS compared to TRS and total S in samples (**Figure A4**). The AVS extraction is operationally defined as targeting amorphous Fe monosulfides, mackinawite, greigite, and dissolved sulfide species. The TRS extraction is defined as targeting AVS phases as well as pyrite and elemental S. The similarity in results between AVS, TRS and total S suggests S is primarily immobilized as AVS phases in the PRB and downgradient aquifer. This result is inconsistent with aqueous geochemical results which suggest a secondary mechanism other than FeS precipitation is occurring based on the bulk removal ratio of 1.8 SO_4:1 Fe (**Table A3**). Sample heterogeneity and moisture content variability throughout the study area is attributed to some samples having AVS > total S or TRS.

There are two zones of S accumulations in the upgradient aquifer. The accumulation of S in the shallow portions of the aquifer is attributed to the formation of jarosite ($KFe_3(SO_4)_2(OH)_6$) and other hydroxysulfates due to AMD migration from the surface. Accumulation of AVS in deeper portions in

the upgradient aquifer is likely the result of sediment lenses with higher organic carbon content developing mildly reducing conditions.

Within the PRB, maximum concentrations of AVS are observed through the center portion of the barrier which may reflect heterogeneity in SO_4 reduction rates. Higher SO_4 reduction rates and higher AVS accumulation in the center of the PRB is consistent with the lowest groundwater Fe concentrations observed in the same portion and do not suggest a zone of preferential flow. The concentration of organic carbon is not consistent through the depth profiles of cores collected within the PRB as reflected in differences in total carbon (**Figure A4**). In zones with less organic carbon there is less accumulation of AVS. This is attributed to variability in reactive PRB material during installation and not exhaustion through microbial reactions. There does not appear to be an appreciable accumulation of AVS in the downgradient aquifer material despite there being no differences in SRB abundance. The migration of DOC from the PRB may support the growth and activity of SRB, however the lack of accumulation of AVS suggests conditions are not favorable for long-term stability.

A temporal comparison of bulk accumulation rates of TRS was conducted to evaluate accumulation of sulfide phases over the treatment lifespan of the PRB (**Table A5**). The TRS accumulation rates calculated for results collected in this study are higher than after 5.9 years of treatment, in different parts of the PRB (upgradient, middle and downgradient; Daignault, 2002). The accumulation rates are moderately decreased compared to rates at 1.9 years in the upgradient and downgradient portions of the PRB and greater in the middle portion of the PRB (Herbert et al., 2000). Some variability in these results may be due to accumulation rates being calculated along different transects of the PRB. Nonetheless, results would suggest accumulation rates have been consistent over the lifespan of the PRB after an initial two-year period where higher rates of SO_4-reduction and TRS accumulation occurred (Benner et al., 2002; Herbert et al., 2000). These results also support the conclusion that there is not a substantive difference in groundwater flow conditions along this studied transect, compared to previous investigations closer to the mid-line of the PRB, as slower groundwater flow rates would result in lower bulk accumulation rates.

A mineralogical investigation was conducted to further constrain the primary mechanism of contaminant immobilization within the PRB. Bulk S XANES spectra were collected on sampled material throughout the PRB (**Figure 2.5**). The dominant phase identified in all samples based on LCF fittings was FeS, in agreement with the geochemical extractions (**Table A6**). The organo-sulfur phase cysteine ($HOOC\text{-}CH\text{-}CH_2\text{-}SH$) was most prevalent in the upgradient and downgradient PRB

materials. Ferrous sulfate identified in samples is attributed to the freeze-drying process during sample preparation. While gypsum was identified in LCF fittings, there was not substantial accumulation in any measured sample. Geochemical modeling results suggest unfavorable conditions for gypsum precipitation.

Optical mineralogy and SEM revealed an abundance of Fe monosulfide in association with the organic carbon material (**Figure A7**). Iron monosulfides were commonly observed replacing plant cell wall material or filling intracellular spaces. Mineral identification was further refined by using XRF maps to target Fe and S hotspots followed by S μXANES which identified mackinawite and organo-sulfur species as the dominant phases based on LCF fitting (**Figure A8; Table A7**). Angai et al. (2022) observed similar mechanisms of Fe sulfide precipitation in ZVI organic carbon column experiments treating AMD. The presence of organo-sulfur species would suggest these phases were not fully targeted using geochemical AVS and TRS extraction methods and may be a likely secondary source of S immobilization.

Bulk Fe K-edge XANES were collected on sampled material from the PRB and downgradient aquifer (**Figure A9**). The results of the Fe XANES and LCF analysis of these spectra to identify primary Fe phases are confounding as all samples appear to have appreciable concentrations of Fe-oxide phases (**Table A8**). All samples from the PRB have some concentration of pyrite but FeS was not identified using LCF fitting. One sample (PBR21-2-5) had high concentration of magnetite (66%). These XANES analysis were performed by other researchers and time stamps suggest less than 24 hours between these measurements and S XANES, which were measured first, on the same sample group and suggest an appreciable concentration of FeS. Samples may have oxidized during this time compromising the Fe XANES results due to the sensitivity of FeS under atmospheric conditions. Optical mineralogy did identify Fe-oxide phases, however these did not appear to be the most abundant phases in areas examined. While these results are important to consider, additional lines of evidence suggest Fe is primarily immobilized as FeS.

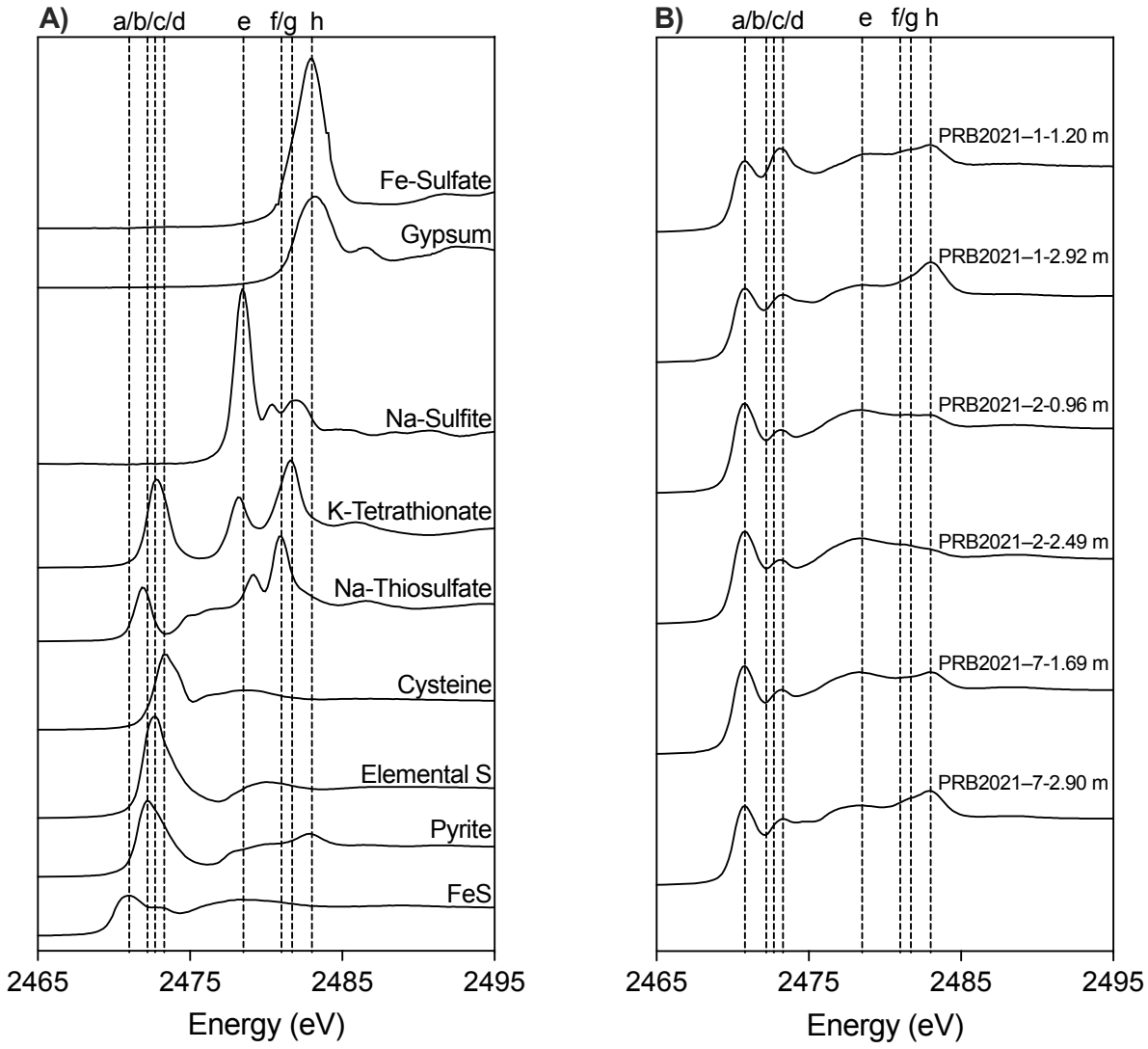


Figure 2.5. Bulk S XANES. A) S K-edge XANES of standards used for LCF fitting with vertical lines representing the maximum peaks of each standard. B) S K-edge XANES of sampled material. The vertical dashed lines correspond to the lines in A to allow for fingerprinting.

On occasion, Fe-sulfide precipitation was observed within the thin-section matrix intermingled with organic carbon material (**Figure A10**). Framboidal pyrite was identified in close association with other Fe-sulfide phases within plant cells and the extracellular matrix (**Figure A7**). However, the overall abundance of pyrite was limited and does not suggest a transition to pyrite as the primary long-term immobilization mechanisms. Experimental results suggest Ni can inhibit the transformation of mackinawite to pyrite when present at higher concentrations (Swanner et al., 2019) and may be occurring to some extent within the PRB. In natural systems the two primary pathways of pyrite formation from FeS are through reactions with H_2S and polysulfide (Rickard & Luther, 2007). The limited abundance of H_2S and polysulfide within the PRB may be limiting the rate of pyrite formation. In some instances, pyrite was observed forming on Fe-oxide phases but the opposite pattern was not observed (**Figure A10**).

Minerals containing Ni were not readily identified in the optical mineralogy and SEM investigation. Using XRF mapping, two hotspots were identified from which Ni K-edge μXANES spectra were collected (**Figure A8**). The sharp peaks observed between 8,352-8,353 eV are not a characteristic of native Ni or Ni-S phases. Linear combination fitting suggests Ni is sorbed onto Fe-oxides or in Ni-oxide phases (**Table A9**). A previous mineralogical investigation of the Nickel Rim PRB identified Ni immobilized as native metal with minor components of Fe-bearing Ni sulfate and potentially a Ni sulfate-phosphate (Jambor et al., 2005). Results of this study contrast with results of laboratory experiments where Ni in the presence of sulfide forms Ni-sulfide phases (Parigi et al., 2022a) or Ni-sorbed to mackinawite (Swanner et al., 2019). Freshly precipitated Ni-sulfide has been observed to possess significant residual Ni-O coordination (Parigi et al., 2022a; Wilkin & Rogers, 2010). If sulfide production from DSR is limited, the transition to Ni -S coordination that is observed in aged experimental tests may not proceed.

Geochemical modeling of aqueous geochemistry results suggests Fe-sulfide mineral precipitation is only favored in some locations within the PRB and downgradient aquifer (**Figure A2**). These calculations suggest unstable conditions for the previously precipitated sulfide minerals. The incongruence in the continued accumulation of Fe-sulfide phases and modeling results can be reconciled by low rates of SO_4 reduction and dual porosity within the PRB material. The organic carbon material supports SRB growth which results in the production of sulfide within the secondary pore space of the organic material. The rapid precipitation of Fe sulfide phases within these secondary pore spaces or replacement of organic carbon would limit the sulfide migrating into the macropore space. Groundwater sampling and subsequent geochemical modeling may be more representative of

the macropore space where conditions are less reducing and precipitated sulfides are more susceptible to abiotic and microbial recycling. Modeling results may also be affected by sampling and analysis error of redox sensitive and unstable parameters and Eh measurements. While efforts were made to collect representative groundwater samples for analysis, slow recharge of some monitoring wells and interaction with atmospheric conditions would bias water sampling results to indicate less reducing conditions.

2.3.4 Conclusions and Implications

Aqueous geochemical results demonstrate a high degree of Fe, Ni and SO_4 removal after 26 years of treatment. Bulk removal rates of Fe and SO_4 are similar to the removal rates calculated at 38 months of treatment suggesting sustained long-term treatment performance and that the initial 15-year treatment system lifespan under-estimated the potential of this treatment technology. Microbial community characterization identified SRB within the PRB and aqueous geochemical results paired with isotopic analysis of SO_4 suggests DSR is the primary driver of sustained treatment performance. There is no statistical difference in the abundance of SRB between the PRB and aquifer material, however there are distinct differences in the make-up of the SRB community with a diverse SRB community within the PRB. Analysis of the solid phase material and mineralogical characterization identified FeS precipitation as the primary mechanism of Fe and SO_4 attenuation in the PRB. This mechanism is consistent with initial studies of the Nickel Rim North PRB (Benner et al., 1999; Herbert et al., 2000). There is some evidence of the presence of sulfur cycling and formation of Fe-oxide mineral phases. The more complex solid phase organic carbon within the PRB may serve a dual purpose of supporting DSR over the treatment system lifespan and increasing the geochemical stability of secondary sulfide mineral precipitates to prevent remobilization of contaminants over time.

The initial 15-year treatment system lifespan under-estimated the potential of this technology. It was initially assumed treatment performance would be consistent with the simple G-model where reaction rates asymptotically approach zero over time (Benner et al., 2002; Westrich & Berner, 1984). Modeling organic carbon degradation, and thus long-term PRB performance, using the simple first order G-model may be inappropriate given the abundance of complex organic carbon in a PRB compared to ocean sediments in which the simple G-model was initially based. Rather, there appears to be an initial decline in treatment performance until a steady rate is reached which is likely controlled by the enzymatic degradation of more complex organic carbon sources such as cellulose in

wood chips. A focused comparison of the microbial communities present in a PRB at the onset of treatment to those observed in this study and PRBs that are not operating effectively is needed to identify the importance of enzymatic degradation of complex organic carbon in long-term treatment performance. Natural analogs such as wetlands or peat that intercept mine-impacted groundwater may yield the best estimates of potential treatment system lifespan. Future evaluations of this PRB, and evaluations of other PRBs treating mine-impacted groundwater on a multi-decadal timescale, will allow for further refinement of the overall potential of these systems and more realistic cost-benefit comparisons of a PRB to other treatment technologies.

More work is needed to account for changes to microbial community function during scale-up from bench-scale laboratory experiments to field-scale treatment systems to determine the long-term performance of various reactive media mixtures being tested. Sulfate reducing bacteria are a minor component in the microbial community that allow the PRB to perform over decades. Further research of the micro-organisms that provide organic carbon substrates to promote SRB growth and activity over decades is needed to exploit these microbial relationships in future PRB designs.

Long-term immobilization of S and Fe through the precipitation of FeS appears to remain consistent over decades of treatment. However, the confounding Fe XANES results suggest more work is needed to characterize the immobilization mechanisms in this treatment system. In addition to supporting the long-term performance of the PRB, the complex organic carbon sources promote stabile conditions for FeS precipitation, the predominant mechanism for contaminant immobilization. Mine-impacted groundwater treatment systems utilizing DSR that rely on more bioavailable carbon sources may have limited long-term contaminant stability if reducing conditions cannot be sustained.

***Chapter 3**: Incorporation of Emulsified Vegetable Oil into Organic-Carbon Permeable Reactive Barriers for Treatment of Mine-Impacted Groundwater: Column Experiments*

Executive Summary

Permeable reactive barriers (PRBs) that promote the growth and activity of sulfate reducing bacteria (SRB) and sustain high rates of dissimilatory sulfate reduction (DSR) are an established passive method of managing acid mine drainage (AMD). Four bench-scale column experiments were conducted to investigate emulsified vegetable oil (EVO) additions into a solid-phase organic carbon (OC) permeable reactive barrier (PRB) through two methods of incorporation: soaking OC with EVO prior to treatment and EVO injection. High-resolution aqueous sampling of both the effluent and pore-water over 300 days identified higher rates of metal removal, alkalinity generation, and reduced acid generation potential in columns with EVO compared to a control column containing the same solid phase reactive material. In addition, geochemical results after a second injection of EVO demonstrate re-establishment of treatment performance. The aqueous geochemical results combined with isotopic analyses and microbial community characterization provide insight into the microbiological processes occurring under different treatment conditions. Greater rates of sulfate and dissolved metal removal observed in columns with EVO are attributed to higher rates of DSR associated with differences in the availability of labile organic carbon and in the bacterial and archaeal community structure. Sulfate reduction rates varied along the column length in EVO columns and may reflect microbial reaction inhibition due to excess sulfide production. Sequential extractions and S-XANES on solid phase reactive material from each column identified FeS precipitation as the principal S removal mechanism. All treatments were effective at removing Ni. The experimental results demonstrate that optimized additions of EVO to OC PRBs can improve the extent and duration of initial treatment performance and subsequent EVO injections provide a means of re-establishing treatment in PRBs where treatment is not meeting objectives.

3.1 Introduction

Mining of sulfide ore deposits for economically important minerals can result in severe environmental impacts to water resources (España et al., 2005; Moncur et al., 2014). Modern and historic mining practices result in the massive accumulation of waste rock and tailings that contain sulfide minerals (ICOLD, 1996). Improper management can result in the exposure of these sulfide minerals to air and water leading to accelerated biotic or abiotic oxidation (Blowes et al., 2014), as represented by pyrite (FeS_2) oxidation:

$$FeS_{2(s)} + \frac{7}{2}O_2 + H_2O \rightarrow SO_4^{2-} + Fe^{2+} + 2H^+ \qquad [1]$$

The downgradient transport of low-quality pore-water results in a cascade of acid neutralization and mineral precipitation reactions unique to each site that act as a primary control on the release of weathering products (Blowes et al., 2014; Lindsay et al., 2015). The outcome of these reactions is the development of groundwater plumes characterized by neutral pH, high concentrations of SO_4, Fe(II), and low to moderate concentrations of other metals (R. H. Johnson et al., 2000; Lindsay et al., 2015). Surface discharge of this contaminated groundwater can result in Fe(II) oxidation (Blowes et al., 2014):

$$Fe^{2+} + \frac{1}{4}O_2 + \frac{5}{2}H_2O \rightarrow Fe(OH)_{3(s)} + 2H^+ \qquad [2]$$

There is significant risk to ecosystem and human health from the combined release of H^+ increasing the acidity, precipitation of metal (oxy)hydroxides and mobilization of metal contaminants (Hogsden & Harding, 2012; Wang et al., 2021). Environmental impacts associated with sulfide mine wastes can persist on the order of decades to millennia (Blowes & Jambor, 1990; Leblanc et al., 2000; Moncur et al., 2005) requiring long-term and costly remediation.

Over the past two decades passive bioremediation treatment systems designed to promote the growth and activity of sulfate reducing bacteria (SRB), such as sulfate reducing bioreactors (SRBR) and organic carbon (OC) permeable reactive barriers (PRB), have become established remediation practices for low-quality mine drainage due to their low cost of implementation, maintenance and monitoring (Adams et al., 2014; Neculita et al., 2007). These systems are designed to promote the growth of SRB and make use of dissimilatory sulfate reduction (DSR); a metabolic process that couples the oxidation of a variety of simple OC substrates, such as lactate, to the reduction of SO_4 to sulfide (Rabus et al., 2013):

$$3\,SO_4^{2-} + 2CH_3CHOHCOO^- \rightarrow 6HCO_3^- + 3HS^- + H^+ \qquad [3]$$

Treatment is expected to occur through precipitation reactions that immobilize metal contaminants within and immediately downgradient of the PRB. The production of aqueous sulfide species from DSR in the presence of dissolved metals can result in the precipitation of sparingly soluble metal sulfides with a preponderance of these being FeS (Herbert et al., 2000):

$$H_2S + Fe^{2+} \rightarrow FeS + 2H^+ \qquad [4]$$

Organic carbon PRBs are particularly advantageous as reactive media intercepts contaminant plumes *in situ*, allowing for passive treatment preventing oxidation of Fe(II) at discharge zones. *In situ* treatment limits the exposure of the treatment media to oxidants and temperature variations which results in more stable conditions for uniform rates of DSR year-round (Angai, 2020; Benner et al., 2002; Blowes et al., 2000).

A key consideration in designing an effective OC PRB is the long-term availability of suitable OC to support SRB and promote sulfidogenesis. Numerous studies have been conducted to optimize solid-phase reactive media to promote DSR and sustain treatment efficacy, with a mixture of locally available solid phase OC often utilized to provide an economical source for long-term passive treatment (Habe et al., 2020; Neculita et al., 2007). A primary limitation of solid phase OC is a finite treatment lifespan (Blowes et al., 2000). Often there are limitations on the rate and extent of degradation despite systems containing a sufficient volume of OC to theoretically sustain DSR for decades (Benner et al., 2002). Furthermore, the sustainable long-term rates of SO_4 reduction may not meet remediation objectives for the site (Gibert et al., 2011).

Re-establishing treatment system efficacy in an OC PRB requires reactive material removal, disposal and replacement: all steps that add appreciable cost to the remediation project (ITRC, 2011). Some treatment systems take a more active approach; relying on regular injections of readily biodegradable OC (*e.g.,* acetate, ethanol, and methanol) to maintain high rates of DSR (Glombitza, 2001; Tsukamoto et al., 2004). These liquid substrates have limited temporal and spatial effectiveness beyond the initial injection due to high microbial utilization rates and a propensity for biofouling (Li et al., 2009; Vrionis et al., 2005; Wu et al., 2006). The high financial and labor costs associated with the frequent injections (*i.e.*, daily or weekly) to maintain treatment conditions also limits widespread use in remote sites.

Amendments of emulsified vegetable oil (EVO) are very effective in promoting bioremediation *in situ* when injected into aquifers and tailings (Lindow & Borden, 2004; Watson et al., 2013). The latent microbial response due to the more complex organic structure of the vegetable oil allows for sustained treatment performance and wider distribution of the amendment. Incorporation of EVO into

solid phase OC PRBs may offer a synergistic effect for improved treatment. Furthermore, EVO may provide a means to re-establish treatment performance in older PRBs, or PRBs not reaching remediation objectives due to design flaws or age, without requiring removal and replacement. Combining solid phase OC with EVO amendments to treat mine-impacted groundwater shows great promise (Legrand et al., 2016).

In this study four bench-scale column experiments were conducted to investigate the incorporation of EVO into a solid phase OC PRB to remove metal contaminants and prevent AMD generation. Experimental columns were designed to evaluate the potential performance benefits of incorporating EVO into an OC PRB through both soaking and injection. To evaluate the ability of EVO to re-establish treatment performance, a second EVO injection was applied in one column. The aqueous geochemistry and microbial dynamics were investigated to gain insight into differences in treatment performance. A combination of solid-phase analyses and geochemical modeling was used to interrogate the primary mechanisms of contaminant immobilization.

3.2 Methodology

3.2.1 Column Design and Experimental Setup

Four flow-through column experiments were conducted in acrylic columns 39.3 - 41.2 cm long with a 7.6 cm internal diameter. Solid-phase reactive material, composed of 49.5 vol. % silica sand (SS; ASTM 20-30, U.S. Silica Company), 0.5 vol. % pulverized limestone (Beachville Quarries), and a combination of 40 vol. % leaf mulch and 10 vol. % wood chips as the solid phase OC, was the same in each column. The leaf mulch and wood chips, obtained from the Region of Waterloo Cambridge Landfill in March, 2021, were sieved to < 3/8” and pieces larger than 10 mm in one-dimension were removed by hand. The EVO (EOS Pro, EOS Remediation LLC., Research Triangle Park, NC) was stored at 4°C prior to use. The mixture of OC was prepared manually with SS to facilitate homogeneous flow conditions. Limestone was added to increase the acid buffering capacity of the material to aid in establishing and maintaining microbial populations. The moisture content of each material can be found in **Table B1**. Microbial populations were established by dispersing approximately 10 g of organic-rich sediment and water inoculum through each column. The inoculum originated from anaerobic sediment in Laurel Creek, Waterloo, Ontario that was incubated and maintained in the laboratory on stock solutions high in SO_4, metals and lactate.

The four flow-through column experiments: control column (CC); EVO soaked column 1 (EVOS1); EVO soaked column 2 (EVOS2); and EVO injection column (EVOI); are differentiated by the quantity of EVO and mechanism of EVO incorporation into the reactive material (**Table 3.1**). No EVO was incorporated into CC. The leaf compost component of EVO soaked columns (EVOS), EVOS1 and EVOS2, was homogenized and soaked in 100 mL (95 g) of EVO for 24 hours prior to packing the columns. Two injections of a 100 mL 1:4 EVO: influent mixture were added to the EVOI through the influent port of the column. The first occurred at the onset of flow and the second at 40 pore volumes (PVs); after a decline in treatment performance was observed. These injections occurred at a rate of < 10 ml $min.^{-1}$ to prevent the development of preferential flow pathways in the reactive material.

Table 3.1. Column experiment composition of the solid phase reactive material by volume %. The amount of solid phase reactive material (including bacterial inoculum) and EVO is indicated for each column. The reactive material density was determined from the solid phase reactive material mass (wet) and volume determined from the volume of material in the column.

Column Name: Identifier	< 3/8" Leaf Compost	< 3/8" Wood Chips	Silica Sand	Limestone	Solid Phase Reactive Matrix	EVO	Solid Phase Reactive Material Density
	(vol. %)	(vol. %)	(vol. %)	(vol. %)	(g)	(mL)	(g cm^{-3})
Control: CC	40	10	49.5	0.5	2,068	0	1.27
EVO Injection: EVOI	40	10	49.5	0.5	1,996	20	1.22
EVO Soaked 1: EVOS1	40	10	49.5	0.5	2,059	100	1.28
EVO Soaked 2: EVOS2	40	10	49.5	0.5	2,060	100	1.29

Each column was outfitted with influent and effluent ports, six profile pore-water ports, and eight profile solid sampling ports. The distribution of these ports along the length of the column varied, with increased sampling density at the inlet end of the reactive material (**Figure 3.1**). Filter layers which included a coarse and fine NITEX™ screen and SS were placed at the base and top of the reactive material to provide uniform flow distribution. In each column ~ 36 cm of reactive material was added and packed in 1-2 cm lifts to maintain consistent density. Slight differences in overall column height were accounted for by varying the depth of inert SS at the column base rather than the volume of reactive material. All columns, influent and effluent lines were wrapped in aluminum foil to prevent growth of phototrophic microorganisms. The columns were purged with

$CO_{2(g)}$ for 2 hours prior to saturation. The EVOS2 column was started 7 days after CC, EVOI, and EVOS1.

Using a multi-channel peristaltic pump (Ismatec and Rainin Dynamax) water was pumped from the influent port in the column base upward. Effluent flowed through a 125 mL amber glass bottle, which was used to collect samples inside the anaerobic chamber. A combination of Pharmed® BPT tubing and Teflon tubing connected the influent bottle, column and sample vessel. Effluent was discharged into 4 L capped polyethylene (PE) bottles outside the anaerobic chamber for gravimetric measurements to determine total discharge volumes. The effect of evaporative loss on these gravimetric measurements was measured at a rate of 0.33-0.66 mL d^{-1}.

Column influent solution was prepared to simulate mine impacted groundwater entering a PRB in Sudbury, Ontario (Benner et al., 1999) by adding $CaSO_4$, $FeSO_4 \cdot 7H_2O$, $MgSO_4 \cdot 7H_2O$, $MnSO_4 \cdot H_2O$, and $NiSO_4 \cdot 6H_2O$ to deionized water sparged with $CO_{2(g)}$ and saturated with $CaCO_3$. The influent solution was circumneutral in pH and had high concentrations of dissolved SO_4^{2-}, Fe(II) and Ni(II) (**Table 3.2**). Influent batches were prepared in a 4 L amber glass bottle every 5 days under anaerobic conditions and sparged with $Ar_{(g)}$ for a minimum of 6 hours prior to $FeSO_4 \cdot 7H_2O$ addition. The pH of the solution was adjusted using either powdered $CaCO_3$ or 95-98% A.C.S., reagent-grade H_2SO_4 and sampled to ensure consistency between batches. Starting on day 9 (3.2-3.8 PV) of experimental flow for CC, EVOI and EVOS1, NaBr was included in the influent solution batches for all columns to serve as a conservative tracer. Sodium bromide was added for 12 days in total and terminated on day 21 (5.4-6.4 PV).

Initially, the columns were saturated over 24 hours using influent solution without $FeSO_4 \cdot 7H_2O$ outside the glove box to check for leaks and determine saturated mass. After an initial period of flow (~2 saturation volumes equivalent), column flow was paused and columns were transferred to the anaerobic chamber and then allowed 7 days of low flow conditions (~100 mL d^{-1}) to promote bacterial growth. Experimental flow began with influent containing Fe(II) on day 10-12 (1.3-1.8 PV).

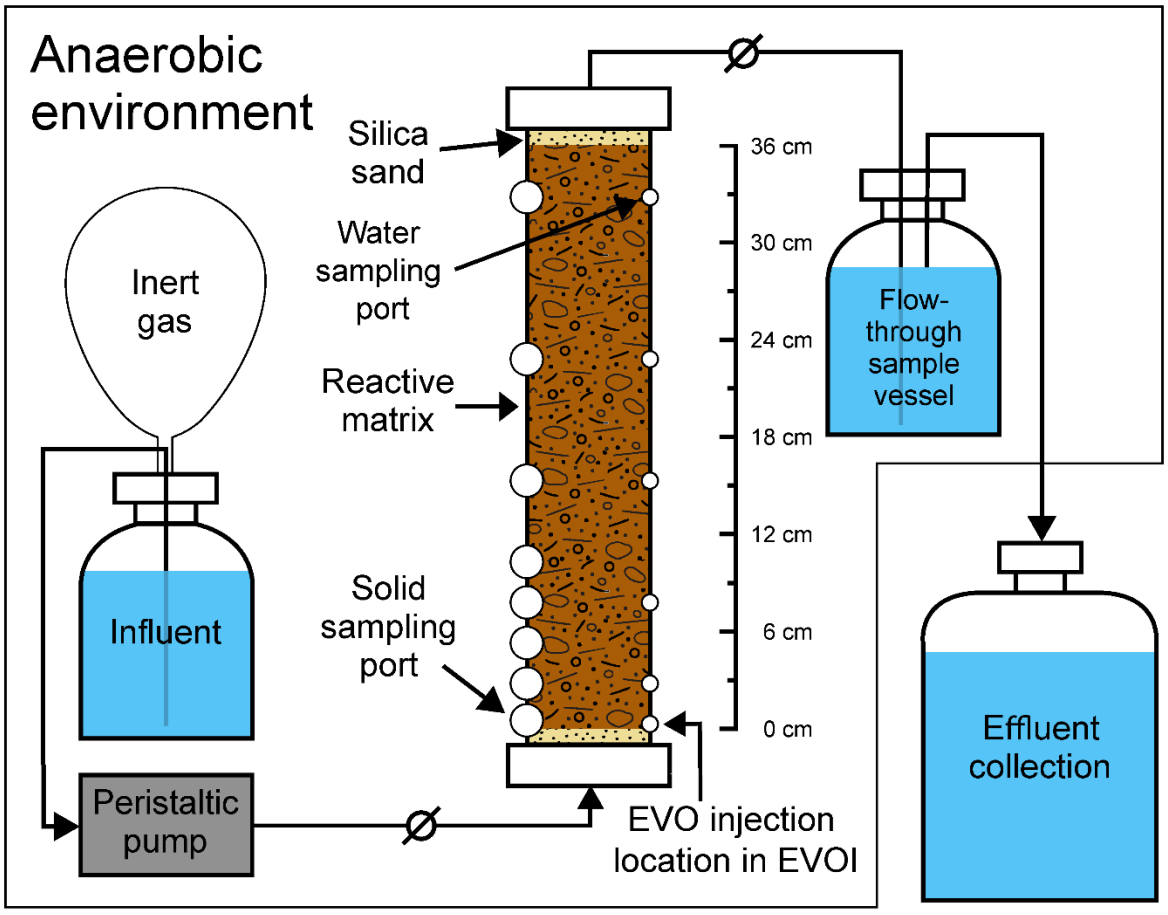


Figure 3.1. Schematic diagram of column experiment setup and design. Influent was pumped into the bottom of each column in an anaerobic glovebox. Profile pore-water and solid-phase sampling ports were used to sample the columns over the course of the experiment. The lowest water sampling port was also used for EVO injection in EVOI.

Table 3.2. Influent solution aqueous geochemical composition.

Parameter	Column Saturation and Acclimation Influent (n=4)			Experiment (n=64)		
	Mean Column Influent	Standard Deviation	Number of Measurements	Mean Column Influent	Standard Deviation	Number of Measurements
pH	-	-	0	6.64	0.34	64
Eh (mV)	-	-	0	-15.9	67	64
Alkalinity (mg L^{-1} as $CaCO_3$)	213.3	-	1	15.5	19	58
SO_4 (mg L^{-1})	1,642	335	4	2,908	180	52
Fe (mg L^{-1})	0	0	4	709	28	53
Ni (µg L^{-1})	4,350	310	4	4,867	387	53
Ca (mg L^{-1})	397	127	4	335	41	53
Mg (mg L^{-1})	287	7	4	281	7.3	53
Mn (mg L^{-1})	9	3	4	11	0.9	53
Sulfide (µg L^{-1})	-	-	0.0	0	0.0	31
DOC (mg L^{-1} as C)	18.05	25.1	2	3	7	9
Br* (mg L^{-1})	-	-	-	108	2.8	3

**NaBr included for 3 batches (13 days) as a conservative tracer. All other Br concentrations were at the detection limit and not included in the statistics presented*

3.2.2 Sample Collection

3.2.2.1 Effluent, influent and Profile Pore-water Sampling

Water sampling was conducted under anaerobic conditions with the effluent collected accounted for in discharge volume determinations. Influent samples were collected for each new batch of solution every 7 days (~3-4 PV). Column effluent sampling was variable with increased frequency at the start of the experiments with sampling occurring every day (~0.3 PV). During the tracer tests, column effluent samples were collected up to three times a day (~0.05 PV). Effluent sampling frequency decreased to 1 week intervals (~1 PV) after the tracer test and 2 week intervals (~2 PV) after week 44. Pore-water profile sampling was conducted on weeks 11, 24, and 44. Profile sampling provides geochemical characterization along the flow path. Pore-water sampling started with the effluent and

moved sequentially to the next upgradient profile port every 12 hours. Samples were collected in capped 125 mL amber glass bottles connected via Teflon tubing to Luer locks on the profile sampling port. Pore-water sub-samples were drawn from the amber glass bottles using a 50 mL polypropylene (PP) Luer lock syringe.

Unfiltered sub-samples were used for pH and Eh measurements and volatile solids analysis. Migration of EVO into the sample vessels during the first 3 PV for EVOI, EVOS1 and EVOS2 resulted in probe interferences, so these sub-samples were filtered (0.45 µm nylon). The remaining sub-samples collected from influent, effluent and pore-water for all columns were filtered (0.45 µm nylon). Sub-samples for anion, cation, and aqueous SO_4 isotope measurements, were transferred into high density polyethylene (HDPE) bottles. Samples for dissolved organic carbon (DOC) and volatile solids analysis were transferred into amber glass bottles with minimal headspace. Cation sub-samples were preserved with trace metal grade HNO_3, and DOC were preserved with 95-98% A.C.S. reagent H_2SO_4, to a pH of <2. If measurable sulfide was detected in the sample, sub-samples for SO_4 isotopes were allowed to degas H_2S under atmospheric conditions for 20 minutes, before being capped and stored. All sub-samples were stored at 4°C prior to analysis.

3.2.2.2 Solid-Phase Sampling

Two solid phase sampling events occurred and were conducted in an anaerobic chamber with anaerobic conditions confirmed using dry anaerobic indicator strips (BD BBL™ Gas Pak™). Profile solid-phase sampling for mineralogical and DNA extraction occurred after the first pore-water profile sampling (week 12) for mineralogical analysis and DNA extractions. The first sampling was conducted by clamping the influent and effluent lines, turning a column to horizontal and using a sterilized scoopula to remove ~15 g of reactive material from the profile sampling ports, which was then replaced with SS. The second sampling event occurred at the end of the experiment (week 45) when each column was destructively sampled, working from the base upwards in 1-3.5 cm increments, for mineralogical analysis. Sampled material was stored in sterilized PP centrifuge tubes. Sub-samples for mineralogy and physical characteristics determination were stored in HDPE bottles. All sub-samples for DNA extraction were immediately stored at -80 °C and all other sub-samples were stored at -20 °C prior to further sample preparation.

3.2.3 Analytical Methods

3.2.3.1 Aqueous Analyses

The pH was measured on a fresh water sample using a combination pH electrode (Orion A321 meter with and Orion triode temperature compensating gel filled pH probe) and the Eh was determined using a platinum combination electrode (Orion 3 Star meter with Orion 9678 BN redox electrode and VWR Symphony combination epoxy electrode with Orion 9000001 filling solution) and corrected to the standard hydrogen electrode; See supplement B1). Alkalinity and dissolved aqueous sulfide (S^{2-}) were measured immediately outside the glovebox. Alkalinity was measured in duplicate or triplicate using a digital titrator and the bromocresol green/methyl red indicator and standardized H_2SO_4 (Hach Method #8203). Aqueous S^{2-} was determined using a Hach spectrophotometer (DR2800) and the methylene blue method (Hach Method #8131) with duplicate or triplicate measurements taken when sample volume permitted. Samples beyond the calibration range for S^{2-} were diluted gravimetrically with DI sparged with $Ar_{(g)}$. Influent, effluent and pore-water samples were analyzed at the University of Waterloo Groundwater, Geochemistry and Remediation Laboratory for anions (including volatile organic acids; Dionex DX6000 ion chromatograph), major cations (Thermo Scientific iCap 6000, ICP-OES), trace elements (Thermo Scientific X-series 2, ICP-MS), and DOC using combustion (Aurora 1030W total organic carbon analyzer).

3.2.3.2 Sulfur and Oxygen Isotopic Measurement from Aqueous Sulfate

A subset of water samples was analyzed for $\delta^{34}S$ and $\delta^{18}O$ in SO_4. $BaSO_4$ was precipitated at the University of Waterloo (See supplement B2) and analyzed at the University of Calgary Isotope Science Laboratory - Applied Geochemistry Group for both S and O isotopic ratios. Ratios of $^{34}S/^{32}S$ were measured using combustion/ reduction reactor (Carlo Erba NA 1500® elemental analyzer) interfaced (via a Conflo-III® device) to a continuous-flow mass spectrometer (CF-EA-IRMS; Thermo Delta+XL®). $^{18}O/^{16}O$ ratios were measured using a high temperature reactor (Heka High temperature oxygen analyzer) and interfaced (via a Conflo-III® open split/interface) to a CF-EA-IRMS (Thermo Delta+XL®). Oxygen and S isotopic compositions are reported in standard delta notation as per mil (‰) deviations from Vienna Standard Mean Ocean Water (VSMOW) and Vienna Cañon Diablo Triolite (VCDT) respectively.

3.2.4 Microbial Characterization

Microbial community characterization was conducted using high throughput amplicon sequencing of 16S ribosomal ribonucleic acid (rRNA) genes on 36 week 12 solid phase subsamples. Total genomic material was extracted using Sox DNA isolation kit (v. 14.7; Metagenome Bio Inc.) following manufacturer methods for samples with high humic acid content and stored at -80 °C prior to 16s rRNA gene amplicon sequencing (Metagenome Bio Inc.; Toronto, On).

The V4 region of 16S rRNA genes was amplified with illumina MiSeq sequencing using the modified universal primers 515F/806R (Walters et al., 2016). Sequencing data was processed using the Mothur program (Schloss et al., 2009) and Mothur MiSeq standard operating procedure (Kozich et al., 2013). Duplicate sample populations (n=4) from each column were compared on the phylum and genus level before being merged for further data processing due to their high level of similarity (**Figure B1**). Taxonomic investigations utilized clustering of the operational taxonomic units (OTU) at a 97% similarity level using a *de novo* OTU picking process. Taxonomic annotation used the Silva database (release 132 for Mothur, download 18/03/2019) as reference. Several taxa (unknown, mitochondria, eukaryotes) were not used in subsequent analyses while Cyanobacteria were retained.

Relative abundances of putative SRB, iron-oxiding microorganisms (IOM), sulfur-oxidizing microorganisms (SOM), methanogens, and methylogens were obtained by screening the taxonomy file for prokaryotic genera containing at least one species with the investigated metabolic trait. Higher taxa were used when genus level identification was not possible. Prokaryotic diversity was investigated in the data set with unmerged duplicate samples. Microbial α-diversity for each library was measured using the Gini-Simpson's diversity index (1-D) and Chao richness estimator. Good's coverage was used to assess how representative the samples were of the environments from which they were taken with three samples having low Good's coverage (53.7 to 64.5 %; **Table B2**) removed before β-diversity investigations using UniFrac to compare bacteria and archaeal communities at the genus level (Lozupone & Knight, 2005). The UniFrac analyses are visualized using 2D non-metric multidimensional scaling (2D-NMDS) plots. The analysis of molecular variance (AMOVA) was used to determine if differences in prokaryotic β-diversities in samples collected from different columns are significant. An overview of 16S rRNA gene sequence data statistics can be found in Supplementary Information B3 and **Table B2**.

3.2.5 Solid-Phase Characterization

3.2.5.1 Solid-Phase Sample Preparation and Bulk Material Characteristics

Sub-samples were freeze dried. The difference in mass before and after drying was measured and used to calculate moisture content. Twenty-five percent of samples were collected in duplicate. Sample for C/S analyses were crushed to <250μm using a ball mill.

3.2.5.2 Carbon and Sulfur Analyses

Total C and S contents were determined (Eltra CS 2000 C/S determinator equipped with an induction and resistance furnace) and inorganic C content was calculated by measuring the total C in a pre-fired sample (500 °C for 1 hour).

Selective extractions were used to determine the abundance of solid phase S species. A hot 6N HCl with $SnCl_2$ extraction was conducted to quantify the acid volatile sulfides (AVS) fraction (Rice et al., 1993). The chromium reducible sulfur (CRS) method was used to quantify the total reducible sulfur (TRS) fraction (Canfield et al., 1986). Details on the extraction methods, standards and the standards recoveries can be found in Supplementary Information A4 and **Table A2**.

3.2.5.3 X-Ray Absorption Spectroscopy

Sulfur K-edge X-ray Absorption near-edge structure (XANES) spectra were collected on the soft X-ray micro-characterization beamline (SXRMB) at the Canadian Light Source (CLS). Freeze dried samples were powdered in the glovebox and transported to the beamline in an anaerobic cannister. Samples and standards were prepared for analysis by spreading thin layers of powdered material on double-sided tape and mounted on a copper plate. Samples were analyzed under vacuum. Spectra were collected between 2,442 eV and 2,552 eV with a 2.0 eV step size from 2,442 to 2,466 eV, a 0.1 eV step size from 2,466 eV to 2,492 eV, and a 0.8 eV step size from 2,492 eV to 2,552 eV. Multiple scans were collected and merged prior to data processing to improve the signal-to-noise ratio and enhance data analysis. Data processing including; energy calibration, multiple scan averaging, and normalization was conducted using Larch (Newville, 2013). A $CaSO_4$ standard spectra was used for E° correction of S K-edge standards collected previously (ESRF, 2023; He et al., 2010; Liu et al., 2016) for linear combination fitting (LCF). The best-fit LCF results are reported based on constituents in the fit and minimized $\chi 2$ (**Table B3**).

3.2.6 Data Interpretation

3.2.6.1 Tracer Test and Transport Parameter Determination

The bromide breakthrough curves were modeled using the computer program Stanmod (Simunek et al., 1999) and the CXTFIT code (v. 2.1; Toride et al., 1995). The measured data was fit with the deterministic equilibrium convection dispersion equation (CDE) transport model with a Dirichlet input boundary (See Supplement B4). The fitted parameters from CXTFIT were used to determine the PV for each column used in plotting aqueous geochemical results.

3.2.6.2 Sulfate Removal Rates

Sulfate removal rates were calculated for each column using pore-water results from the first sampling event of all columns. In addition, the second and third sampling event were fit for EVOI. A simple linear regression was for the CC dataset and second EVOI sampling event. A one-phase decay model was used for the first and third sampling event of EVOI and the EVOS columns.

3.2.6.3 Saturation Indices

Saturation indices were determined using the geochemical modeling software PHREEQC (v. 3.6.2.15100; Parkhurst & Appelo, 2013) using the MINTEQ V4 thermodynamic database (Allison et al., 1998) modified to be consistent with WATEQ4F (Ball & Nordstrom, 1991). In these simulations volatile organic acids are considered in alkalinity determinations and total alkalinity had to be increased from measured values to allow some sample simulations to converge. The measured pe (converted from Eh) was used to determine concentrations of redox couples.

3.3 Results

3.3.1 Column Flow Characteristics and EVO Mobility

Column experiments were conducted for 315 days for CC, EVOI and EVOS1 and 309 days for EVOS2 (**Figure B2**). The cumulative discharge for CC, EVOI and EVOS2 was similar (56.9-57.2 x 10^3 cm^3) with consistent flow rates (mean 7.5-7.7 mL h^{-1}; **Table B4**). An interruption in flow occurred in EVOS1 due to a brief clog in the effluent line at ~210 days resulting in a lower mean flow rate (7.2 mL h^{-1}) and cumulative discharge (54.7 x 10^3 cm^3). Initial pore volume estimates were calculated gravimetrically from the difference in the initial saturated and unsaturated mass of the column (**Table B4**). The EVOS columns had a lower PV than CC using this method of gravimetric PV calculation. The observed and simulated Br^- breakthrough curves showed good agreement (**Figure B2)**. The coefficient of determination for the CXTFIT models indicate a good fit to observed results when using the deterministic equilibrium CDE (mean R^2= 0.92; **Table B5**). Simulated results indicated minor variations in pore-water velocities and dispersion coefficients between columns, with CC having a higher pore-water velocity (8.9 cm d^{-1}) than EVO columns (7.1-7.8 cm d^{-1}; **Table B5**). The PV, porosity, residence time, and total PVs were determined using the CXTFIT model results (**Table B5**). The column PVs calculated from modeled results were greater than the gravimetric results with the largest increases observed in the EVOS columns. The higher pore-water velocity in CC resulted in a shorter residence time (4.4 days) and greater number of total PVs (71.1).

Preferential migration of EVO was visible after the first injection of EVO in EVOI with EVO present in the effluent collection vessel the following day (**Figure B3**). Migration of EVO out of the column was not observed in the EVOS columns at the onset of flow or after the second injection of EVO in EVOI. Attempts to track EVO migration out of the columns using volatile solids analysis via combustion were not successful.

3.3.2 Geochemical Conditions

3.3.2.1 General Water Quality

The geochemical conditions in CC, EVOI, EVOS1, and EVOS2 vary temporally and between test conditions (**Figure 3.2**). In general, both the effluent and pore-water profiles over the length of each column were consistent with the influent pH 6.64 ± 0.34 (mean ± standard deviation; **Figure 3.2 & 3.3**). A decrease in pH to ~5.5 in EVOS columns effluent was observed over the first 15 PV before

approaching the influent with continued flow. In the first profile sampling event for EVOS columns, a similar decline in pH was observed in the lower ~10 cm.

Influent Eh was variable with a mean of -15.9 ± 67 mV. Initially all column effluent Eh values were negative. There was a progressive shift to positive Eh values in CC and EVOI over the course of the experiment. No notable shift in Eh was observed with the second injection of EVO in EVOI. The EVOS effluent Eh was consistently negative (-102 ± 30 mV; mean ± standard deviation). Pore-water Eh in CC and EVOI was generally consistent with the influent for all three sampling events. In EVOS, pore-water Eh was < -20 mV, with the exception of a pronounced shift to values >17 mV in the lower portion of the columns during the second and third sampling event.

Influent alkalinity was low with a mean of 15.5 ± 18.8 mg L^{-1} as $CaCO_3$. The effluent alkalinity in all four columns markedly increased, with maxima between 1,070-1,954 mg L^{-1} as $CaCO_3$ for the first 6-10 PV. Effluent Ca maxima (825-1,048 mg L^{-1}) were also observed during this period. After the initial peak, CC effluent alkalinity and Ca decreased rapidly and became consistent with the influent. The alkalinity and Ca concentrations of the EVOI effluent approached influent values prior to the second injection of EVO. A smaller transitory peak in EVOI effluent alkalinity concentration (~500 mg L^{-1} as $CaCO_3$) proceeded the second injection of EVO while Ca concentrations remained consistent with the influent values before increasing during the decline in alkalinity concentrations. The EVOS effluent alkalinity remained elevated at ~500 mg L^{-1} as $CaCO_3$ until 30 PV, when the alkalinity began to gradually decrease in both columns. The Ca concentration in EVOS effluent remained elevated throughout the duration of the experiment. Alkalinity and Ca increased along the flow path in all columns during every profile sampling event with a greater magnitude increase occurring in columns with EVO. In the third sampling event for EVOS, and the second sampling event for EVOI, alkalinity was lower in the upper half of the column pore-water.

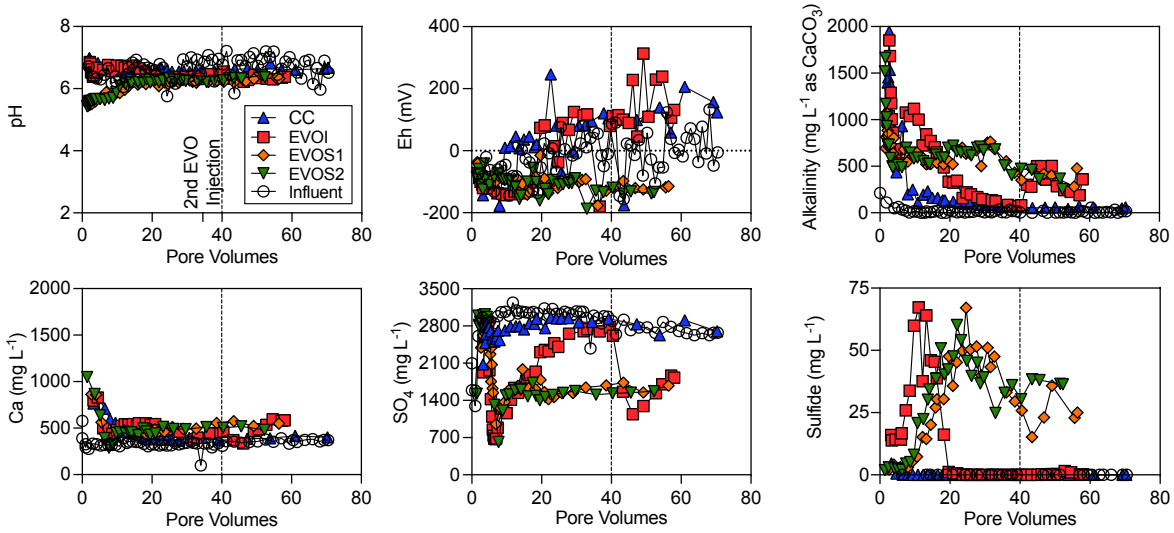


Figure 3.2. pH, Eh, alkalinity, Ca, SO_4 and sulfide versus pore volumes (PV) in influent and effluent of the four column experiments. The dashed line at 40 PV indicates when the second injection of EVO occurred in the EVOI column. The influent and column effluents are differentiated by shape and color.

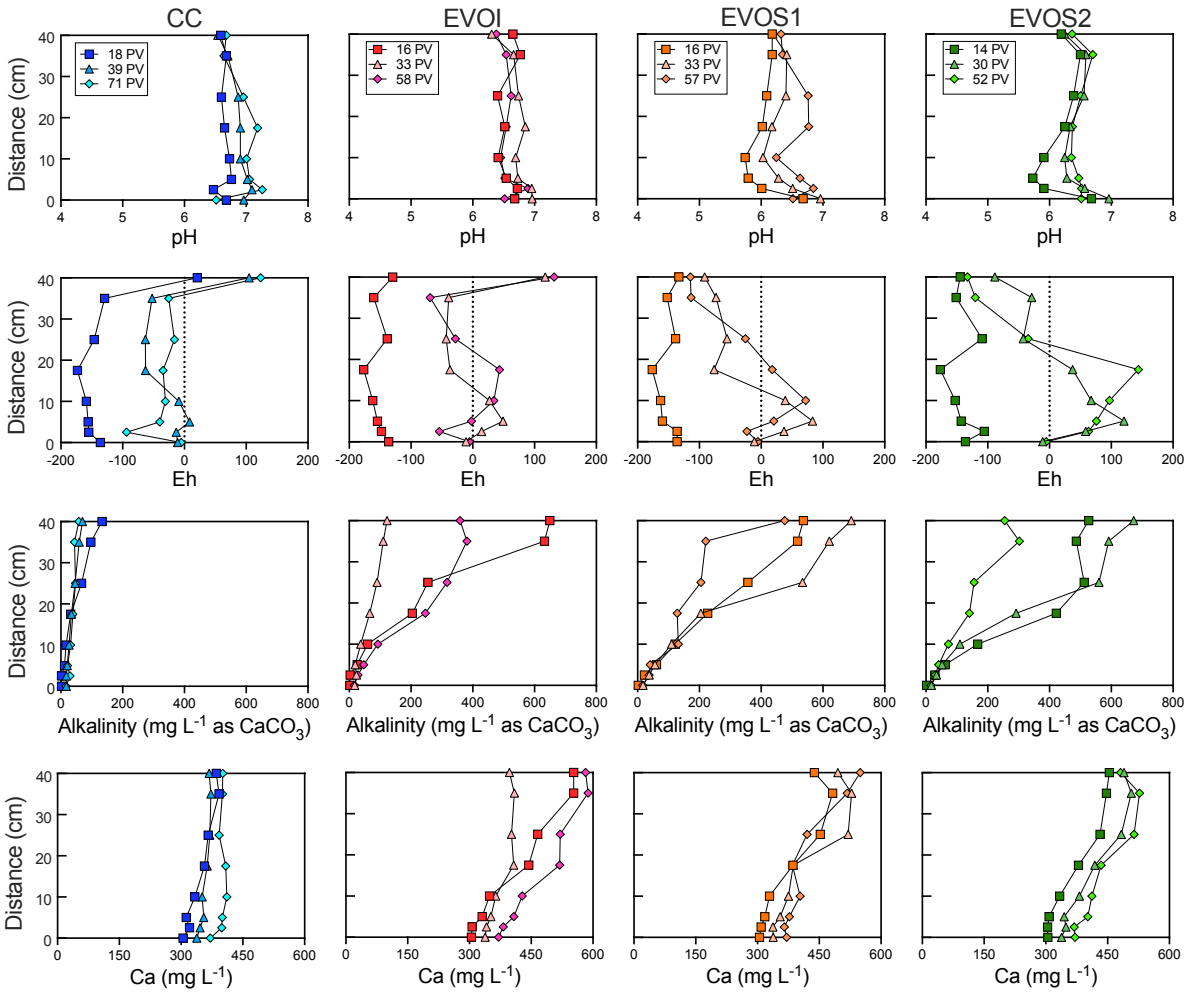


Figure 3.3. pH, Eh, alkalinity, and Ca in pore-water samples from CC, EVOI, EVOS1, and EVOS2 during three sampling events. The three sampling events are labeled according to the approximate pore volume (PV) of sampling and differentiated by different color shade and shape. Distance 0 cm represents the influent concentration and distance 40 cm represents the effluent concentration.

3.3.2.2 Dissolved Organic Carbon and Volatile Organic Acids

There was little to no measurable DOC or volatile organic acids (VOA) in the influent (**Figure 3.4**). At the onset of treatment, the DOC and VOA concentrations were elevated in all column effluents. The EVOS2 effluent exhibited the highest concentrations with maximums of 3,122 mg L^{-1} DOC as C, 1,151 mg L^{-1} acetate as C, 3,107 mg L^{-1} propionate as C and 162 mg L^{-1} formate as C. Concentrations of DOC and acetate decreased rapidly in the effluent of CC and EVOI while remaining elevated in the EVOS column effluents. There was a modest increase in DOC or VOA in the EVOI effluent after the second injection of EVO. Propionate and formate concentrations rapidly decreased in all four columns. Volatile organic acids were not elevated in pore-water in profile samples with the notable exception of acetate in EVOS columns where concentrations increased linearly from the base in the first and second sampling event and after 20 cm in the third sampling event (**Figure B4**).

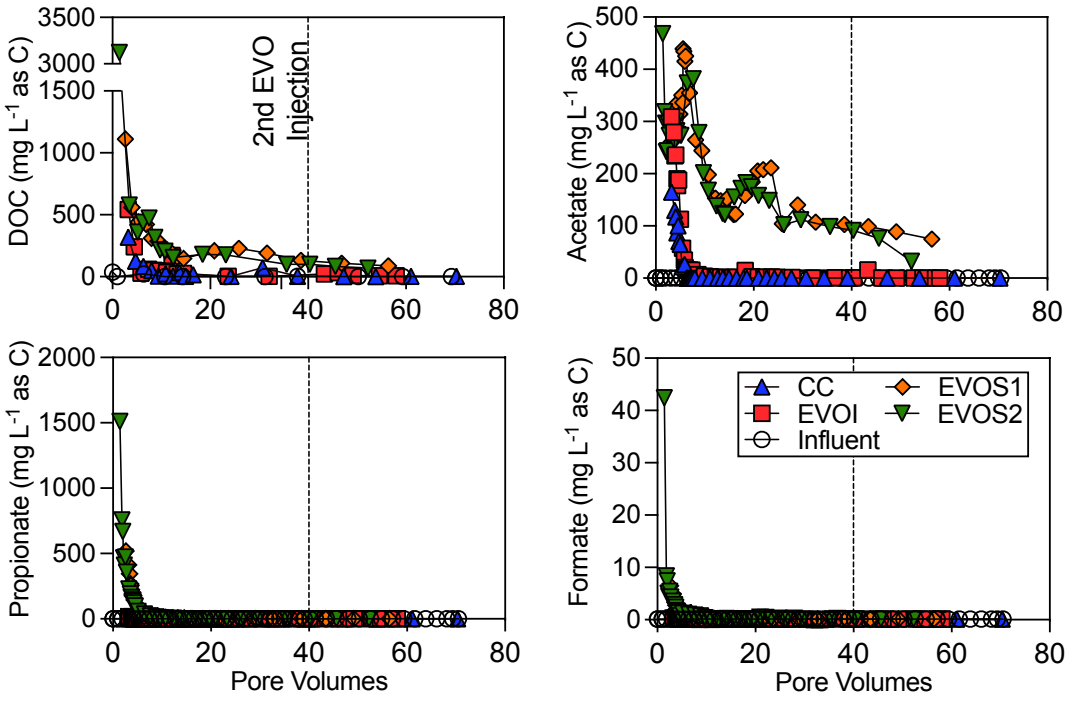


Figure 3.4. Concentrations of dissolved organic carbon (DOC), acetate, propionate, and formate in column influent and effluent.

3.3.2.3 Sulfur Geochemistry

The mean influent SO_4 was 2,908 mg L^{-1} with concentrations linearly decreasing from ~3,100 mg L^{-1} to ~2,800 mg L^{-1} over the duration of the experiment (**Figure 3.2**). The maximum influent S^{2-} measured was 3 μg L^{-1}(**Figure 3.2**). At the beginning of treatment all column effluents had measurable S^{2-}. At 6-8 PV the CC effluent minimum SO_4 of 2,509 mg L^{-1} occurred together with the minimum effluent concentrations of ~600 mg L^{-1} for EVOI, EVOS1, and EVOS2. Control column effluent SO_4 approached influent concentrations, after the observed minimum, with no pronounced removal observed after 20 PV for the duration of the experiment. This increase in SO_4 coincided with a decline in measurable S^{2-} concentrations. Pore-water SO_4 in CC was generally consistent with the influent concentrations with little to no S^{2-} measured in all three sampling events (**Figure 3.5**). A notable increase in SO_4 concentrations was observed above influent concentrations at 20 cm in the third CC profile sampling event.

Following the measured EVOI effluent SO_4 minimum, a maximum effluent S^{2-} concentration of 67 mg L^{-1} was observed at 11 PV before sharply decreasing and approaching 0 mg L^{-1} after 20 PV. The EVOI effluent SO_4 increased and approached influent concentrations prior to the second EVO injection (40 PV). Pore-water SO_4 concentrations in EVOI decreased in the first sampling event (16 PV) with a sharp decline observed in the lower 20 cm of the column and S^{2-} only measured in the upper sampling points. There was a modest linear decrease in pore-water SO_4 in the second sampling event (33 PV) prior to the second EVO injection with minimal S^{2-} measured. After the second EVO injection, a rapid transient decrease in EVOI effluent SO_4 to secondary measured minimum of 1,137 mg L^{-1} occurred after 6 PV (46 PV total) before progressively increasing to the end of observation. A small increase in EVOI effluent S^{2-} was also observed. Concentrations of SO_4 in EVOI pore-water at the end of the experiment were consistent with the first pore-water sampling event, however there was only a modest increase in S^{2-}.

Effluent SO_4 concentrations from EVOS columns were similar; increasing rapidly from the observed minimum at 7 PV to a plateau after 12 PV and remaining consistently around ~1,600 mg L^{-1} for the duration of the experiment. Shortly after SO_4 values became consistent, maximum S^{2-} of 67.1 mg L^{-1} at 25 PV and 60.2 mg L^{-1} at 22 PV were observed in the EVOS1 and EVOS2 effluent respectively. In EVOS columns, pore-water SO_4 decreased in the lower 25 cm to a minimum where values remained consistent for the duration of the column length in all three sampling events. Inversely, S^{2-} increased and plateaued above 15 cm in all three sampling events.

Pore-water sulfate $\delta^{34}S_{SO_4}$ and $\delta^{18}O_{SO_4}$ ratios were determined for pore-water sampling events from CC, EVOS1 and EVOS2 (**Figure 3.5**). Precision and accuracy as σ of 10 standards measured at the University of Calgary is 0.5‰ for $\delta^{18}O_{SO_4}$ and 0.3‰ for $\delta^{34}S_{SO_4}$. Pore-water $\delta^{34}S_{SO_4}$ in CC are consistent with the influent in both the first and third sampling event. In the first sampling event pore-water $\delta^{34}S_{SO_4}$ increased by 10.3‰, 8.3‰, and 9.6‰ in EVOI, EVOS1 and EVOS2 respectively. In the second and third sampling event, EVOI pore-water $\delta^{34}S_{SO_4}$ increased by 3.6‰ and 6.4‰ respectively. Pore-water $\delta^{18}O_{SO_4}$ measurements in all four columns suggest there were very little shifts from influent values along the column length.

Sulfate removal rates were calculated using the pore-water data with fundamental differences in the pattern of bulk SO_4 removal in columns with EVO (**Figure B5**). The first sampling event from CC and the second sampling event in EVOI were consistent with a zero-order rate equation $C = k_o t$ where C is pore-water SO_4 concentration (mg L^{-1}), t is the residence time (days) and k_o is the zero-order rate constant for SO_4 removal (mg $L^{-1}d^{-1}$). The zero-order rate constant for CC pore-water data is -14 mg $L^{-1}d^{-1}$. The fit of this model was poor (R^2=0.092) and the zero-order rate constant calculated is not significantly different from zero (F-test; p=0.4640). The zero-order rate constant for the EVOI second sampling pore-water results was -53 mg $L^{-1}d^{-1}$ with a reasonable fit (R^2 = 0.93). There was no significant difference between these two calculated results for the first sampling event in CC and the second sampling event in EVOI (p = 0.0519).

A zero-order rate equation did not appropriately represent the sulfate removal rates for the first and third sampling event from EVOI and the EVOS columns first sampling event due to a varying rate of removal along the column length. These data were consistent with a first-order rate equation $C = C_0e^{-kt}$, where C is the pore-water SO_4 concentration (mg L^{-1}), C_0 is the initial SO_4 concentration (mg L^{-1}), t is the residence time (days), and k is the first-order rate constant (d^{-1}). The EVOS1 and EVOS2 datasets were adequately described by one curve (F test; p = 0.1050) with a reasonable model fit (R^2 = 0.98). The first-order rate constant for EVOS columns is k = -0.66 d^{-1}. In EVOI first and third sampling events, sulfate removal was not observed along the flow path until the third sampling port. A first-order rate equation was applied with an initial plateau with no removal. The first-order rate constant for EVOI first sampling event is k = -0.34 d^{-1} and the third sampling event is k = -1.98 d^{-1}. These two datasets are best described by separate curves (F test; P = 0.0002) with reasonable fits (R^2 > 0.98).

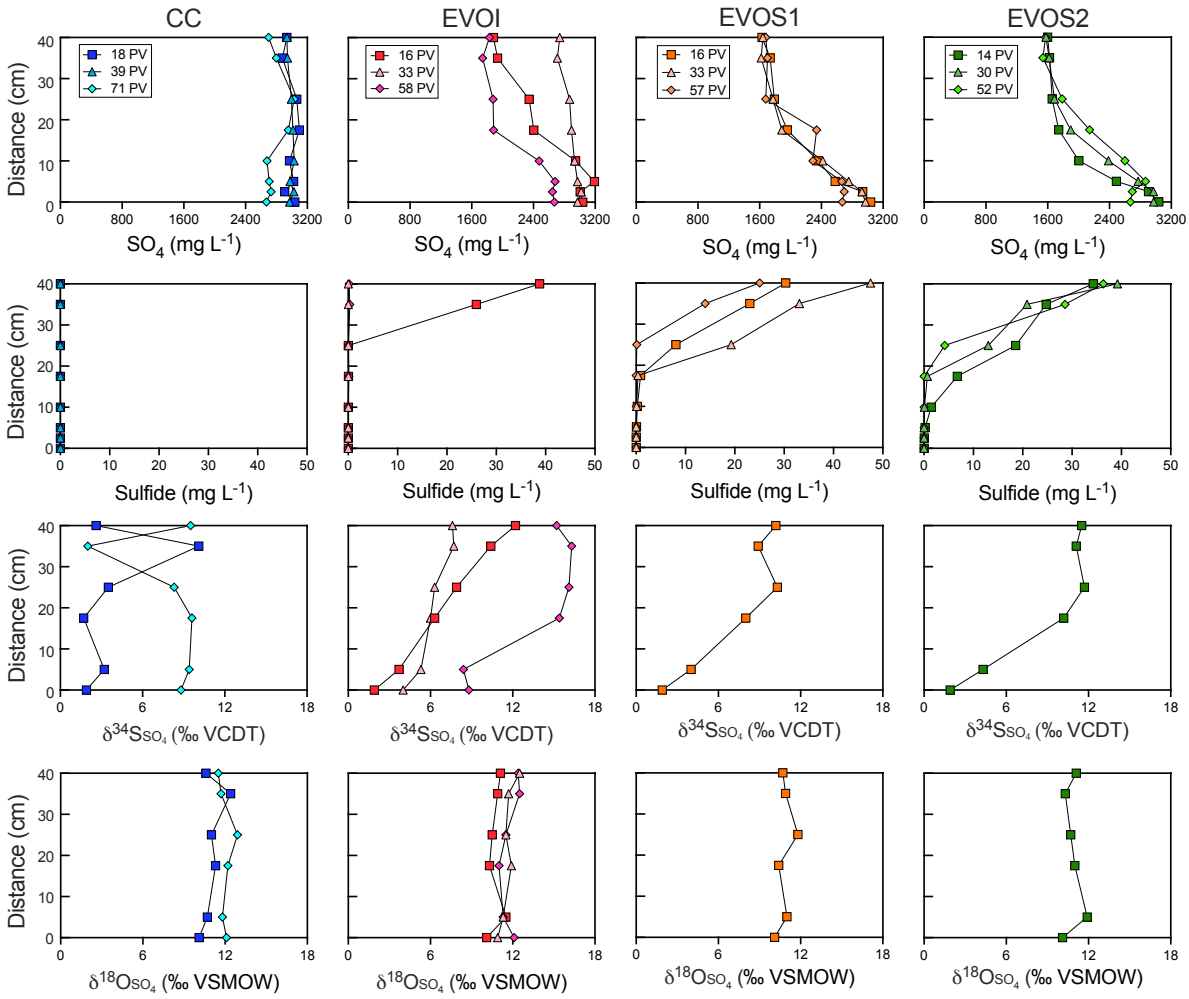


Figure 3.5. Pore-water SO_4, sulfide, and $\delta^{18}O_{SO_4}$ and $\delta^{34}S_{SO_4}$ measurements from pore-water SO_4. Samples were collected along the length of each column during three sampling events with each plot representing a different geochemical parameter for each column. The sampling events for each column, labeled according to the approximate PV during sampling, are differentiated by both color and shape. Distance 0 cm represents the influent and 40 cm represents the effluent.

3.3.2.4 Contaminant Treatment: Metal Attenuation and Acid Generation Mitigation

The mean influent Fe concentration was 708 ± 27 mg L^{-1} (**Figure 3.6**). The effluent of all four columns had little to no measurable Fe at the beginning of the experiment. The CC effluent Fe concentration increased sharply over the first 10 PV to 525 mg L^{-1} with measured concentrations approaching influent values for the duration of observation. All three profile pore-water sampling events of CC show little to no change in Fe concentration from the influent though the column (**Figure 3.7**). There was near complete removal of Fe in EVOI over the first 20 PV. Pore-water sampling during this period revealed Fe concentrations decreased throughout the column with variable rates of removal. After 20 PV the EVOI effluent Fe concentration increased to a maximum concentration prior to the second injection of EVO. Profile sampling of EVOI at 33 PV shows a modest linear decline in Fe concentration along the flow path. A rapid transient decline in Fe concentration was observed in EVOI effluent after the second EVO injection with a minimum measured concentration of 8 mg L^{-1} after 12 PV (52 PV total) and a subsequent increase in concentration to the end of observation. The Fe concentrations in the final profile sampling event at 58 PV decreased in a similar manner to the first event with a minimum measured concentration of 25 mg L^{-1} in the last sampling port (35 cm). Little to no Fe was measured in EVOS1 and EVOS2 effluent for the entire experimental period expect for a brief initial breakthrough event at ~5 PV in both columns. All three pore-water profiles in the EVOS columns had a similar pattern of Fe concentration with near complete removal occurring in the first 30 cm of the columns.

Potential acidity was calculated by subtracting the acid buffering capacity in molar equivalents of total alkalinity from the acid producing potential as a result of dissolved Fe(II) oxidation. The low alkalinity and high Fe concentration results in a net-acid potential for the influent solution (25 ± 1; mean ± standard deviation). Initially, the effluent of all columns was net-acid consuming (**Figure 3.6**). After the first 10 PV, the effluent of CC became net-acid producing for the duration of observation. Corresponding to the increase in Fe concentration, the effluent of EVOI became net-acid producing at 20 PV. The effluent became net-acid consuming again after the second EVO injection at 46 PV and remained acid consuming for the remaining experimental period. The effluent of EVOS columns remained net-acid consuming except for EVOS2 during the breakthrough of Fe in the effluent at 5 PV.

Influent Ni concentrations were stable with mean of 4,870± 390 μg L^{-1} (**Figure 3.6**). All four columns had little to no measurable Ni in the effluent. Pore-water profiles show a sharp decrease in

Ni concentration in all four columns with near complete removal occurring by 10 cm in every column (**Figure 3.7**).

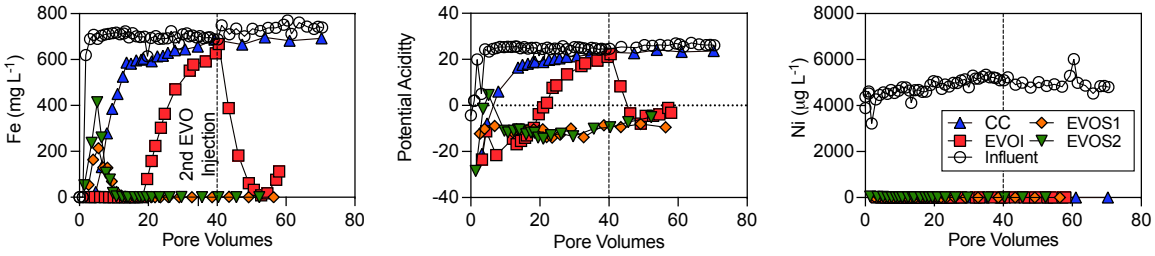


Figure 3.6. Influent water and column effluent Fe, potential acidity, and Ni. A positive potential acidity would indicate a net-acid potential with surface discharge while negative values indicate net-acid consuming potential. Each plot is a measured or calculated parameter with influent and effluents from each column differentiated by shape and color.

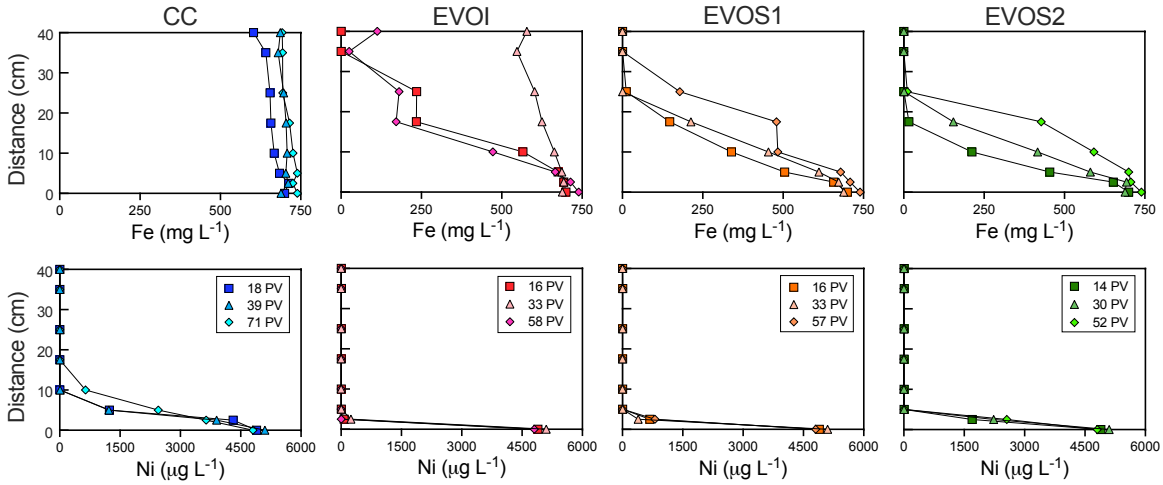


Figure 3.7. Pore-water Fe and Ni concentrations collected along the length of each column during three sampling events with each plot representing a different geochemical parameter and column. The sampling events for each column, labeled according to the approximate PV during sampling, are differentiated by both color shade and shape. Distance 0 cm represents the influent and 40 cm represents the effluent.

3.3.3 Column Microbiology Characterization and Comparison

The microbial community in each sample is similar at the phylum level (**Figure 3.8**). Firmicutes is the most abundant (mean relative abundance 54.9% of total reads) followed by Proteobacteria (17.4%), Actinobacteria (6.8%) and Bacteroidetes (3.6%). The mean relative abundance of unclassified bacteria on the phylum level accounted for 7.7% of total amplicons. The most abundant prokaryotic groups could not be identified at the genus level with minor genera grouped together accounting for 41.9% of total reads. Higher taxa that could not be identified at the genus level but were prominent in the samples include: Bacillales 12.44% total reads), Bacteria (7.73%), Firmicutes (5.12%), Clostridiales (4.11%), and Ruminococcaceae (3.49%). The most abundant bacteria that could be identified at the genus level were SRB *Desulfosporosinus* (1.9%) and *Desulfurispora* (0.9%).

Bacteria and archaeal communities (BACs), on the genus level, were compared using unweighted and weighted UniFrac with observable differences between test conditions (**Figure 3.8**). The addition of EVO through soaking and injection greatly affected the column BACs. Highly significant differences (AMOVA, $p < 0.001$) in β-diversities were observed when comparing samples from different test conditions: CC *vs.* EVOI, CC *vs.* EVOS columns, and EVOI *vs.* EVOS columns. When comparing EVOS columns (EVOS1 *vs*. EVOS2), there were insignificant differences based on weighted UniFrac (AMOVA, $P < 0.05$) and significant differences using unweighted UniFrac (AMOVA, $P < 0.05$).

The distribution and make up of SRB populations within each column varied spatially and between treatment conditions (**Figure 3.9**). The mean relative abundance of SRB in CC, EVOI, EVOS1, and EVOS2 were 4.4% ± 0.6% (mean ± standard deviation), 5.5% ± 1.9%, 3.1% ± 1.8%, 4.0% ± 2.9% respectively with an insignificant difference (t-test, $P > 0.05$) between mean relative abundances in each test condition. At a genus level, the most abundant SRB varied between each test condition (**Table B6**). In CC the most abundant genus were *Desulfurispora* (0.99 %*)* followed by *Desulfovibrionales* (0.84%)*, Desulfotomaculum* (0.53%) with *Desulfosporosinus* accounting for 0.4% of total reads. In EVOI and EVOS columns the most abundant genus was *Desulfosporosinus* making up 1.39% (of total reads) and 2.40% respectively. Other prominent groups in EVOI include *Desulfurispora* (1.21%) and *Desulfovibrionales* (0.88%). In EVOS columns *Desulfovibrionales* (0.37%) and Desulfitibacter (0.26%) were also abundant.

Iron and S oxidizers were detected in low mean relative abundance with difference in relative abundance between each test condition determined to be insignificant (t-test, $P > 0.05$; **Figure 3.9**).

Alicyclobacillaceae and *Acidimicrobiia* were the most abundant Fe and S oxidizers in each column of the genus detected. Methanogens and methylogens were also detected in all columns at low relative abundances (**Figure 3.9**). The mean sample abundance of methanogens in CC samples (0.8 ± 0.2 %) was significantly higher (t-test; $P < 0.05$) than in EVO columns (EVOI, EVOS1, and EVOS2) while the mean abundance in EVOS column samples was significantly lower than CC and EVOI samples.

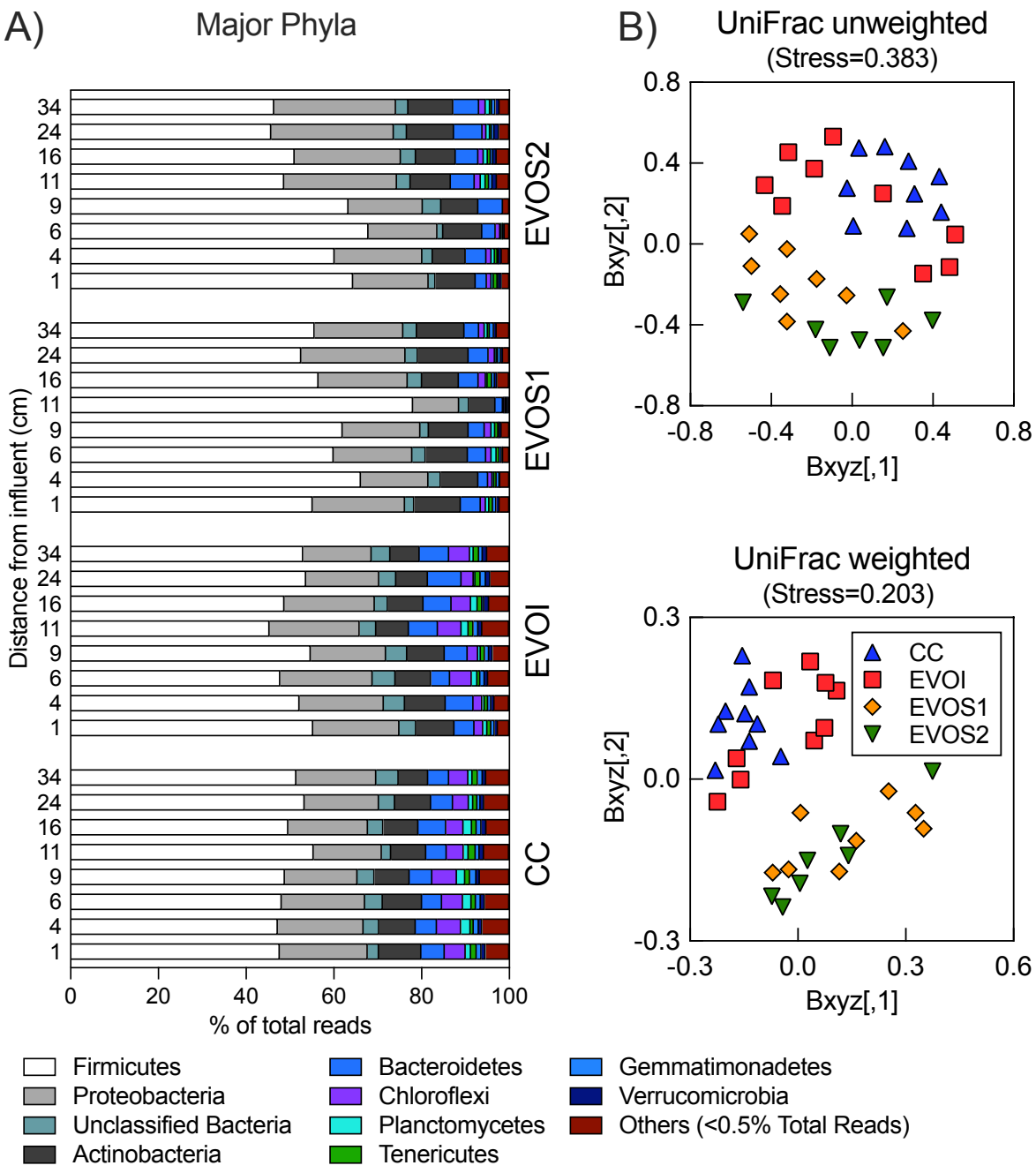


Figure 3.8. A) Major phyla proportion of total reads (relative abundance >0.5 % of total reads) of samples collected at week 12. B) 2-dimensional non-metric multidimensional scaling (2D-NMDS) plots based on unweighted UniFrac and weighted UniFrac. In these plots the distance between any two points represents the difference between the two communities.

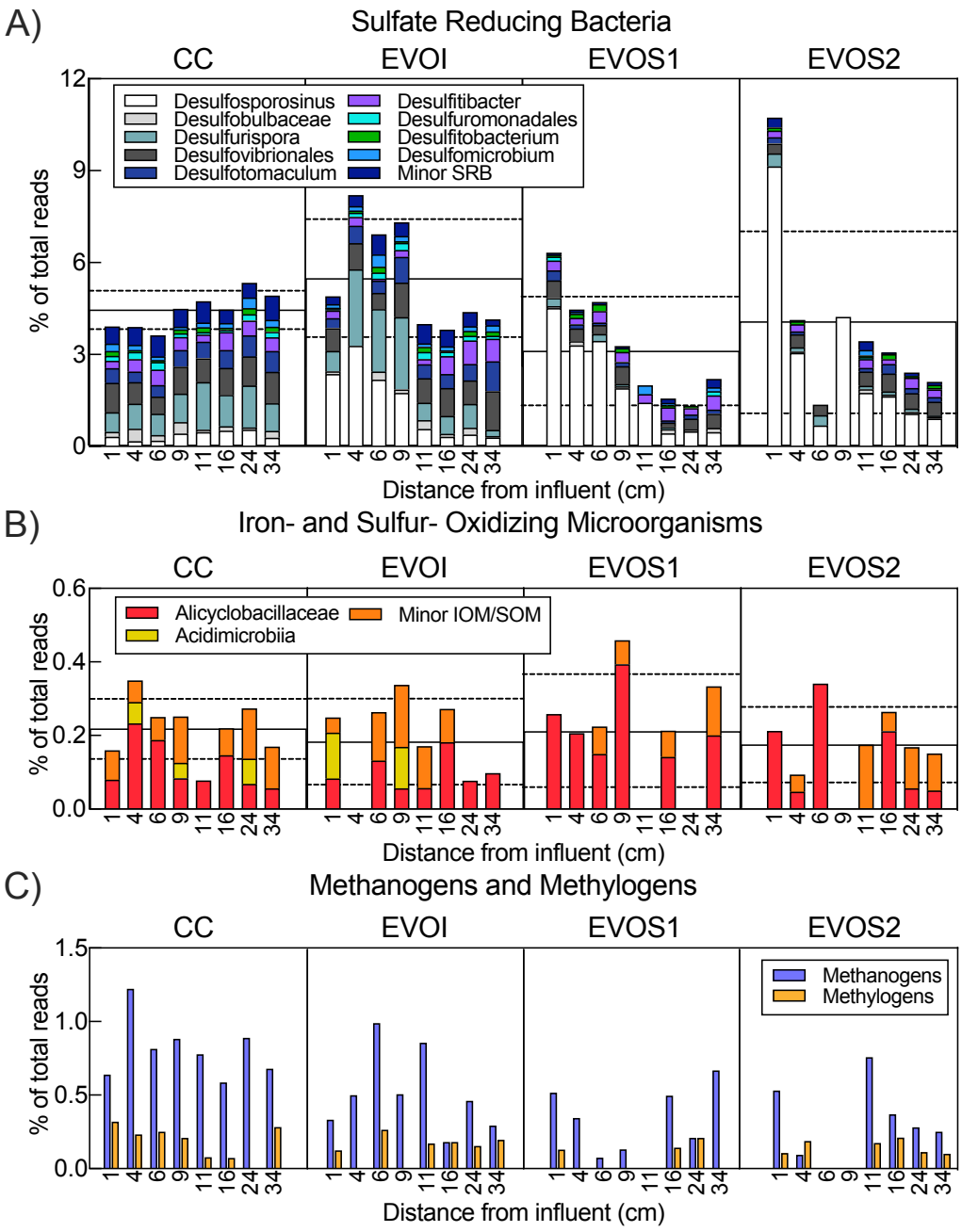


Figure 3.9. A) Proportion of total reads of sulfate reducing bacteria (SRB) at the genus level. An asterisks indicates when genus level identification was not possible and merged higher taxa are used. Minor SRB < 0.5 % of total reads. B) Proportion of total reads of iron-(IOM)/ sulfur-(SOM) oxidizing microorganisms at the genus level. Minor IOM/SOM < 0.05 % of total reads. A solid black line represents the mean relative abundance of IOM/SOM in each column with 1 standard deviation from the mean indicated by dashed lines in A and B. C) Proportion of total reads of methanogens and methylogens at the genus level. Samples were collected at week 12.

3.3.4 Solid-Phase Characterization

3.3.4.1 Solid-Phase Characterization

Moisture content was consistent along the column length and between columns (**Table B7**). Duplicate samples had an average moisture content relative percent difference of 4.3% and maximum of 10.2%. Total inorganic carbon content was low (0.3 ± 0.1 wt. %; mean ± standard deviation) in all samples with little variation between columns or along the column length (**Figure 3.10**). Total C content is greater in columns with EVO. Total C in CC was consistent with the mean (2.6 ± 0.3 wt. %) throughout the column length. In EVOI, the highest concentrations, up to 3.7 wt. %, were observed in the lower half of the column. In EVOI, the lowest sample (1.5 cm) and upper half of the column (>20 cm) had similar concentrations of total C to CC. Total C increases along the column length in EVOS1 from 2.6 wt. % to a maximum of 5.0 wt. % while concentrations were more consistent around a mean 3.78 ± 0.38 wt. % through the length of EVOS2.

3.3.4.2 Sulfur Selective Extractions

Sulfide minerals are divided into two operationally-defined groups: AVS composed of dissolved sulfide species, monosulfides, amorphous Fe sulfides, mackinawite and greigite, and TRS which encompasses the AVS fraction in addition to disulfides, such as pyrite, and elemental sulfur (Rickard & Morse, 2005). The concentration of total S, TRS, and AVS are generally consistent in each sampling point (**Figure 3.10**). Due to the similarity in these measurements the results of AVS extraction will only be described. The measured AVS in CC samples are consistent with a mean of 60.0 ± 29.5 μmol g^{-1} along the column length. In EVO columns, AVS was elevated in the lower portion reaching maximums of 596 μmol g^{-1}, 988 μmol g^{-1}, 734 μmol g^{-1} for EVOI, EVOS1 and EVOS2 respectively. In EVO columns AVS progressively decreases along the flow path after reaching the maximum. Large uncertainty in some measurements results in many samples breaking from the expected concentration hierarchy of total S > TRS > AVS. There may be appreciable accumulation solid phase S forms other than AVS below 5 cm in EVOS columns based on extraction results.

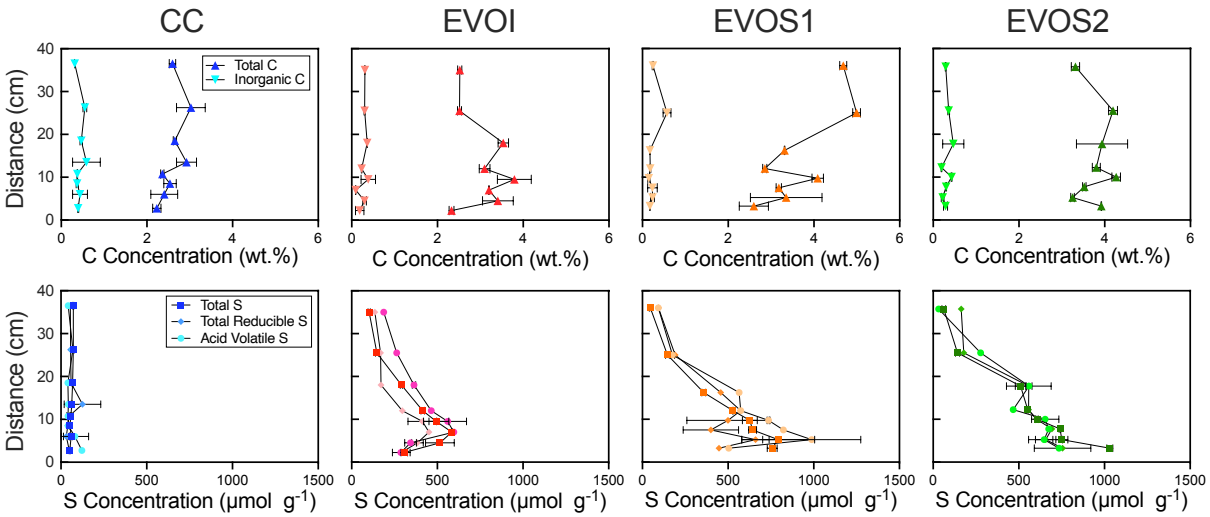


Figure 3.10. Solid phase analyses of C and S from samples taken at the end of the experiment. Each analysis is differentiated by shape with the color used to differentiate columns and aid in comparison to water chemistry data. The mean concentrations are plotted when measured in replicate with error bars representing 1 standard deviation from the mean to provide an estimate of sample heterogeneity and analytical error.

3.3.4.3 Sulfur K-Edge XANES

S K-edge XANES linear combination fitting results suggest FeS is one of the primary reduced S phases in every column (**Table B3**). A prominent peak at 2,482 eV, attributed to ferrous sulfate, gypsum and other sulfate species, is observed in every sample except EVOS1-4 cm (**Figure 3.11**). Some pyrite may have formed in all columns as suggested by the best LCF fitting. The LCF goodness of fit with pyrite provide only marginal improvement compared to fits without pyrite (**Table B8**). There appears to be a notable accumulation of organic S species in both CC and columns with EVO. Intermediate S species also appear to be present in modest abundances in the columns with EVO while not readily observed in the CC column samples (**Table B3**). The most noteworthy intermediate S phase is thiosulfate in the 4 cm samples from EVOS columns based on the peak at 2,472.1 eV. Comparing the raw S XANES spectra counts between samples, the counts from CC samples at 4 cm and 24 cm are notably lower than the samples from EVO columns except for the EVOS2 24 cm sample (**Figure B6**).

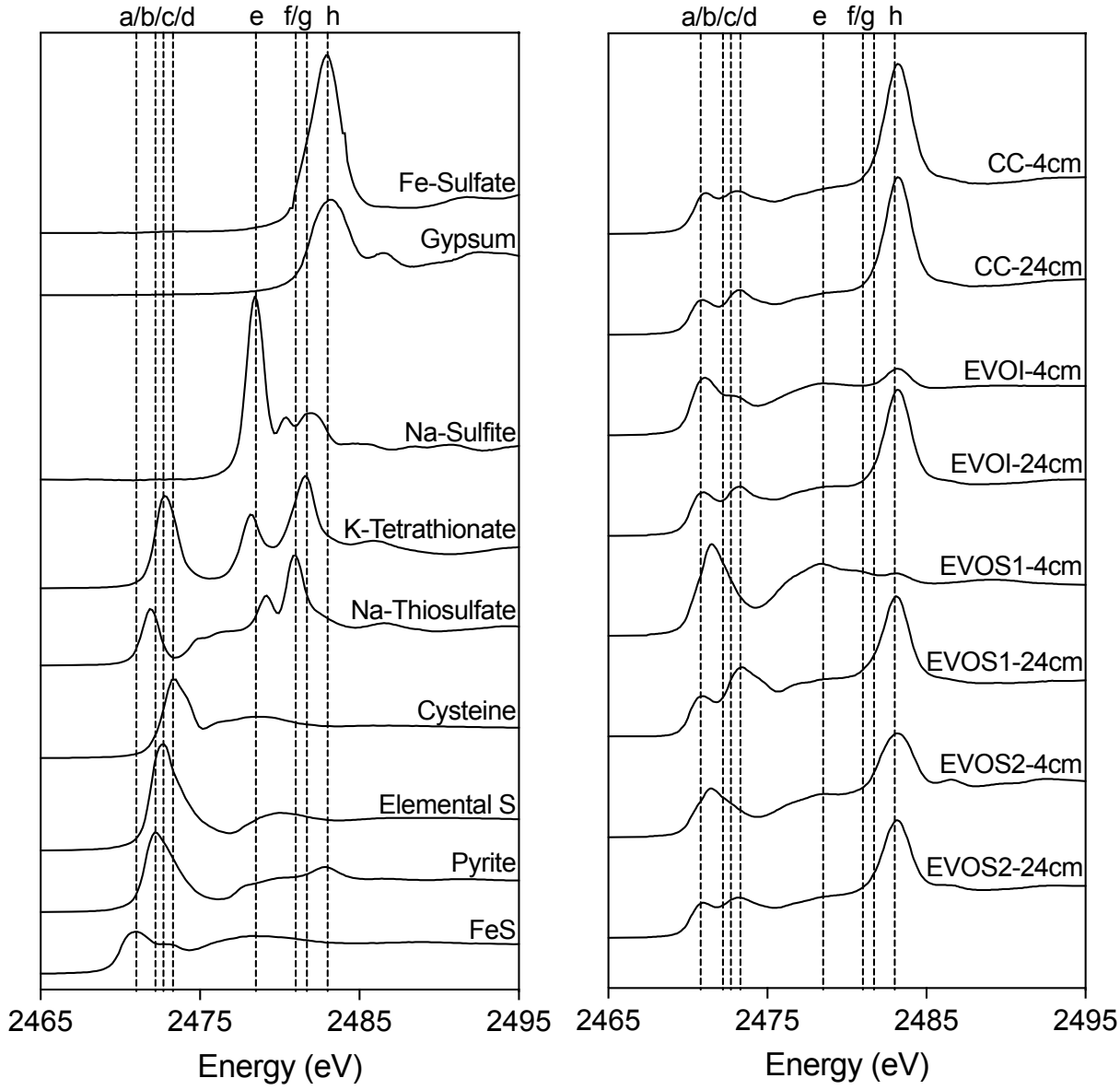


Figure 3.11. Measured Bulk S K-edge X-ray adsorption near edge structure (XANES) of solid material collected after 12 weeks of treatment. Standards on the left were used in linear combination fitting. The max peak (whiteline position) is illustrated as a dashed line for FeS (a), pyrite (b), elemental S (c), cysteine (d), Na-sulfite (e), Na-thiosulfate (f), K-tetrathionate (g), gypsum (h), and ferrous sulfate (h).

3.4 Discussion

3.4.1 Column Flow Conditions and EVO Mobility

Amendments that do not have adverse impacts on flow conditions of a PRB are important for effective treatment as internal pore clogging causing groundwater flow bypass are common mechanisms of failed PRBs (Gibert et al., 2011; Henderson & Demond, 2007) requiring reactive material replacement (ITRC, 2011). A modest reduction in PV was initially observed in the EVOS columns when measured gravimetrically after saturation. This reduction in PV appears to be transient because the modeled results from the tracer tests conducted within the first 10 PV of treatment flow suggest the PV of the EVOS columns was greater than CC– a reversal from the gravimetric measurements. This may suggest breakdown and/or flushing of the EVO out of the column occurred early in the experiment. Elevated total C concentrations measured at the end of the experiment and the overall treatment performance of the EVOS columns are indicators of high levels of EVO retention. A more likely possibility is that packing the EVOS columns wet, with EVO acting as a binder, led to less settling of fine-grained material and a greater porosity once flow began.

The EVOI CXTFIT result also indicate a greater PV than the gravimetric result, suggesting there was no reduction in porosity observed after the initial injection of EVO. Previous studies of EVO injection, retention and transport dynamics primarily occurred in sand and clay aquifer material (Borden, 2007; Coulibaly & Borden, 2004; Muller et al., 2018). The retention of oil is expected to result in modest to moderate losses in permeability (Coulibaly & Borden, 2004) with the greater initial emulsion concentrations resulting in more oil retained in the sediment (Muller et al., 2018). Injection into solid phase OC may allow for oil retention in the matrix pore system without clogging the macropore space associated with primary water flow. The consistency of discharge results before and after the second EVO injection in EVOI suggests no apparent adverse effects from EVO, the EVO degradation products, biofouling, or precipitation reactions with subsequent EVO injections.

The migration of EVO beyond the initial PRB boundaries in a field environment would result in a more expansive treatment zone and extend the hydraulic residence times with the net effect of enhancing the overall treatment performance. Because of the column configuration, these effects are not apparent in analyzing the geochemical results of the experiments. The preferential migration of EVO in EVOI following the first injection is attributed to the lower density of EVO compared to water, resulting in a buoyancy effect and faster movement of EVO in a vertical column. Buoyancy effects have been observed at a field site (Tang et al., 2013) and should be accounted for during EVO

additions at the field scale through injection well placement. In addition, colloidal migration of EVO due to size exclusion may have also contributed to preferential migration (Tang et al., 2013; Watson et al., 2013). The lack of visible migration during and after the second EVO injection suggests that the secondary precipitates have a higher affinity for retaining EVO. The physical characteristics of the EVO (*e.g.*, droplet size) may have also changed over time (Coulibaly & Borden, 2004) affecting the flow characteristics.

3.4.2 Geochemical Conditions

The geochemistry and microbial community composition are both affected by the incorporation of EVO through soaking and injection. At the onset of treatment, the effluents of all four columns were reducing with an abundance of DOC and volatile organic acids present. Exhaustion and initial flushing of the labile OC within the solid phase OC mixture in CC is attributed to the rapid decline in DOC concentration and shift to less reducing conditions (Angai et al., 2022; Lindsay et al., 2011). Continued treatment in CC was likely limited by enzymatic degradation and hydrolysis of the more complex lignocellulose compounds (Drennan et al., 2017; Logan et al., 2005). Breakdown of EVO is expected to occur rapidly resulting in glycerol that is quickly utilized, and long chain fatty acids (LCFA) that support long-term bioremediation (Gihring et al., 2011). The amendment of EVO may do more than simply provide an OC source that sustains reducing conditions. A priming effect has been observed, in natural soils, where amendments of labile OC can increase the mineralization rate of recalcitrant OC (Guenet et al., 2010). The incorporation of EVO into lignocellulose-based OC may provide a similar priming effect and a more efficient long-lasting system than obtained from using EVO and solid phase OC independently. Regardless of the presence or absence of a priming effect, the sustained decrease in Eh and higher DOC concentrations in the effluent of EVO columns are attributed to the EVO amendments.

Comparing the results of EVOI to EVOS may suggest that soaking OC in EVO sustains reducing conditions for longer. However, the effects of different amounts of EVO in the initial amendments between injection and soaking are confounding. Soaking ensures consistent distribution of EVO with less EVO migration. In a field PRB installation, the presence of DOC and volatile organic acids in the effluent are likely to promote reducing conditions in the downgradient aquifer material, similar to the migration of EVO. The presence of DOC or volatile organic acid derived from EVO will also increase the treatment hydraulic residence time and further improve treatment performance.

The incorporation of EVO may influence pore-water pH and mineral stability. In the EVOS columns, the decreased effluent pH observed at the beginning of the experiment and the decreased pH in the lower portion of the columns during the first pore-water sampling event is attributed to the release of LCFA (Gonsalez et al., 2023). Over time, as the supply of LCFA declined, these effects decreased and the pH approached circumneutral conditions in EVOS columns pore-water and effluent. This transition likely occurred in EVOI after both EVO injections to a lesser extent due to lower concentrations of EVO retained, which limited the observable effect on pH.

The pH in all four columns was regulated by the dissolution of $CaCO_3$ present in the initial limestone amendments. Calculated saturation indices suggest the pore-water was undersaturated with respect to calcite in all EVO columns at the beginning of the experiment (**Figure B7**). Elevated concentrations of Ca in the effluent in all columns suggest dissolution of the limestone amendments occurred. In CC, limestone dissolution was likely limited to the lower portion of the column before reaching equilibrium and transitioning to saturation with respect to calcite due to bicarbonate production from anaerobic OC oxidation. Sustained limestone dissolution in EVOI and EVOS, due to a decrease in pH, may have occurred based on the increase in Ca observed in both the pore-water and effluent compared to the influent. Alternatively, limestone dissolution rates may have been greater in EVO columns at the onset of the experiment. The resulting elevated Ca concentrations in combination with availability of LCFA may have promoted the formation of secondary Ca-LCFA complexes (Tang et al., 2013). As secondary Ca-LCFA complexes degrade over time, the Ca would be re-released increasing the effluent Ca concentration with little to no limestone dissolution required.

Calcium effluent concentrations from CC and EVOI approach influent concentrations at 20 PV and 32 PV respectively. Geochemical calculations suggest CC and EVOI effluent remained undersaturated with respect to calcite and no clear change in influent or effluent pH was observed. The elevated concentrations of inorganic C in both CC and EVOI observed in the solid phase analysis from samples taken at the end of the experiment suggest an accumulation of either primary or secondary carbonates. The initial high concentrations of Ca in addition to the SO_4 concentrations resulted in conditions favorable to gypsum precipitation which may have passivated the initial limestone amendments limiting further dissolution. Simulation results of similar column experiments suggest siderite precipitation results in undersaturated conditions with respect to calcite and continued calcite dissolution until all the initial limestone amendments are exhausted (Amos et al., 2004). Based on effluent results, siderite is favored to precipitate in CC and EVOI after ~5 PV and ~20 PV

respectively (**Figure B7**). However, the increase in EVOI effluent Ca concentrations following the second injection of EVO may suggest the initial amendment of calcite was not exhausted.

The products from the microbial degradation and utilization of EVO also regulate pore-water pH. For example, the products of DSR by *Desulfosporosinus*, the most abundant SRB in the EVO columns, are bicarbonate and acetate (Rabus et al., 2013). Both bicarbonate and the conjugate base forms of volatile organic acids increase the alkalinity and pH buffering capacity of the pore-water and effluent. The initial abundance of labile OC in all columns and the extent of degradation early in the experiment resulted in the maximum accumulations of both alkalinity and volatile organic acids. The degradation of EVO in the EVOS likely resulted in sustained production of bicarbonate and acetate over the duration of the experiment. The sustained elevated alkalinity in EVOI compared to CC is attributed to the EVO injection. The second EVO injection in EVOI appears to provoke a less pronounced microbial response compared to the first injection, resulting in a lower magnitude increase in alkalinity. The delay in the increase in Ca concentrations after the second injection may suggest calcite dissolution was not a major contributor to this second peak in alkalinity.

The differences in the microbial communities observed within the column experiments following the first pore-water sampling event reflect the microbial response to EVO amendments. The EVO amendments affected the BAC resulting in highly significant differences in β-diversities between every test condition. Unweighted UniFrac suggests differences in the microbial community make-up between EVOS1 and EVOS2; when abundance is taken into account using weighted UniFrac, the communites are similar. Additions of EVO likely resulted in competitive exclusion that favored microorganisms capable of utilizing the EVO degradation products (Deng et al., 2016). Amendments of EVO have been shown to reduce species richness following injections (Gihring et al., 2011; P. Zhang et al., 2017). Based on the Gini-Simpson's index results, there does not appear to be any reduction in species richness in the EVOI column or EVOS columns compared to CC at the time of sampling. In contrast, lignocellulose-based SRBRs often have a highly diverse microbial community compared to systems with a single carbon source due to degradation of more complex forms of OC (Hiibel et al., 2011). At the broad phylum level, there is a high level of similarity between each column and to results reported in previous studies of lignocellulose-based SRBRs treating mine impacted groundwater with high abundances of Firmicutes, Proteobacteria and Bacteroidetes (Aoyagi et al., 2017; Baldwin et al., 2015; Drennan et al., 2017). Species within *Clostridium* and *Ruminococcaceae* are often found within SRBRs and are inferred to contribute to OC degradation and fermentation (Baldwin et al., 2015; Drennan et al., 2016).

Methanogens co-occur with, and in some instances outcompete SRB in SRBRs (Rezadehbashi & Baldwin, 2018). A decrease in the abundance of methanogens was observed in EVO columns compared to the CC column. The proliferation of acetate-consuming methanogens is thought to be beneficial in promoting DSR due to acetic acid inhibition of SRB (Rezadehbashi & Baldwin, 2018). The differences in effluent acetate concentrations from the EVOS *vs*. EVOI column likely reflect differences in the overall microbial community structure rather than the rapid utilization of all the EVO retained in EVOI. Methanogens may play a role in regulating acetate accumulation in CC and EVOI but the importance of methanogenesis in supporting DSR is not clear. Methanogens are inhibited by sulfide (Karhadkar et al., 1987), which may limit the benefit of methanogens in systems with high rates of DSR or limited Fe. The pore-water sulfide may have inhibited methanogens in the EVOS columns. In treatment systems with lower pH, acetic acid, the conjugate acid of acetate, plays a larger role in inhibiting SRB growth (Reis et al., 1990) and methanogens consuming acetate may have greater importance in enhancing treatment.

Temporal shifts in the microbial communities may have occurred following EVO amendments (Gihring et al., 2011; P. Zhang et al., 2017). Inferences into the temporal changes in microbial community structure in each column are limited by the single DNA sampling event. The timing of DNA sampling has important implications for these results because the EVOI effluent showed Fe breakthrough shortly after DNA sampling that is attributed to the exhaustion of the EVO amendment. The results of weighted and unweighted UniFrac would suggest there is greater similarity betweeen CC and EVOI than with EVOS, based on sample clustering. Temporal differences in the microbial community in each column may have resulted in the rapid decline in volatile organic acid concentrations as microbes capable of filling the niche proliferated. The rapid decline in propionate and formate concentration in the effluent of every column early in the experiment suggests a rapid increase in microbial activity.

3.4.3 Sulfur Biogeochemistry

Amendments of EVO stimulated shifts in the SRB community structure. High levels of SO_4 removal and presence of sulfide at the onset of treatment indicates DSR was occurring at a rapid rate in every column. The SRB communities are dynamic and changes to the dominant SRB species are expected with shifts in the availability of OC substrates from both the breakdown of EVO and the degradation of solid-phase OC sources (P. Zhang et al., 2017). At the time of DNA sampling, bulk SO_4 removal rates were distinctly different among the columns. As with previous column studies (Drennan et al.,

2016), there does not appear to be a correlation between the rate of SO_4 reduction and the abundance of SRB because the difference in the mean SRB abundance between test conditions was insignificant. In lignocellulose-based SRBRs the relative abundance of SRB is typically low due to the broad array of functional groups required for OC mineralization (Baldwin et al., 2015; Hiibel et al., 2011; Schmidtova & Baldwin, 2011).

In both EVOS and EVOI there is a clear proliferation of *Desulfosporosinus* which can utilize a variety of OC electron donors and grow chemolithotrophically using H_2 (Pester et al., 2012). In SRBRs treating AMD, *Desulfosporosinus* is often the dominant SRB despite differences in geographic location, treatment conditions and operating configuration (Habe et al., 2020). *Desulfosporosinus* are resilient spore-forming SRB capable of surviving in dry and oxic conditions for extended periods and have previously been identified in oxidized layers of gold mine tailings (Mardanov et al., 2016) along with other AMD environments characterized by low-pH and high metal concentrations (Sánchez-Andrea et al., 2011, 2014). The presence of *Desulfosporosinus* in AMD environments and SRBRs suggests a similar microbial response could be established in field applications of EVO without the need for microbial inoculation. In contrast to a previous microbial study of an EVO injection site (P. Zhang et al., 2017), the species richness of the SRB community appears to decrease in columns with EVO, particularly in EVOS. The discrepancies between these observations are likely due to EVO being amended into a mixture of OC sources that already sustain a great variety of SRB, as observed in CC, rather than aquifer material with a lower OC content.

Assuming the breakdown of EVO is similar in the EVOI and EVOS columns due to the timing of injection, differences in the SRB community between the EVOI and EVOS column are attributed to differences in the amount of EVO retained within each column. At the time of measurement, the abundance of *Desulfurispora* and *Desulfovibrionales* in EVOI is higher than EVOS and similar to CC, probably due to a lower amount of EVO retained. *Desulfurispora* are a gram-positive spore forming SRB that can use a variety of OC substrates to reduce SO_4 and have been previously identified in sulfidogenic fluidized bed reactors treating AMD (Kaksonen et al., 2007). The order *Desulfovibrionales* contains *Desulfovibrio vulgaris* which have been shown to be inhibited by elevated metal concentrations including Ni (Cabrera et al., 2006). The rapid attenuation of Ni in the columns may prevent the inhibitory effects. *Desulfovibrio vulgaris* are also incompletely-oxidizing SRB producing acetate from the oxidation of various OC substrates (Rabus et al., 2013).

Fractionation in pore-water $\delta^{34}S_{SO_4}$ can be imparted by a variety of processes (Canfield & Thamdrup, 1994; Pellerin et al., 2019; Rees, 1973; Sim et al., 2011). Dissimilatory sulfate reduction

is the dominant process resulting in fractionation in sulfidogenic OC treatment systems (Druhan et al., 2012, 2013; Gibson et al., 2011; Guo & Blowes, 2009) . Through a multi-step reversal pathway ^{32}S is preferentially incorporated into sulfide resulting in a measurable fractionation factor (α) and more positive $\delta^{34}S_{SO_4}$. During the first sampling event, pore-water $\delta^{34}S_{SO_4}$ does not vary through CC which is attributed to the low rate of SO_4 removal and a large initial pool of SO_4. The increase in $\delta^{34}S_{SO_4}$in EVO columns is attributed to DSR. A Rayleigh model was fit to the CC and EVO columns $\delta^{34}S_{SO_4}$ pore-water data to calculate α and enrichment factors (ε; **Figure B13**; Guo & Blowes, 2009). The CC results poorly fit the model ($R^2 < 0.41$) which contrasts with previous solid phase OC column results (Guo & Blowes, 2009). The poor fit in first and second sampling event for EVOI may suggest a variable α from limited OC substrate in some zones of the column (**Table B9**). There was good agreement with the model and results for the third sampling event of EVOI and EVOS column data ($R^2 > 0.96$) with calculated ε of -18.1, -13.7, and -15.0 respectively. These ε are smaller in magnitude than what has been previously reported for column experiments with OC (Angai et al., 2022; Guo & Blowes, 2009; Waybrant et al., 2002). The smaller ε measured in EVO columns are likely a result of increased substrate availability and higher cell specific rates of SO_4 reduction (Leavitt et al., 2013; Sim et al., 2011) but other factors may also contribute (Giannetta et al., 2019).

During the first profile sampling event, SO_4 removal appears to occur in every column. In the ~6 PV prior to this sampling event, the influent SO_4 was consistent (3,057 ± 20 mg L^{-1}, mean ± standard deviation) which suggests that the variability and overall decrease in SO_4 observed in CC is a result of processes occurring within the column, including S cycling. The bulk removal rates in a field-based system decreased from an initial rate of 58 mmol L^{-1} a^{-1} (15.3 mg L^{-1} d^{-1}) to 40 mmol L^{-1} d^{-1} (10.5 mg L^{-1} d^{-1}) over the first 38 months of treatment (Benner et al., 2002). The rate observed in CC (14 mg $L^{-1}d^{-1}$) is similar to the initial rates observed in the field-based system. It is important to note the field-based system operates at a much lower average temperature that should decrease the overall rate of DSR (Benner et al., 2002). The reaction rate of CC is less than previous OC column experiments conducted (Angai et al., 2022; Waybrant et al., 2002). However, the dry wt. % of OC is less than half these experiments. Previous OC column experiment results are more consistent with the rate observed in EVOI during the second sampling event likely due to the exhaustion of the initial EVO amendment and a transition to degradation of more recalcitrant OC. In microcosm experiments, higher SO_4 removal rates occurred in experiments containing more OC (Lindsay et al., 2008). Results from column experiments would suggest SO_4 removal rates may not increase after a threshold mass of

solid phase OC is present in the system (Angai et al., 2022). Comparing the results from CC to previous studies would suggest improved long-term treatment performance may have been feasible with a larger proportion of OC.

The columns with EVO amendments exhibit varied rates of removal along the column length. During the first and third sampling events in the EVOI column, appreciable SO_4 removal did not occur until ~10 cm within the column which is attributed to the migration of EVO during injection and exhaustion of EVO retained in the lower section. Rates of SO_4 removal dramatically increase above 10 cm. In EVOS the highest rates of SO_4 removal occurred in the lower portion of the columns. The rates in the lower portion of EVOI (first and third sampling event), and in EVOS, are an order of magnitude greater than what has been observed in solid phase OC column experiments (Angai et al., 2022; Waybrant et al., 2002). These high rates are not sustained along the column length, which is unique to this reactive media.

Solid phase analyses suggest removal of SO_4 occurs primarily through the precipitation of metal sulfides, formation of elemental S, and formation of organic S species. The LCF fitting of S XANES spectra indicates the presence of tetrathionate, sulfite and thiosulfate in the EVO columns (in varying amounts) but no appreciable accumulations in CC. These variations may be due to different microbial sulfur-cycling pathways or simply due to the higher rates of reaction allowing for greater accumulations of intermediate species. In marine environments, the formation of organic S species and sulfurization has been identified as a mechanism that limits the degradation of OC (Raven et al., 2021). In a PRB treatment system this process may limit OC reactivity and long-term treatment performance. The presence of gypsum and ferrous sulfate species in solid phase analysis is primarily attributed to the freeze-drying process and changes in the saturation state with dehydration because geochemical modeling of the influent and pore water suggests undersaturation of these species for a majority of the experiment. Ebullition of sulfide gas may be an additional mechanism of H_2S removal in sulfate reducing PRBs experiencing higher rates of SO_4 reduction (Williams et al., 2007), however no observations of gas release were made during these column experiments.

Spatially, the changes in bulk SO_4 removal rate along the column profile may be indicative of two different processes; S cycling or changes to the rate of DSR. Sulfur cycling is a common phenomena in natural environments and the paired use of $\delta^{34}S$ and $\delta^{18}O$ from pore-water SO_4 is often used to identify these effects (Antler et al., 2013; Gomes & Johnston, 2017; Mills et al., 2016). The consistency of $\delta^{18}O_{SO_4}$ is not indicative of S cycling occurring in the upper portion of columns with EVO (**Figure B13**). The availability of SO_4 also limits the rate of DSR (Boudeau & Westrich, 1984),

however the SO_4 concentrations in the EVOS effluent should not be limiting to the degree observed. Inhibition of DSR can also occur from the production of sulfide and acetate with acetate causing inhibition at lower concentrations than sulfide (Reis et al., 1990, 1992). Bulk SO_4 removal does appear to decrease as sulfide concentrations begin to increase after all the Fe is removed from the pore-water. Acetate does not accumulate in appreciable concentrations in EVOI, where a decrease in SO_4 removal rate is observed, suggesting acetate inhibition did not occur. The inhibition of DSR from these products is sensitive to both the concentration and the pH because DSR is primarily affected by the abundance of hydrogen sulfide species and acetic acid (Reis et al., 1992). Concentrations of both sulfide and acetate are below threshold values observed to influence some species of SRB directly (Reis et al., 1992). Another study proposed the precipitation of Fe-sulfide species can inhibit DSR (Utgikar et al., 2002). This limitation does not appear to limit DSR in the columns in this experiment; the greatest accumulation of AVS species also occurs in the lower portion of the EVO columns where SO_4 bulk removal rates are highest.

A decrease in the rate of SO_4 reduction along the column length is attributed to a limitation of the availability of a suitable OC source for DSR. Because material was homogenized in the EVOS it is unlikely that exhaustion of OC would be limited to the upper portion of the column prior to the lower zone, where rates of SO_4 reduction are higher. It is more likely that sulfide production in excess of Fe is impacting the rate of DSR, with aqueous sulfide impacting the microbial functional groups responsible for OC degradation. Aqueous sulfide may be acting as a negative feedback mechanism which slows microbial degradation of the OC and potentially prolongs treatment performance. A less desirable mechanism is that pore-water sulfide is resulting in OC sulfurization (Damste & De Leeuw, 1989; Raven et al., 2021). The greater diversity of organic S species in the upper portions of EVO columns may indicate the occurrence of this mechanism. If this is the case, a portion of the OC may become inaccessible for microbial degradation and DSR, which may impact the long-term treatment system performance. Beyond impacting acid mine drainage treatment, OC sulfurization may also limit the utility of complex OC material for managing low-metal and high SO_4 drainage where metal sulfide precipitation does not regulate aqueous sulfide concentrations. Further investigation into OC sulfurization leading to decreased SO_4 removal and the long-term effects on treatment performance of a biologically mediated AMD treatment system is needed.

3.4.4 Metal Removal Mechanism

The dominant mechanism of Fe removal in all columns is the precipitation of insoluble Fe-sulfides. Geochemical modeling suggests these phases were not favored to precipitate in all columns for the duration of the experiment. The modeling results juxtapose the observed solid phase results with this discrepancy attributed to the rapid kinetics of Fe-sulfide mineral precipitation. Iron-sulfide precipitation rapidly removes sulfide from the pore-water, resulting in dissolved H_2S concentrations that are below detection and limit the veracity of geochemical modeling results. Geochemical modeling may be a good indicator of the tendency for FeS formation but model results do not verify that mineral precipitation is occurring, or provide information on reaction rates.

Geochemical extractions, and S K-Edge XANES measurements both indicate that the most abundant reduced S phase is FeS. All four columns had FeS accumulation with EVO columns exhibiting higher concentrations of FeS, as a result of sustained high rates of DSR in the lower portions of the column as indicated by AVS accumulations and the S XANES raw counts. Precipitation of FeS, as a Fe mechanism of immobilization, is consistent with mechanisms observed in previous column experiments (Angai et al., 2022; Waybrant et al., 2002) and in field scale PRB installations (Herbert et al., 2000; Jambor et al., 2005). There does not appear to be a clear difference in the principal Fe removal pathways in CC *vs.* EVO columns. The S XANES spectra, includes indications of the occurrence of pyrite in the column material, however these results are not conclusive. The precipitation of amorphous FeS and mackinawite are considered precursors to pyrite formation with several different pyrite formation pathways possible (Guo & Blowes, 2009; Jambor et al., 2005).

Dissolved Ni removal occurred rapidly in the basal portion of each column. Slightly slower removal rates occurred in CC than the EVO columns. There are multiple mechanisms that can act to remove Ni in these systems. Experimental results have shown that Ni can be adsorbed onto soil organic matter (Shi et al., 2012) and may be a primary mechanism of removal given the rapid removal in all columns and abundance of organic matter. The addition of sulfide to solutions containing both Fe(II) and Ni(II) has been shown to precipitate mackinawite with Ni incorporated (Swanner et al., 2019), and may be another primary mechanism of Ni attenuation in these column experiments. Slower rates of FeS precipitation can result in higher amounts of Ni uptake per gram of FeS (Morse & Arakaki, 1993; Swanner et al., 2019). Rapid sorption on to the surface of mackinawite is expected to occur when Ni is exposed to mackinawite, if sorption sites are available (Wilkin & Beak, 2017). Interstitial substitution for Fe can occur over longer periods (Wilkin & Beak, 2017). It is unclear

whether Ni is being co-precipitated in the amorphous FeS that precedes the formation of mackinawite or if these sorption processes occur after mackinawite formation. The mechanisms of Ni attenuation may differ between the CC and EVO columns due to differences in the rate of FeS accumulation during the later stages of the experiment. Slower rates of DSR and FeS precipitations in CC over the course of the experiment may result in a maximum amount of sorption on mackinawite present within column followed by a transition to incorporating Ni removal through substitution.

Other potential mechanisms of Ni attenuation include the precipitation of poorly crystalline polyphasic NiS, $NiCO_3$, native Ni and Fe-bearing Ni sulfate and the incorporation of Ni into calcite and siderite. Nickel sulfide is not expected to be miscible with FeS phases (Wilkin & Beak, 2017; Wilkin & Rogers, 2010). This mechanism of attenuation is less favored than Ni incorporation into FeS phases based on the results of previous studies (Morse & Arakaki, 1993; Swanner et al., 2019). While $NiCO_3$ is not favored to precipitate based on geochemical modeling, Ni can be incorporated into both calcite (Parigi et al., 2022b) and siderite (Dublet et al., 2014) offering another mechanism of attenuation in these systems. In older PRB treatment systems, Ni has been observed as both native Ni and Fe-bearing Ni sulfate (Jambor et al., 2005), however our experimental design was not suited to identify these phases.

3.5 Implications

Methods to improve treatment performance and extend the treatment system lifespan of an OC PRB are beneficial in reducing overall treatment system cost. These column experiments demonstrate that amendments of EVO through soaking and injection can improve treatment performance in mitigating acid mine drainage by sustaining higher rates of DSR which increases alkalinity production and metal removal compared to treatment systems with only solid phase OC. Additional amendments of EVO through injection can re-establish treatment performance providing a means to extend PRB lifespan without replacement. There does not appear to be a difference in the primary mechanism of Fe removal through FeS precipitation in the different test conditions. All systems are very effective in removing Ni. The sustained higher rates of DSR and FeS precipitation may be beneficial to Ni removal in the long-term. There does not appear to be adverse effects to hydraulic characteristics with EVO amendments at the column scale.

The BAC were affected by additions of EVO. Additional investigation into how a BAC changes over time as EVO is exhausted would provide further insight into optimizing the timing of additional injections to maintain treatment performance. Decreasing rates of SO_4 removal along the flow path in the EVO columns has not been observed in other studies and should be an area of further inquiry. Adding EVO to an OC PRB may improve long-term treatment performance through a priming effect that allows for greater utilization of recalcitrant OC or it may be a hinderance to long-term treatment performance of an OC PRB through the OC sulfurization. The volume and timing of EVO additions will likely need to be optimized to balance these opposing effects.

Chapter 4: *Conclusions and Recommendations*

The primary challenge associated with remediating abandoned and orphaned mine sites is the persistent contamination of local water resources with acidic metal-rich drainage. This is evident at Nickel Rim North, an abandoned Ni-Cu mine, where the groundwater contaminant plume is consistent with the initial characterization studies conducted over 25 years ago (Bain, 1996; Benner et al., 1997, 1999). Potential to produce acid mine drainage (AMD) was addressed through the installation of the Nickel Rim North permeable reactive barrier (PRB) in 1995, which was the first field-scale application of an organic carbon (OC) barrier to treat AMD. Early evaluations of its performance demonstrated the potential for this technology to provide cost-effective passive remediation (Benner et al., 1999; 2002). The field study presented here evaluates the Nickel Rim North PRB 26 years after installation. The results of this investigation indicate the PRB remains highly effective at treatment through the promotion of dissimilatory sulfate reduction (DSR). The long-term performance of this PRB suggests the initial treatment system lifespan was underestimated and the field-based study presented in this thesis provides a new datum to refine these estimates.

Measurement of pore-water along a transect through the Nickel Rim North PRB demonstrates a high level of metal removal is still occurring. Pore-water Fe concentrations decrease by 77% through the PRB from a mean concentration of 516 mg $L^{-1}$and there is near complete removal of Ni from pore-water. The removal of Fe in combination with increases in alkalinity results in little to no acid generation potential immediately downgradient of the PRB. Concomitant with Fe removal, there is extensive removal of SO_4 through the PRB with mean concentrations decreasing by 70% from a mean influent concentration of 1,787 mg L^{-1}. Bulk removal rates of Fe and SO_4 are comparable to those calculated after 38 months of treatment and suggests treatment rates have not asymptotically decreased over time as originally anticipated (Benner et al., 2002). Isotopic analysis of pore-water sulfate would suggest DSR is still actively occurring within the PRB and driving the removal of SO_4 and Fe through the precipitation of FeS. Geochemical extractions and mineralogical evaluation of material from the Nickel Rim PRB indicates this is the long-term mechanism of contaminant immobilization.

Bench-scale column experiments evaluated the performance benefits of incorporating EVO into OC PRB material to treat mine-impacted groundwater simulating the contaminant plume entering the Nickel Rim PRB. These experiments demonstrate clear treatment performance benefits in columns where EVO was incorporated versus a control column (CC) that only had solid phase OC reactive material. There was little to no measurable Fe in the effluent of every column at the start of the experiments. The CC effluent Fe concentration sharply increased after 10 pore volumes (PVs) and

remained consistent with influent concentrations thereafter, while EVO soak columns (EVOS) sustained Fe removal for the duration of monitoring (56 PV). In a column where EVO was injected (EVOI), there was increased initial treatment performance compared to the CC but high Fe and SO_4 removal rates were only sustained for 20 PV with Fe effluent approaching influent concentrations after 40 PV. A direct comparison of the two methods of EVO incorporation is not possible due to the incorporation of different amounts of EVO. A second injection of EVO re-established high rates of Fe removal in EVOI after performance waned. Nickel was rapidly removed from pore-water in every column. Sulfur isotopic measurements of pore-water SO_4 along with changes in SO_4 concentration and alkalinity suggests DSR was actively promoted by the inclusion of EVO which in turn, promoted higher rates of metal and SO_4 removal.

The bulk removal rates of SO_4 were an order of magnitude greater in the EVO columns compared to CC and previous column experiments that used solid phase OC (Angai et al., 2022; Waybrant et al., 2002) and the Nickel Rim PRB (Benner et al., 2002). A unique feature of the EVO column experiments, which is not well understood or documented, is the limited removal of SO_4 occurring after pore-water Fe was completely removed. Production of excess sulfide may have resulted in sulfurization of OC which may limit the long-term benefit of EVO additions because a large component of the solid phase OC may become recalcitrant. Although the column results suggest a much higher capacity for treatment with the inclusion of EVO, the implications of these results with respect to scale-up are unclear, particularly if high levels of SO_4 removal can be sustained for years to decades without frequent EVO additions. Some experimental results suggest additions of labile OC sources can have a "priming effect" and result in more complete utilization of more complex OC sources (Z. Zhang et al., 2019) which may support sustained elevated SO_4 removal rates.

Microbial characterization allows for a direct comparison between the communities present in the Nickel Rim PRB and the laboratory column experiments. The overall microbial community structure observed in the Nickel Rim PRB is similar to the column experiments despite a different inoculation source for the column experiments. At the phylum level, Firmicutes is most abundant, followed by Proteobacteria, Actinobacteria and Bacteroidetes. Similar populations have also been observed in sulfate reducing bioreactors (SRBRs) treating mine-impacted waters (Aoyagi et al., 2017; Baldwin et al., 2015; Drennan et al., 2017). The lower overall abundance of Firmicutes in the Nickel Rim North PRB stands out as a key differentiator between the column experiments and previous microbial characterizations of SRBRs. This difference may reflect the aging system with a limited supply of available OC for degradation. The column experiment results do not suggest there is a

relationship between the mean relative abundance of SRB and treatment performance. Additions of EVO appear to proliferate *Desulfosporosinus* and reduce the overall SRB diversity. The promotion of *Desulfosporosinus* may be advantageous if high SO_4 reduction rates are required for remediation due to high flow rates and/or space constraints. The presence of *Desulfosporosinus* in the Nickel Rim PRB and other SRBRs would suggest a similar response could be possible within these treatment systems with EVO additions. However, the long-term performance observed in the Nickel Rim PRB was associated with a diverse SRB community. This is likely a result of the assemblage of microbial pathways that degrade the complex OC sources available and produce a great variety of substrates that can support a diverse SRB community.

Geochemical extraction results and bulk S X-ray absorption near edge spectroscopy (XANES) of solid phase material from the column experiments conducted demonstrate the precipitation of FeS is the dominant immobilization mechanism of S. Geochemical modeling results do not appear to be a good indicator of when low masses of Fe-sulfide mineral phases precipitate due to the rapid kinetics of these reactions. The precipitation of FeS is consistent with what was observed in previous column experiments (Angai et al., 2022; Waybrant et al., 2002) and during the initial investigations of the Nickel Rim PRB (Herbert et al., 1998, 2000). Previous studies suggested a progression of the composition of Fe-sulfide phases over long-term treatment (Jambor et al., 2005) that is not clearly observed to have occurred in our study of the Nickel Rim North PRB.

Cored material from the Nickel Rim PRB characterized using geochemical extractions, optical microscopy, scanning electron microscope - energy dispersive X-ray spectroscopy (SEM-EDX) analysis and S XANES identified FeS as the primary S phase. In contrast, bulk Fe XANES and linear combination fitting (LCF) analysis of the same material suggest there is an appreciable concentration of Fe-oxide phases and some pyrite with no FeS identified. Both framboidal pyrite and Fe-oxide phases were identified during mineralogical characterization using optical microscopy, however these did not appear to be the dominant phases present. Further evaluation of PRB material using XRD, geochemical extractions that target Fe-oxide phases, and other mineralogical techniques may help to resolve these conflicting results and further constrain the long-term immobilization mechanisms. The primary driver of Ni immobilization within column experiments could not be determined. Nickel μXANES and LCF of Ni hotspots, revealed in Nickel Rim PRB thin sections using XRF mapping, identified Ni immobilized through adsorption onto ferrihydrite.

Examination of thin sections from the Nickel Rim PRB revealed Fe-sulfide phases were in close association with more complex organic material and often replaced organic material. The secondary

porosity of these more complex OC structures may provide a more stable geochemical environment for FeS precipitation and suggest an additional benefit of incorporating more complex OC into a PRB over barriers that rely on injection of labile OC sources into aquifer material. This dual porosity characteristic of the reactive material may help reconcile the differences in geochemical modeling results of pore-water from the Nickel Rim PRB and what is observed though mineralogical characterization because the pore-water is more likely sourced from the primary pore space, which is less reduced.

Comparing the results of the Nickel Rim PRB to other OC PRB treating AMD, some factors that improve long-term treatment performance are apparent. It is important for PRBs to be installed prior to surface discharge of the contaminant plume. While SRB have been identified in acidic environments (Church et al., 2007; Sánchez-Andrea et al., 2014) there may be some effects on the cellulose degraders and fermenters that provide suitable OC substrates to promote DSR (Z. Zhang et al., 2019). In addition, acidic waters can have high concentrations of Fe(III) that is a more efficient oxidizer of sulfides than oxygen and can remobilize contaminants trapped in sulfide minerals through oxidative dissolution (Blowes et al., 2014). Under these conditions, S cycling is much more likely and the efficiency of the treatment system decreases. To quantify the amount of S recycling occurring in SRBRs that are treating influent streams with Fe(III), future SRBR studies could utilize S radiotracer techniques (Jørgensen, 1977).

The extent of treatment is a result of the rate of SO_4 reduction and the hydraulic residence time. The thickness of OC PRB installations should be based on sustainable SO_4 reduction rates that are produced by the more recalcitrant OC sources included to ensure a sufficient hydraulic residence time is achieved for sustained long-term treatment. Incorporating EVO through soaking or injection during installation will likely improve the initial contaminant removal rates and promote reducing conditions in the aquifer material downgradient of the PRB. Injections of EVO after installation may accelerate contaminant removal rates during the winter months or if the thickness of the PRB is found to be insufficient to meet remediation objectives.

There is a continued need for long-term evaluations of OC PRBs to better constrain the treatment lifespan of these systems. The results of this project could be improved with better constraints on the hydrogeologic parameters along the transect studied at the Nickel Rim North site. Future tests of EVO injections into aquifer material rather than OC PRB material to treat AMD is needed to determine if there are additional benefits to treatment performance and long-term contaminant immobilization through the incorporation of more complex OC. The Nickel Rim PRB would also

provide a good test location of EVO injections into older PRBs to improve treatment performance as the future studies could directly compare changes in the aqueous geochemistry, microbiology and mineralogy to the results presented here. Field pilot-scale installations of PRBs with OC soaked in EVO are needed to determine if the treatment benefits observed in the EVO soak columns are consistent at longer temporal and larger spatial scales. The conceptual model of what drives long-term Fe and Ni immobilization could be further refined with targeted mineralogical examination of cored material from the Nickel Rim PRB. Despite these needs, the results presented in this thesis further confirm that OC PRBs are a viable passive remediation option to treat mine-impacted groundwater and demonstrate that EVO can be utilized to improve treatment performance in OC PRBs.

References

Adams, B., Anderson, R., Bless, D., Butler, B., Conway, B., Dailey, A., Freed, E., Gervais, G., Gill, M., & Grosse, D. (2014). Reference guide to Treatment Technologies for mining-influenced water. *Washington, USA: US Environmental Protection Agency-OSRTI*, 8–30.

Allison, J. D., Brown, D. S., & Novo-Gradac, K. J. (1998). *MINTEQA2/PRODEFA2, A Geochemical Assessment Model for Environmental Systems: User Manual Supplement for Version 4.0*.

Amos, R. T., Mayer, K. U., Blowes, D. W., & Ptacek, C. J. (2004). Reactive transport modeling of column experiments for the remediation of acid mine drainage. *Environmental Science and Technology*, *38*(11), 3131–3138. https://doi.org/10.1021/es0349608

Angai, J (2020). *Removal of Arsenic and Metals from Mine-impacted Groundwater Using Organic Carbon and Zero-valent Iron in Passive Remediation Systems [MSc]*. University of Waterloo.

Angai, J. U., Ptacek, C. J., Pakostova, E., Bain, J. G., Verbuyst, B. R., & Blowes, D. W. (2022). Removal of arsenic and metals from groundwater impacted by mine waste using zero-valent iron and organic carbon: laboratory column experiments. *Journal of Hazardous Materials*, *424(A), 127295*. https://doi.org/10.1016/j.jhazmat.2021.127295

Antler, G., Turchyn, A. V., Rennie, V., Herut, B., & Sivan, O. (2013). Coupled sulfur and oxygen isotope insight into bacterial sulfate reduction in the natural environment. *Geochimica et Cosmochimica Acta*, *118*, 98–117. https://doi.org/10.1016/j.gca.2013.05.005

Aoyagi, T., Hamai, T., Hori, T., Sato, Y., Kobayashi, M., Sato, Y., Inaba, T., Ogata, A., Habe, H., & Sakata, T. (2017). Hydraulic retention time and pH affect the performance and microbial communities of passive bioreactors for treatment of acid mine drainage. *AMB Express*, *7*(1). https://doi.org/10.1186/s13568-017-0440-z

Aoyagi, T., Hamai, T., Hori, T., Sato, Y., Kobayashi, M., Sato, Y., Inaba, T., Ogata, A., Habe, H., & Sakata, T. (2018). Microbial community analysis of sulfate-reducing passive bioreactor for treating acid mine drainage under failure conditions after long-term continuous operation. *Journal of Environmental Chemical Engineering*, *6*(5), 5795–5800. https://doi.org/10.1016/j.jece.2018.09.003

Arndt, S., Jørgensen, B. B., LaRowe, D. E., Middelburg, J. J., Pancost, R. D., & Regnier, P. (2013). Quantifying the degradation of organic matter in marine sediments: a review and synthesis. *Earth-Science Reviews,* 123, 53–86. https://doi.org/10.1016/j.earscirev.2013.02.008

Arnosti, C. (2011). Microbial extracellular enzymes and the marine carbon cycle. *Annual Review of Marine Science*, *3*, 401–425. https://doi.org/10.1146/annurev-marine-120709-142731

Bain, J. G. (1996). *Hydrogeochemical Investigation and Reactive Transport Modelling of an Aquifer Affected by Mine Drainage [MSc]*. University of Waterloo.

Bain, J. G., Blowes, D. W., Robertson, W. D., & Frind, E. O. (2000). Modelling of sulfide oxidation with reactive transport at a mine drainage site. *Journal of Contaminant Hydrology, 41, 23-47.* \ https://doi.org/10.1016/S0169-7722(99)00069-8

Baldwin, S. A., Khoshnoodi, M., Rezadehbashi, M., Taupp, M., Hallam, S., Mattes, A., Sanei, H., & Puyol, D. (2015). The microbial community of a passive biochemical reactor treating arsenic, zinc, and sulfate-rich seepage. *Frontiers in Bioengineering and Biotechnology, 3.* https://doi.org/10.3389/fbioe.2015.00027

Ball, J., & Nordstrom, K. D. (1991). *User's manual for WATEQ4F, with revised thermodynamic data base and test cases for calculating speciation of major, trace, and redox elements in natural waters*. US Geological Survey.

Benner, S. G., Blowes, D. W., Gould, W. D., Herbert, R. B., & Ptacek, C. J. (1999). Geochemistry of a permeable reactive barrier for metals and acid mine drainage. *Environmental Science and Technology*, *33*(16), 2793–2799. https://doi.org/10.1021/es981040u

Benner, S. G., Blowes, D. W., & Ptacek, C. J. (1997). A full-scale porous reactive wall for prevention of acid mine drainage. *Groundwater Monitoring & Remediation*, *17*(4), 99–107.

Benner, S. G., Blowes, D. W., Ptacek, C. J., & Mayer, K. U. (2002). Rates of sulfate reduction and metal sulfide precipitation in a permeable reactive barrier. *Applied Geochemistry*, *17*(3), 301–320. https://doi.org/10.1016/S0883-2927(01)00084-1

Benner, S. G., Gould, W. D., & Blowes, D. W. (2000). Microbial populations associated with the generation and treatment of acid mine drainage. *Chemical Geology*, *169*(3–4), 435–448. https://doi.org/10.1016/S0009-2541(00)00219-9

Bethke, C. M., Sanford, R. A., Kirk, M. F., Jin, Q., & Flynn, T. M. (2011). The thermodynamic ladder in geomicrobiology. *American Journal of Science*, *311*(3), 183–210. https://doi.org/10.2475/03.2011.01

Blowes, D. W., & Jambor, J. L. (1990). The pore-water geochemistry and the mineralogy of the vadose zone. *Applied Geochemistry*, *5*, 327–346.

Blowes, D. W., Ptacek, C. J., Benner, S. G., McRae, C. W. T., Bennett, T. A., & Puls, R. W. (2000). Treatment of inorganic contaminants using permeable reactive barriers. *Journal of Contaminant Hydrology*, *45*(1–2), 123–137. https://doi.org/10.1016/S0169-7722(00)00122-4

Blowes, D. W., Ptacek, C. J., Jambor, J. L., Weisener, C. G., Paktunc, D., Gould, W. D., & Johnson, D. B. (2014). The geochemistry of acid mine drainage. In *Treatise on Geochemistry: Second Edition*, 11, 131–190. https://doi.org/10.1016/B978-0-08-095975-7.00905-0

Borden, R. C. (2007). Effective distribution of emulsified edible oil for enhanced anaerobic bioremediation. *Journal of Contaminant Hydrology*, *94*(1–2), 1–12. https://doi.org/10.1016/j.jconhyd.2007.06.001

Boudeau, B., & Westrich, J. (1984). The dependence of bacterial sulfate reduction on sulfate concentration in marine sediments. *Geochimica et Cosmochimica Acta*, *48*, 2503–2516.

Brunner, B., Bernasconi, S. M., Kleikemper, J., & Schroth, M. H. (2005). A model for oxygen and sulfur isotope fractionation in sulfate during bacterial sulfate reduction processes. *Geochimica et Cosmochimica Acta, 69(20), 4773-4785.* https://doi.org/10.1016/j.gca.2005.04.017

Burns, A. S., Pugh, C. W., Yosief, S.T., Behum, P. T., Lefticariu, L., & Bender, K. S. (2012). Performance and microbial community dynamics of a sulfate-reducing bioreactor treating coal generated acid mine drainage. *Biodegradation*, *23*, 415–429. https://doi.org/10.1007/s10532-011-9520-y

Cabrera, G., Pérez, R., Gómez, J. M., Ábalos, A., & Cantero, D. (2006). Toxic effects of dissolved heavy metals on Desulfovibrio vulgaris and Desulfovibrio sp. strains. *Journal of Hazardous Materials*, *135*(1–3), 40–46. https://doi.org/10.1016/j.jhazmat.2005.11.058

Canfield, D. E., Raiswell, R., Westrich, J. T., Reaves, C. M., & Berner, R. A. (1986). The use of chromium reduction in the analysis of reduced inorganic sulfur in sediments and shales. *Chemical Geology*, *54*(1–2), 149–155. https://doi.org/10.1016/0009-2541(86)90078-1

Canfield, D. E., & Thamdrup, B. (1994). The production of 34S-depleted sulfide during bacterial disproportionation of elemental sulfur. *Science*, *266*(5193), 1973–1975.

Caraballo, M. A., Santofimia, E., & Jarvis, A. P. (2010). Metal retention, mineralogy, and design considerations of a mature permeable reactive barrier (PRB) for acidic mine water drainage in Northumberland, U.K. *American Mineralogist*, *95*(11–12), 1642–1649. https://doi.org/10.2138/am.2010.3505

Chen, S., Cheng, H., Wyckoff, K. N., & He, Q. (2016). Linkages of Firmicutes and Bacteroidetes populations to methanogenic process performance. *Journal of Industrial Microbiology and Biotechnology*, *43*(6), 771–781. https://doi.org/10.1007/s10295-016-1760-8

Church, C. D., Wilkin, R. T., Alpers, C. N., Rye, R. O., & Blaine, R. B. (2007). Microbial sulfate reduction and metal attenuation in pH 4 acid mine water. *Geochemical Transactions*, *8*. https://doi.org/10.1186/1467-4866-8-10

Cornwell, J. C., & Morse, J. W. (1987). The characterization of iron sulfide minerals in anoxic marine sediments. *Marine Chemistry*, 22(2–4), 193–206.

Coulibaly, K. M., & Borden, R. C. (2004). Impact of edible oil injection on the permeability of aquifer sands. *Journal of Contaminant Hydrology*, *71*(1–4), 219–237. https://doi.org/10.1016/J.JCONHYD.2003.10.002

Daignault, E. (2002). *The solid phase sulfur speciation of metal sulphides in a permeable reactive barrier, Nickel Rim mine, Sudbury, Ontario [BSc]*. University of Waterloo.

Damste, J. S. S., & De Leeuw, J. W. (1989). Advances in Organic Geochemistry. *Organic. Geochemistry, 16(4–6), 1077– 1101*.

Deng, Y., Zhang, P., Qin, Y., Tu, Q., Yang, Y., He, Z., Schadt, C. W., & Zhou, J. (2016). Network succession reveals the importance of competition in response to emulsified vegetable oil amendment for uranium bioremediation. *Environmental Microbiology*, *18*(1), 205–218. https://doi.org/10.1111/1462-2920.12981

DeNicola, D. M., & Stapleton, M. G. (2002). Impact of acid mine drainage on benthic communities in streams: the relative roles of substratum vs. aqueous effects. *Environmental Pollution*, *119*(3), 303–315. https://doi.org/10.1016/S0269-7491(02)00106-9

Doerr, N. A., Ptacek, C. J., & Blowes, D. W. (2005). Effects of a reactive barrier and aquifer geology on metal distribution and mobility in a mine drainage impacted aquifer. *Journal of Contaminant Hydrology*, *78*(1–2), 1–25. https://doi.org/10.1016/j.jconhyd.2005.02.005

Drennan, D. M., Almstrand, R., Ladderud, J., Lee, I., Landkamer, L., Figueroa, L., & Sharp, J. O. (2017). Spatial impacts of inorganic ligand availability and localized microbial community structure on mitigation of zinc laden mine water in sulfate-reducing bioreactors. *Water Research*, *115*, 50–59. https://doi.org/10.1016/j.watres.2017.02.037

Drennan, D. M., Almstrand, R., Lee, I., Landkamer, L., Figueroa, L., & Sharp, J. O. (2016). Organoheterotrophic bacterial abundance associates with zinc removal in lignocellulose-based

sulfate-reducing systems. *Environmental Science and Technology*, *50*(1), 378–387. https://doi.org/10.1021/acs.est.5b04268

Druhan, J. L., Steefel, C. I., Conrad, M. E., & Depaolo, D. J. (2013). A large column analog experiment of stable isotope variations during reactive transport: I. A comprehensive model of sulfur cycling and d 34 S fractionation. *Geochemica et Cosmochemica Acta, 124, 366-393*. https://doi.org/10.1016/j.gca.2013.08.037

Druhan, J. L., Steefel, C. I., Molins, S., Williams, K. H., Conrad, M. E., & Depaolo, D. J. (2012). Timing the onset of sulfate reduction over multiple subsurface acetate amendments by measurement and modeling of sulfur isotope fractionation. *Environmental Science and Technology*, *46*(16), 8895–8902. https://doi.org/10.1021/es302016p

Dublet, G., Juillot, F., Morin, G., Fritsch, E., Noel, V., Brest, J., & Brown, G. E. (2014). XAS evidence for Ni sequestration by siderite in a lateritic Ni-deposit from New Caledonia. *American Mineralogist*, *99*(1), 225–234. https://doi.org/10.2138/am.2014.4625

España, J. S., Pamo, E. L., Santofimia, E., Aduvire, O., Reyes, J., & Barettino, D. (2005). Acid mine drainage in the Iberian Pyrite Belt (Odiel river watershed, Huelva, SW Spain): Geochemistry, mineralogy and environmental implications. *Applied Geochemistry*, *20*(7), 1320–1356. https://doi.org/10.1016/j.apgeochem.2005.01.011

ESRF. (2023). *Database organic sulfur compounds.* https://www.Esrf.Fr/Home/UsersAndScience/Experiments/XNP/ID21/Php/Database-SOrganic.Html.

Findlay, A. J., & Kamyshny, A. (2017). Turnover rates of intermediate sulfur species (Sx2-, S0, S2O32-, S4O62-, SO32-) in anoxic freshwater and sediments. *Frontiers in Microbiology*, *8*(DEC). https://doi.org/10.3389/fmicb.2017.02551

Fotherby, A., Bradbury, H. J., Antler, G., Sun, X., Druhan, J. L., & Turchyn, A. V. (2021). Modelling the effects of non-steady state transport dynamics on the sulfur and oxygen isotope composition of sulfate in sedimentary pore fluids. *Frontiers in Earth Science*, *8*. https://doi.org/10.3389/feart.2020.587085

Giannetta, M. G., Sanford, R. A., & Druhan, J. L. (2019). A modified Monod rate law for predicting variable S isotope fractionation as a function of sulfate reduction rate. *Geochimica et Cosmochimica Acta*, *258*, 174–194. https://doi.org/10.1016/j.gca.2019.05.015

Gibert, O., Rötting, T., Cortina, J. L., de Pablo, J., Ayora, C., Carrera, J., & Bolzicco, J. (2011). In-situ remediation of acid mine drainage using a permeable reactive barrier in Aznalcóllar (SW

Spain). *Journal of Hazardous Materials*, *191*(1–3), 287–295. https://doi.org/10.1016/j.jhazmat.2011.04.082

Gibson, B. D., Amos, R. T., & Blowes, D. W. (2011). 34 S/ 32 S Fractionation during sulfate reduction in groundwater treatment systems: reactive transport modeling. *Environmental Science and Technolology*, *45*, 2863–2870. https://doi.org/10.1021/es1038276

Gihring, T. M., Zhang, G., Brandt, C. C., Brooks, S. C., Campbell, J. H., Carroll, S., Criddle, C. S., Green, S. J., Jardine, P., Kostka, J. E., Lowe, K., Mehlhorn, T. L., Overholt, W., Watson, D. B., Yang, Z., Wu, W. M., & Schadt, C. W. (2011). A limited microbial consortium is responsible for extended bioreduction of uranium in a contaminated aquifer. *Applied and Environmental Microbiology*, *77*(17), 5955–5965. https://doi.org/10.1128/AEM.00220-11

Glombitza, F. (2001). Treatment of acid lignite mine flooding water by means of microbial sulfate reduction. *Waste Management*, *21*, 197–203. www.elsevier.nl/locate/wasman

Göker, M., Teshima, H., Lapidus, A., Nolan, M., Lucas, S., Hammon, N., Deshpande, S., Cheng, J.-F., Tapia, R., Han, C., Goodwin, L., Pitluck, S., Huntemann, M., Liolios, K., Ivanova, N., Pagani, I., Mavromatis, K., Ovchinikova, G., Pati, A., … Klenk, H.-P. (2011). Complete genome sequence of the acetate-degrading sulfate reducer Desulfobacca acetoxidans type strain (ASRB2T). *Standards in Genomic Sciences*, *4*(3), 393–401. https://doi.org/10.4056/sigs.2064705

Gomes, M. L., & Johnston, D. T. (2017). Oxygen and sulfur isotopes in sulfate in modern euxinic systems with implications for evaluating the extent of euxinia in ancient oceans. *Geochimica et Cosmochimica Acta*, *205*, 331–359. https://doi.org/10.1016/j.gca.2017.02.020

Guenet, B., Danger, M., Abbadie, L., & Lacroix, G. (2010). Priming effect: bridging the gap between terrestrial and aquatic ecology. *Ecology*, *91*(10), 2850–2861. https://doi.org/10.1890/09-1968.1

Guo, Q., & Blowes, D. W. (2009). Biogeochemistry of two types of permeable reactive barriers, organic carbon and iron-bearing organic carbon for mine drainage treatment: Column experiments. *Journal of Contaminant Hydrology*, *107*(3–4), 128–139. https://doi.org/10.1016/j.jconhyd.2009.04.008

Habe, H., Sato, Y., Aoyagi, T., Inaba, T., Hori, T., Hamai, T., Hayashi, K., Kobayashi, M., Sakata, T., & Sato, N. (2020). Design, application, and microbiome of sulfate-reducing bioreactors for treatment of mining-influenced water. *Applied Microbiology and Biotechnology*, *104*, 6893–6903. https://doi.org/10.1007/s00253-020-10737-2/Published

He, Y. T., Wilson, J. T., & Wilkin, R. T. (2008). Transformation of reactive iron minerals in a permeable reactive barrier (Biowall) used to treat TCE in groundwater. *Environmental Science and Technology*, *42*(17), 6690–6696. https://doi.org/10.1021/es8010354

He, Y. T., Wilson, J. T., & Wilkin, R. T. (2010). Impact of iron sulfide transformation on trichloroethylene degradation. *Geochimica et Cosmochimica Acta*, *74*(7), 2025–2039. https://doi.org/10.1016/j.gca.2010.01.013

Hemsi, P. S., Shackelford, C. D., & Figueroa, L. A. (2005). Modeling the influence of decomposing organic solids on sulfate reduction rates for iron precipitation. *Environmental Science and Technology*, *39*(9), 3215–3225. https://doi.org/10.1021/es0486420

Henderson, A. D., & Demond, A. H. (2007). Long-term performance of zero-valent iron permeable reactive barriers: A critical review. *Environmental Engineering Science*, *24*(4), 401–423. https://doi.org/10.1089/ees.2006.0071

Herbert, R. B., Benner, S. G., & Blowes, D. W. (1998). Reactive barrier treatment of groundwater contaminated by acid mine drainage: Sulphur accumulation and sulphide formation. *IAHS-AISH Publication*, *250*, 451–457.

Herbert, R. B., Benner, S. G., & Blowes, D. W. (2000). Solid phase iron-sulfur geochemistry of a reactive barrier for treatment of mine drainage. *Applied Geochemistry*, *15*(9), 1331–1343. https://doi.org/10.1016/S0883-2927(00)00005-6

Hiibel, S. R., Pereyra, L. P., Breazeal, M. V. R., Reisman, D. J., Reardon, K. F., & Pruden, A. (2011). Effect of organic substrate on the microbial community structure in pilot-scale sulfate-reducing biochemical reactors treating mine drainage. *Environmental Engineering Science*, *28*(8), 563–572. https://doi.org/10.1089/EES.2010.0237

Hogsden, K. L., & Harding, J. S. (2012). Consequences of acid mine drainage for the structure and function of benthic stream communities: a review. *Freshwater Science*, 31(1). 108–120. https://doi.org/10.1899/11-091.1

Hunger, S., & Benning, L. G. (2007). Greigite: a true intermediate on the polysulfide pathway to pyrite. *Geochemical Transactions 8(1).* https://doi.org/10.1186/1467-4866-8-1

Hunter, W. J. (2001). Use of vegetable oil in a pilot-scale denitrifying barrier. *Journal of Contaminant Hydrology*, *53*(1–2), 119–131. https://doi.org/10.1016/S0169-7722(01)00137-1

ICOLD. (1996). *A Guide to Tailings Dams and Impoundments: Design, Construction, Use and Rehabilitation*.

ITRC. (2011). Technology Update: Permeable Reactive Barriers. In *PBR-5. Washington, DC: Interstate Technology & Regulatory Council, PRB: Technology Update Team*.

Jambor, J. L., Raudsepp, M., & Mountjoy, K. (2005). Mineralogy of permeable reactive barriers for the attenuation of subsurface contaminants. *Canadian Mineralogist*, *43*(6), 2117–2140. https://doi.org/10.2113/gscanmin.43.6.2117

Janzen, M. P., Nicholson, R. V, & Scharer, J. M. (2000). Pyrrhotite reaction kinetics: Reaction rates for oxidation by oxygen, ferric iron, and for nonoxidative dissolution. *Geochimica et Cosmochimica Acta*, *64*(9), 1511–1522. https://doi.org/10.1016/S0016-7037(99)00421-4

Jarvis, A. P., Moustafa, M., Orme, P. H. A., & Younger, P. L. (2006). Effective remediation of grossly polluted acidic, and metal-rich, spoil heap drainage using a novel, low-cost, permeable reactive barrier in Northumberland, UK. *Environmental Pollution*, *143*(2), 261–268. https://doi.org/10.1016/j.envpol.2005.11.028

Johnson, D. B., & Hallberg, K. B. (2005). Acid mine drainage remediation options: A review. *Science of the Total Environment*, *338*(1-2 SPEC. ISS.), 3–14. https://doi.org/10.1016/j.scitotenv.2004.09.002

Johnson, R. H., Blowes, D. W., Robertson, W. D., & Jambor, J. L. (2000). The hydrogeochemistry of the Nickel Rim mine tailings impoundment, Sudbury, Ontario. *Journal of Contaminant Hydrology*, *41*(1–2), 49–80. https://doi.org/10.1016/S0169-7722(99)00068-6

Jørgensen, B. B. (1977). The sulfur cycle of a coastal marine sediment (Limfjorden, Denmark). *Limnology and Oceanography*, *22*(5), 814–832. https://doi.org/10.4319/lo.1977.22.5.0814

Kaksonen, A. H., Spring, S., Schumann, P., Kroppenstedt, R. M., & Puhakka, J. A. (2007). Desulfurispora thermophila gen. nov., sp. nov., a thermophilic, spore-forming sulfate-reducer isolated from a sulfidogenic fluidized-bed reactor. *International Journal of Systematic and Evolutionary Microbiology*, *57*(5), 1089–1094. https://doi.org/10.1099/ijs.0.64593-0

Karhadkar, P. P., Audic, J.-M., Faup, G. M., & Khanna, P. (1987). Sulfide and sulfate inhibition of methanogensis. *Water Research, 21(9)*, 1061-1066.

Kozich, J. J., Westcott, S. L., Baxter, N. T., Highlander, S. K., & Schloss, P. D. (2013). Development of a dual-index sequencing strategy and curation pipeline for analyzing amplicon sequence data on the miseq illumina sequencing platform. *Applied and Environmental Microbiology*, *79*(17), 5112–5120. https://doi.org/10.1128/AEM.01043-13

Leavitt, W. D., Halevy, I., Bradley, A. S., & Johnston, D. T. (2013). Influence of sulfate reduction rates on the Phanerozoic sulfur isotope record. *Proceedings of the National Academy of Sciences*

of the United States of America, *110*(28), 11244–11249. https://doi.org/10.1073/pnas.1218874110

Leblanc, M., Morales, J. A., Borrego, J., & Elbaz-Poulichet, F. (2000). 4,500-year-old mining pollution in southwestern Spain: long-term implications for modern mining pollution. *Economic Geology*, *95*, 655–662.

Lee, T. R., & Wilkin, R. T. (2010). Iron hydroxy carbonate formation in zerovalent iron permeable reactive barriers: Characterization and evaluation of phase stability. *Journal of Contaminant Hydrology*, *116*(1–4), 47–57. https://doi.org/10.1016/j.jconhyd.2010.05.009

Lefticariu, L., Walters, E. R., Pugh, C. W., & Bender, K. S. (2015). Sulfate reducing bioreactor dependence on organic substrates for remediation of coal-generated acid mine drainage: Field experiments. *Applied Geochemistry*, *63*, 70–82. https://doi.org/10.1016/j.apgeochem.2015.08.002

Legrand, R., Maestas, K. M., Henry, R. L., Bain, J. G., Blowes, D. W., Strunk, J. F., & Chai, Y. (2016). Pilot testing of a permeable reactive barrier (PRB) to remediate sulfate, metals, and low pH in groundwater. *2016 SME Annual Conference and Expo: The Future for Mining in a Data-Driven World*, 723-728.

Li, L., Steefel, C. I., Williams, K. H., Wilkins, M. J., & Hubbard, S. S. (2009). Mineral transformation and biomass accumulation associated with uranium bioremediation at Rifle, Colorado. *Environmental Science and Technology*, *43*(14), 5429–5435. https://doi.org/10.1021/es900016v

Light, T. S. (1972). Standard solution for redox potential measurements. *Analytical Chemistry*, *44.6*, 1038–1039.

Lindow, N. L., & Borden, R. C. (2004). Anaerobic bioremediation of acid mine drainage using EOS. *Journal American Society of Mining and Reclamation*, *2004*(1), 1192–1204. https://doi.org/10.21000/jasmr04011192

Lindsay, M. B. J., Blowes, D. W., Condon, P. D., & Ptacek, C. J. (2009). Managing pore-water quality in mine tailings by inducing microbial sulfate reduction. *Environmental Science and Technology*, *43*(18), 7086–7091. https://doi.org/10.1021/es901524z

Lindsay, M. B. J., Blowes, D. W., Ptacek, C. J., & Condon, P. D. (2011). Transport and attenuation of metal(loid)s in mine tailings amended with organic carbon: Column experiments. *Journal of Contaminant Hydrology*, *125*(1–4), 26–38. https://doi.org/10.1016/j.jconhyd.2011.04.004

Lindsay, M. B. J., Moncur, M. C., Bain, J. G., Jambor, J. L., Ptacek, C. J., & Blowes, D. W. (2015). Geochemical and mineralogical aspects of sulfide mine tailings. *Applied Geochemistry*, *57*, 157–177. https://doi.org/10.1016/j.apgeochem.2015.01.009

Lindsay, M. B. J., Ptacek, C. J., Blowes, D. W., & Gould, W. D. (2008). Zero-valent iron and organic carbon mixtures for remediation of acid mine drainage: Batch experiments. *Applied Geochemistry*, *23*(8), 2214–2225. https://doi.org/10.1016/j.apgeochem.2008.03.005

Liu, P., Ptacek, C. J., Blowes, D. W., & Landis, R. C. (2016). Mechanisms of mercury removal by biochars produced from different feedstocks determined using X-ray absorption spectroscopy. *Journal of Hazardous Materials*, *308*, 233–242. https://doi.org/10.1016/J.JHAZMAT.2016.01.007

Lloyd, R. (1968). Oxygen isotope behavior in the sulfate-water system. *Journal of Geophysical Research*, *73*(18), 6099–6110. https://doi.org/10.1029/JB073I018P06099

Logan, M. V., Reardon, K. F., Figueroa, L. A., McLain, J. E. T., & Ahmann, D. M. (2005). Microbial community activities during establishment, performance, and decline of bench-scale passive treatment systems for mine drainage. *Water Research*, *39*(18), 4537–4551. https://doi.org/10.1016/j.watres.2005.08.013

Lozupone, C., & Knight, R. (2005). UniFrac: A new phylogenetic method for comparing microbial communities. *Applied and Environmental Microbiology*, *71*(12), 8228–8235. https://doi.org/10.1128/AEM.71.12.8228-8235.2005

Ludwig, R. D., McGregor, R. G., Blowes, D. W., Benner, S. G., & Mountjoy, K. (2002). A permeable reactive barrier for treatment of heavy metals. *Groundwater*, *40*(1), 59–66. https://doi.org/10.1111/J.1745-6584.2002.TB02491.X

Ludwig, R. D., Smyth, D. J. A., Blowes, D. W., Spink, L. E., Wilkin, R. T., Jewett, D. G., & Weisener, C. J. (2009). Treatment of arsenic, heavy metals, and acidity using a mixed ZVI-compost PRB. *Environmental Science and Technology*, *43*(6), 1970–1976. https://doi.org/10.1021/ES802394P/SUPPL_FILE/ES802394P_SI_001.PDF

Machemer, S. D., Reynolds, J. S., Laudon, L. S., & Wildeman, T. R. (1993). Balance of S in a constructed wetland built to treat acid mine drainage, Idaho Springs, Colorado, U.S.A. *Applied Geochemistry*, *8*(6), 587–603. https://doi.org/10.1016/0883-2927(93)90015-9

Mardanov, A. V., Panova, I. A., Beletsky, A. V., Avakyan, M. R., Kadnikov, V. V., Antsiferov, D. V., Banks, D., Frank, Y. A., Pimenov, N. V., Ravin, N. V., & Karnachuk, O. V. (2016). Genomic insights into a new acidophilic, copper-resistant Desulfosporosinus isolate from the

oxidized tailings area of an abandoned gold mine. *FEMS Microbiology Ecology*, *92*(8). https://doi.org/10.1093/femsec/fiw111

Mayer, K. U., Benner, S. G., & Blowes, D. W. (2006). Process-based reactive transport modeling of a permeable reactive barrier for the treatment of mine drainage. *Journal of Contaminant Hydrology*, *85*(3–4), 195–211. https://doi.org/10.1016/j.jconhyd.2006.02.006

McGregor, R. G., & Blowes, D. W. (2002). The physical, chemical and mineralogical properties of three cemented layers within sulfide-bearing mine tailings. *Journal of Geochemical Exploration*, *76*(3), 195–207. https://doi.org/10.1016/S0375-6742(02)00255-8

Mills, J. V, Antler, G., & Turchyn, A. V. (2016). Geochemical evidence for cryptic sulfur cycling in salt marsh sediments. *Earth and Planetary Science Letters*, *453*, 23–32. https://doi.org/10.1016/j.epsl.2016.08.001

Mirjafari, P., & Baldwin, S. A. (2016). Decline in performance of biochemical reactors for sulphate removal from mine-influenced water is accompanied by changes in organic matter characteristics and microbial population composition. *Water (Switzerland)*, *8*(4). https://doi.org/10.3390/w8040124

Moncur, M. C., Ptacek, C. J., Blowes, D. W., & Jambor, J. L. (2005). Release, transport and attenuation of metals from an old tailings impoundment. *Applied Geochemistry*, *20*(3), 639–659. https://doi.org/10.1016/j.apgeochem.2004.09.019

Moncur, M. C., Ptacek, C. J., Hayashi, M., Blowes, D. W., & Birks, S. J. (2014). Seasonal cycling and mass-loading of dissolved metals and sulfate discharging from an abandoned mine site in northern Canada. *Applied Geochemistry*, *41*, 176–188. https://doi.org/10.1016/J.APGEOCHEM.2013.12.007

Morse, J. W., & Arakaki, T. (1993). Adsorption and coprecipitation of divalent metals with mackinawite (FeS). *Geochimica et Cosmochimica Acta*, *57*(15), 3635–3640. https://doi.org/10.1016/0016-7037(93)90145-M

Morse, J. W., & Cornwell, J. C. (1987). Analysis and distribution of iron sulfide minerals in recent anoxic marine sediments. *Marine Chemistry,* 22.

Muller, K. A., Esfahani, S. G., Chapra, S. C., & Ramsburg, C. A. (2018). Transport and retention of concentrated oil-in-water emulsions in porous media. *Environmental Science and Technology*, 52(7), 4256–4264. https://doi.org/10.1021/acs.est.7b06012

Naftz, D. L., Fuller, C. C., Davis}, J. A., Morrison, S. J., Feltcom, E. M., Freethey, G. W., Rowland, R. C., Wilkowske, C., & Pian, M. (2002). Field demonstration of three permeable reactive

barriers to control uranium contamination in groundwater, Fry Canyon, Utah. In *Handbook of groundwater remediation using permeable reactive barriers, 401-434.*

Neculita, C.-M., Zagury, G. J., & Bussière, B. (2007). Passive treatment of acid mine drainage in bioreactors using sulfate-reducing bacteria. *Journal of Environmental Quality*, *36*(1), 1–16. https://doi.org/10.2134/jeq2006.0066

Newville, M. (2013). Larch: An analysis package for XAFS and related spectroscopies. *Journal of Physics: Conference Series*, *430*(1). https://doi.org/10.1088/1742-6596/430/1/012007

Nicholson, R. V, & Scharer, J. M. (1994). Laboratory studies of pyrrhotite oxidation kinetics. In C. N. Alpers & D. W. Blowes (Eds.), *Environmental Geochemistry of Sulfide Oxidation*, 550, 14–30. American Chemical Society Symposium Series. https://doi.org/10.1021/bk-1994-0550.ch002

Nielsen, G., Hatam, I., Abuan, K. A., Janin, A., Coudert, L., Blais, J. F., Mercier, G., & Baldwin, S. A. (2018). Semi-passive in-situ pilot scale bioreactor successfully removed sulfate and metals from mine impacted water under subarctic climatic conditions. *Water Research*, *140*, 268–279. https://doi.org/10.1016/j.watres.2018.04.035

Nordstrom, K. D. (1977). Thermochemical redox equilibria of ZoBell's solution. *Geochimica et Cosmochimica Acta, 41(12), 1835-1841.*

Nordstrom, K. D. (1982). Aqueous pyrite oxidation and the consequent formation of secondary iron minerals. *Acid Sulfate Weathering*, *10*, 37–56.

Parigi, R., Pakostova, E., Reid, J. W., Saurette, E. M., McBeth, J. M., Ptacek, C. J., & Blowes, D. W. (2022a). Nickel isotope fractionation as an indicator of Ni sulfide precipitation associated with microbially mediated sulfate reduction. *Environmental Science and Technology*, *56*(12), 7954–7962. https://doi.org/10.1021/acs.est.2c00523

Parigi, R., Chen, N., Liu, P., Ptacek, C. J., & Blowes, D. W. (2022b). Mechanisms of Ni removal from contaminated groundwater by calcite using X-ray absorption spectroscopy and Ni isotope measurements. *Journal of Hazardous Materials*, *440*, 129679. https://doi.org/10.1016/j.jhazmat.2022.129679

Parkhurst, D., & Appelo. (2013). Description of input and examples for PHREEQC version 3: a computer program for speciation, batch-reaction, one-dimensional transport, and inverse geochemical calculations*. US geological Survey Techniques and Methods*, 6(A43), 497.

Pellerin, A., Antler, G., Holm, S. A., Findlay, A. J., Crockford, P. W., Turchyn, A. V, Jørgensen, B. B., & Finster, K. (2019). Large sulfur isotope fractionation by bacterial sulfide oxidation. *Science Advances, 5(7)*. https://doi.org/10.1126/sciadv.aaw1480

Pester, M., Brambilla, E., Alazard, D., Rattei, T., Weinmaier, T., Han, J., Lucas, S., Lapidus, A., Cheng, J. F., Goodwin, L., Pitluck, S., Peters, L., Ovchinnikova, G., Teshima, H., Detter, J. C., Han, C. S., Tapia, R., Land, M. L., Hauser, L., … Loy, A. (2012). Complete genome sequences of Desulfosporosinus orientis DSM765T, Desulfosporosinus youngiae DSM17734T, Desulfosporosinus meridiei DSM13257T, and Desulfosporosinus acidiphilus DSM22704T. *Journal of Bacteriology, 194(22),* 6300–6301. https://doi.org/10.1128/JB.01392-12

Rabus, R., Hansen, T. A., & Widdel, F. (2013). Dissimilatory sulfate- and sulfur-reducing prokaryotes. *The Prokaryotes: Prokaryotic Physiology and Biochemistry*, 309–404. https://doi.org/10.1007/978-3-642-30141-4_70

Rabus, R., Venceslau, S. S., Wöhlbrand, L., Voordouw, G., Wall, J. D., & Pereira, I. A. C. (2015). A post-genomic view of the ecophysiology, catabolism and biotechnological relevance of sulphate-reducing prokaryotes. *Advances in Microbial Physiology*, 66, 55–321. https://doi.org/10.1016/bs.ampbs.2015.05.002

Raven, M. R., Keil, R. G., & Webb, S. M. (2021). Microbial sulfate reduction and organic sulfur formation in sinking marine particles. *Science*, *371*, 178–181. https://www.science.org

Rees, C. E. (1973). A steady-state model for sulphur isotope fractionation in bacterial reduction processes. *Geochimica et Cosmochimica Acta*, *37*(5), 1141–1162. https://doi.org/10.1016/0016-7037(73)90052-5

Reis, M. A. M., Almeida, J. S., Lemos, P. C., & Carrondo, M. J. T. (1992). Effect of hydrogen sulfide on growth of sulfate reducing bacteria. *Biotechnology and Bioengineering*, *40*(5), 593–600. https://doi.org/10.1002/bit.260400506

Reis, M. A. M., Lemos, P. C., Almeida, J. S., & Carronda, M. J. T. (1990). Influence of produced acetic acid on growth of sulfate reducing bacteria. *Biotechnology Letters (12),* 145–148

Rezadehbashi, M., & Baldwin, S. A. (2018). Core sulphate-reducing microorganisms in metal-removing semi-passive biochemical reactors and the co-occurrence of methanogens. *Microorganisms*, *6*(1). https://doi.org/10.3390/microorganisms6010016

Ribet, I., Ptacek, C. J., Blowes, D. W., & Jambor, J. L. (1995). The potential for metal release by reductive dissolution of weathered mine tailings. *Journal of Contaminant Hydrology*, *17*(3), 239–273. https://doi.org/10.1016/0169-7722(94)00010-F

Rice, C. A., Tuttle, M. L., & Reynolds, R. L. (1993). The analysis of forms of sulfur in ancient sediments and sedimentary rocks: comments and cautions. *Chemical Geology, 107 (1–2), 83–95*.

Rickard, D., & Luther, G. W. (2007). Chemistry of iron sulfides. *Chemical Reviews, 107(2*), 514–562. https://doi.org/10.1021/cr0503658

Rickard, D., & Morse, J. W. (2005). Acid volatile sulfide (AVS). *Marine Chemistry, 97(3–4)*, 141–197. https://doi.org/10.1016/j.marchem.2005.08.004

Sánchez-Andrea, I., Rodríguez, N., Amils, R., & Sanz, J. L. (2011). Microbial diversity in anaerobic sediments at Río Tinto, a naturally acidic environment with a high heavy metal content. *Applied and Environmental Microbiology*, *77*(17), 6085–6093. https://doi.org/10.1128/AEM.00654-11

Sánchez-Andrea, I., Sanz, J. L., Bijmans, M. F. M., & Stams, A. J. M. (2014). Sulfate reduction at low pH to remediate acid mine drainage. *Journal of Hazardous Materials*, *269*, 98–109. https://doi.org/10.1016/j.jhazmat.2013.12.032

Schloss, P. D., Westcott, S. L., Ryabin, T., Hall, J. R., Hartmann, M., Hollister, E. B., Lesniewski, R. A., Oakley, B. B., Parks, D. H., Robinson, C. J., Sahl, J. W., Stres, B., Thallinger, G. G., van Horn, D. J., & Weber, C. F. (2009). Introducing mothur: Open-source, platform-independent, community-supported software for describing and comparing microbial communities. *Applied and Environmental Microbiology*, *75*(23), 7537–7541. https://doi.org/10.1128/AEM.01541-09

Schmidtova, J., & Baldwin, S. A. (2011). Correlation of bacterial communities supported by different organic materials with sulfate reduction in metal-rich landfill leachate. *Water Research*, *45*(3), 1115–1128. https://doi.org/10.1016/j.watres.2010.10.038

Sim, M. S., Bosak, T., & Ono, S. (2011). Large sulfur isotope fractionation does not require disproportionation. *Science*, *333*(6038), 74–77. https://doi.org/10.1126/science.1205103

Simunek, J., Van Genuchten, M. T., Sejna, M., Toride, N., & Leij, F. J. (1999). The STANMOD computer software for evaluating solute transport in porous media using analytical solutions of convection-dispersion equation. Versions 1.0 and 2.0. *Rep. IGWMC-TPS*, *71*, 32.

Shi, Z., Peltier, E., & Sparks, D. L. (2012). Kinetics of Ni sorption in soils: roles of soil organic matter and Ni precipitation, *Environmental Science and Technology,* 46, 2212-2219.

Starr, R. C., & Ingleton, R. A. (1992). A new method for collecting core samples without a drilling rig. *Groundwater Monitoring & Remediation*, 12(1), 91–95. https://doi.org/10.1111/j.1745-6592.1992.tb00413.x

Swanner, E. D., Webb, S. M., & Kappler, A. (2019). Fate of cobalt and nickel in mackinawite during diagenetic pyrite formation. *American Mineralogist*, *104*(7), 917–928. https://doi.org/10.2138/am-2019-6834

Tang, G., Wu, W. M., Watson, D. B., Parker, J. C., Schadt, C. W., Shi, X., & Brooks, S. C. (2013). U(VI) bioreduction with emulsified vegetable oil as the electron donor -microcosm tests and model development. *Environmental Science and Technology*, *47*(7), 3209–3217. https://doi.org/10.1021/es304641b

Toride, N., Leij, F. J., Van Genuchten, M. T., & others. (1995). The CXTFIT code for estimating transport parameters from laboratory or field tracer experiments (Vol. 2). Riverside, CA. US Salinity Laboratory.

Tsukamoto, T. K., Killion, H. A., & Miller, G. C. (2004). Column experiments for microbiological treatment of acid mine drainage: Low-temperature, low-pH and matrix investigations. *Water Research*, *38*(6), 1405–1418. https://doi.org/10.1016/j.watres.2003.12.012

Tuttle, J. H., Dugan, P. R., & Randles, C. I. (1969). Microbial sulfate reduction and its potential utility as an acid mine water pollution abatement procedure. *Applied Microbiology*, *17*(2), 297–302. https://doi.org/10.1128/am.17.2.297-302.1969

Utgikar, V. P., Harmon, S. M., Chaudhary, N., Tabak, H. H., Govind, R., & Haines, J. R. (2002). Inhibition of sulfate-reducing bacteria by metal sulfide formation in bioremediation of acid mine drainage. *Environmental Toxicology*, *17*(1), 40–48. https://doi.org/10.1002/tox.10031

Verburg, R., Bezuidenhout, N., Terrence, C., & Ferguson, K. (2009). The global acid rock drainage guide (GARD guide). *Mine Water Environment*, *28*, 305–310. https://doi.org/10.1007/s10230-009-0078-4

Vrionis, H. A., Anderson, R. T., Ortiz-Bernad, I., O'Neill, K. R., Resch, C. T., Peacock, A. D., Dayvault, R., White, D. C., Long, P. E., & Lovley, D. R. (2005). Microbiological and geochemical heterogeneity in an in situ uranium bioremediation field site. *Applied and Environmental Microbiology*, *71*(10), 6308–6318. https://doi.org/10.1128/AEM.71.10.6308-6318.2005

Walters, W., Hyde, E. R., Berg-Lyons, D., Ackermann, G., Humphrey, G., Parada, A., Gilbert, J. A., Jansson, J. K., Caporaso, J. G., Fuhrman, J. A., Apprill, A., & Knight, R. (2016). Improved bacterial 16S rRNA gene (V4 and V4-5) and fungal internal transcribed spacer marker gene primers for microbial community surveys. *MSystems, 1(1)*. https://doi.org/10.1128/msystems.00009-15

Wan, M., Schröder, C., & Peiffer, S. (2017). Fe(III):S(-II) concentration ratio controls the pathway and the kinetics of pyrite formation during sulfidation of ferric hydroxides. *Geochimica et Cosmochimica Acta*, *217*, 334–348. https://doi.org/10.1016/j.gca.2017.08.036

Wang, Z., Xu, Y., Zhang, Z., & Zhang, Y. (2021). Review: acid mine drainage (AMD) in abandoned coal mines of Shanxi, China. *Water*, *13*(1). https://doi.org/10.3390/w13010008

Warner, R. W. (1971). Distribution of biota in a stream polluted by acid mine-drainage. *Ohio Journal of Science.*, *71*(4), 202–215.

Waskom, M. (2021). Seaborn: statistical data visualization. *Journal of Open Source Software*, *6*(60), 3021. https://doi.org/10.21105/joss.03021

Watson, D. B., Wu, W. M., Mehlhorn, T., Tang, G., Earles, J., Lowe, K., Gihring, T. M., Zhang, G., Phillips, J., Boyanov, M. I., Spalding, B. P., Schadt, C., Kemner, K. M., Criddle, C. S., Jardine, P. M., & Brooks, S. C. (2013). In situ bioremediation of uranium with emulsified vegetable oil as the electron donor. *Environmental Science and Technology*, *47*(12), 6440–6448. https://doi.org/10.1021/es3033555

Waybrant, K. R. (1995). *The prevention of acid mine drainage using in situ porous, reactive walls: a laboratory study* [MSc]. University of Waterloo.

Waybrant, K. R., Ptacek, C. J., & Blowes, D. W. (2002). Treatment of mine drainage using permeable reactive barriers: Column experiments. *Environmental Science and Technology*, *36*(6), 1349–1356. https://doi.org/10.1021/es010751g

Westrich, J. T., & Berner, R. A. (1984). The role of sedimentary organic matter in bacterial sulfate reduction: The G model tested. *Limnology and Oceanography*, *29*(2), 236–249. https://doi.org/10.4319/lo.1984.29.2.0236

Wilkin, R. T., & Beak, D. G. (2017). Uptake of nickel by synthetic mackinawite. *Chemical Geology*, *462*, 15–29. https://doi.org/10.1016/j.chemgeo.2017.04.023

Wilkin, R. T., & Rogers, D. A. (2010). Nickel sulfide formation at low temperature: Initial precipitates, solubility and transformation products. *Environmental Chemistry*, *7*(6), 514–523. https://doi.org/10.1071/EN10076

Williams, R. L., Mayer, K. U., Amos, R. T., Blowes, D. W., Ptacek, C. J., & Bain, J. G. (2007). Using dissolved gas analysis to investigate the performance of an organic carbon permeable reactive barrier for the treatment of mine drainage. *Applied Geochemistry*, *22*(1), 90–108. https://doi.org/10.1016/j.apgeochem.2006.09.007

Wing, B. A., & Halevy, I. (2014). Intracellular metabolite levels shape sulfur isotope fractionation during microbial sulfate respiration. *Proceedings of the National Academy of Sciences of the United States of America*, *111*(51), 18116–18125. https://doi.org/10.1073/pnas.14075021

Wu, W. M., Carley, J., Gentry, T., Ginder-Vogel, M. A., Fienen, M., Mehlhorn, T., Yan, H., Caroll, S., Pace, M. N., Nyman, J., Luo, J., Gentile, M. E., Fields, M. W., Hickey, R. F., Gu, B., Watson, D., Cirpka, O. A., Zhou, J., Fendorf, S., … Criddle, C. S. (2006). Pilot-scale in situ bioremediation of uranium in a highly contaminated aquifer. 2. Reduction of U(VI) and geochemical control of U(VI) bioavailability. *Environmental Science and Technology*, *40*(12), 3986–3995. https://doi.org/10.1021/es051960u

Zhang, P., He, Z., Van Nostrand, J. D., Qin, Y., Deng, Y., Wu, L., Tu, Q., Wang, J., Schadt, C. W., Fields, M. W., Hazen, T. C., Arkin, A. P., Stahl, D. A., & Zhou, J. (2017). Dynamic succession of groundwater sulfate-reducing communities during prolonged reduction of uranium in a contaminated aquifer. *Environmental Science and Technology*, *51*(7), 3609–3620. https://doi.org/10.1021/acs.est.6b02980

Zhang, Z., Wang, W., Qi, J., Zhang, H., Tao, F., & Zhang, R. (2019). Priming effects of soil organic matter decomposition with addition of different carbon substrates. *Journal of Soils and Sediments*, *19*(3), 1171–1178. https://doi.org/10.1007/s11368-018-2103-3

Appendix A: *Additional Data and Information Presented for Chapter 2*

A1. Monitoring Well Installations

The water table is used as a datum to measure all well and core depths because an excavator was used to remove large cobble sized clasts and road debris from above the PRB, before well installation and coring, which disturbed the ground surface. Due to an upward groundwater flow gradient within the PRB interval, coring locations were drained using a trash pump to limit contamination of the borehole with surface water. The monitoring well network is a combination of drive point piezometers, constructed out of 3.1 cm inner diameter (ID) polyvinyl chloride with 15 cm Gen Pore sintered plastic screens, and nests of screened 1.3 cm ID polyethylene (PE) tubing. Location PRB2021-8 (renamed from previous studies) is a nest of reconditioned nested wells installed as part of the original monitoring network made of 1.3 cm ID PE tubing with 15 cm slotted bottoms wrapped in 100 μm Nytex. Wyoming sodium bentonite seal chip was applied around the newly installed PRB wells to prevent infiltration of surface water after installation and reseal the original clay cap.

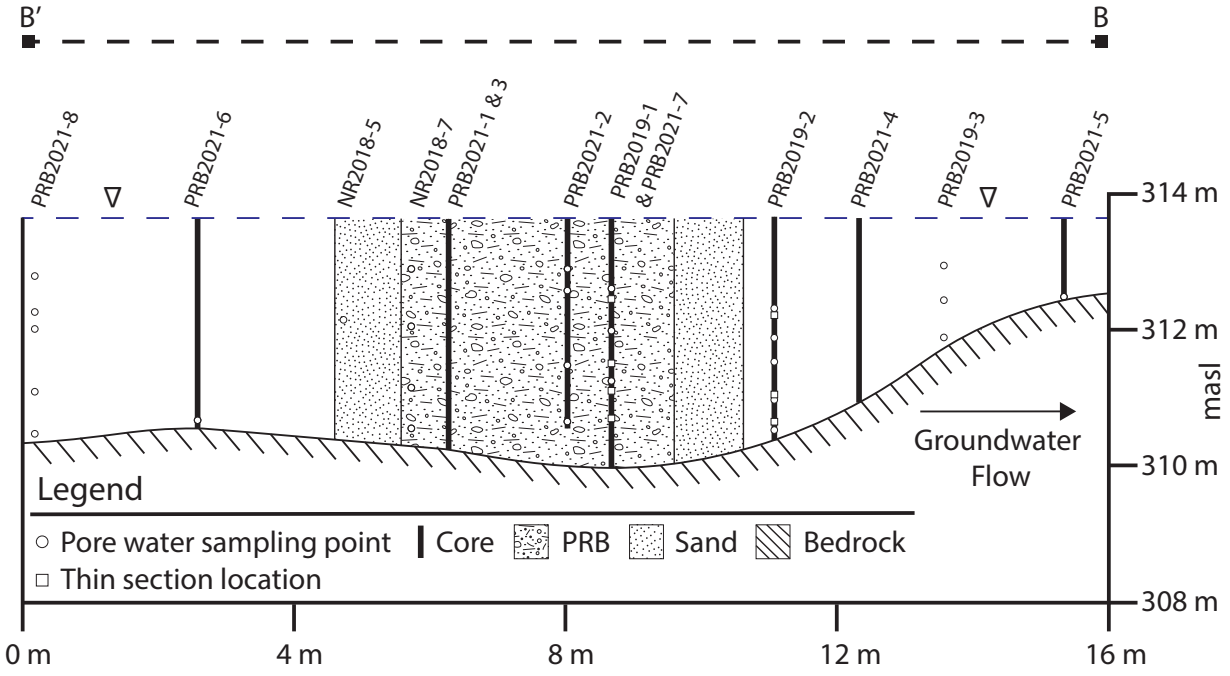


Figure A1. The B-B' cross-section transecting the PRB and illustrating the groundwater sampling and core locations. The location of the PRB and sand material was constrained by lithologic characterization of the cored material and recorded dimensions during installation. Not illustrated is the bentonite clay cover above the PRB.

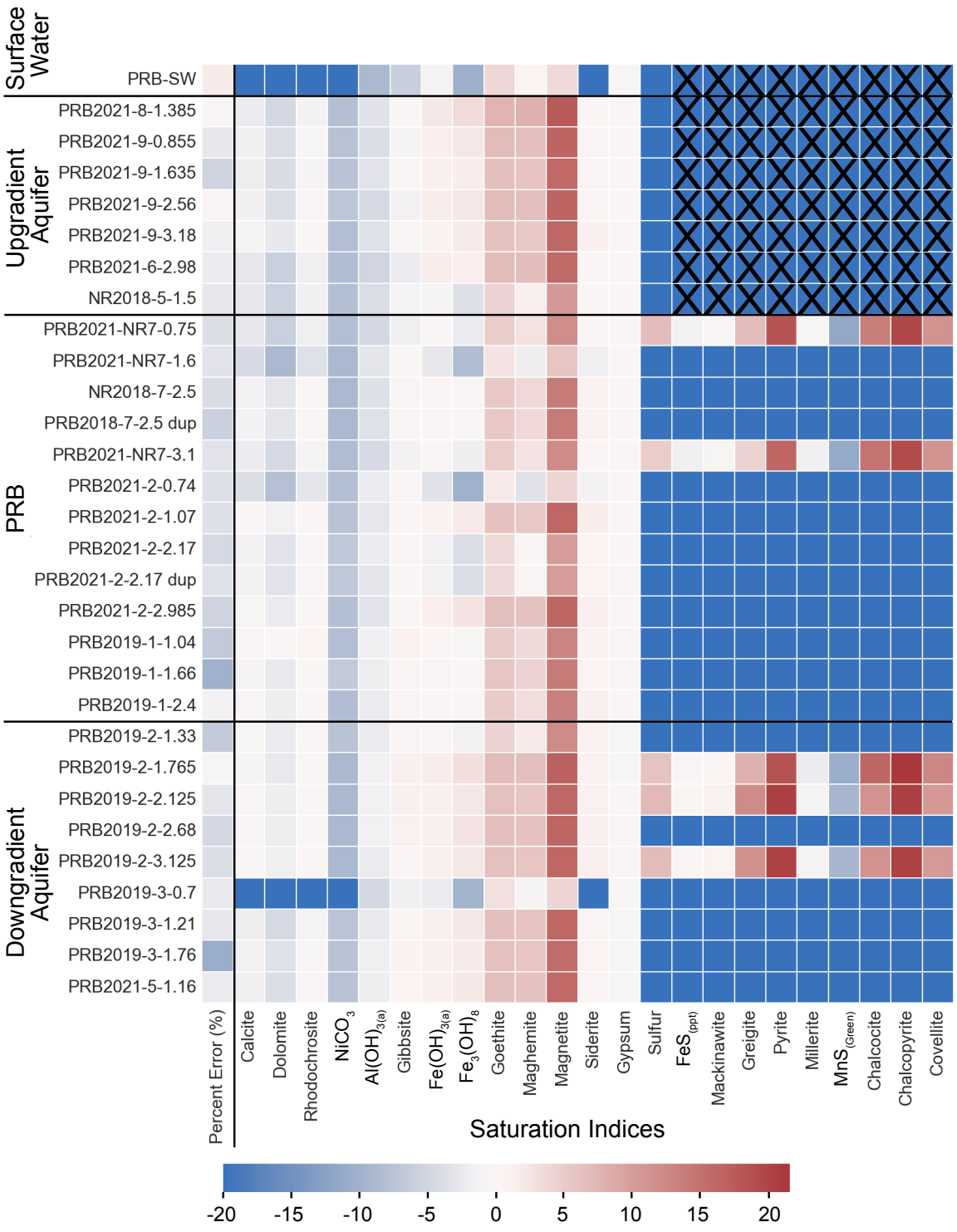


Figure A2. Heatmap of calculated charge balance percent error and saturation indices using PHREEQC and WATEQ4F database for potential reaction products. Groundwater samples are in order based on well nest location along the transect and depth in each well nest. Samples with no S^{2-} measurement are marked with an X in the sulfide species as these species are unconstrained.

A2. $BaSO_4$ Precipitation

A subset of groundwater samples were prepared at the University of Waterloo by acidification with 3N trace metal grade HCl to a pH <2 to drive off dissolved inorganic carbon before adding 20% (w/v) $BaCl_2$ solution to quantitively precipitate all SO_4 as $BaSO_4$. The $BaSO_4$ was captured on a 0.45 µm filter and rinsed with 18 MΩ H_2O to remove excess $BaCl_2$. The filter with precipitate was transferred to a watch glass and dried in a desiccator overnight. Precipitates were transferred using a clean razor blade to borosilicate glass vials that were shipped to the University of Calgary for analysis.

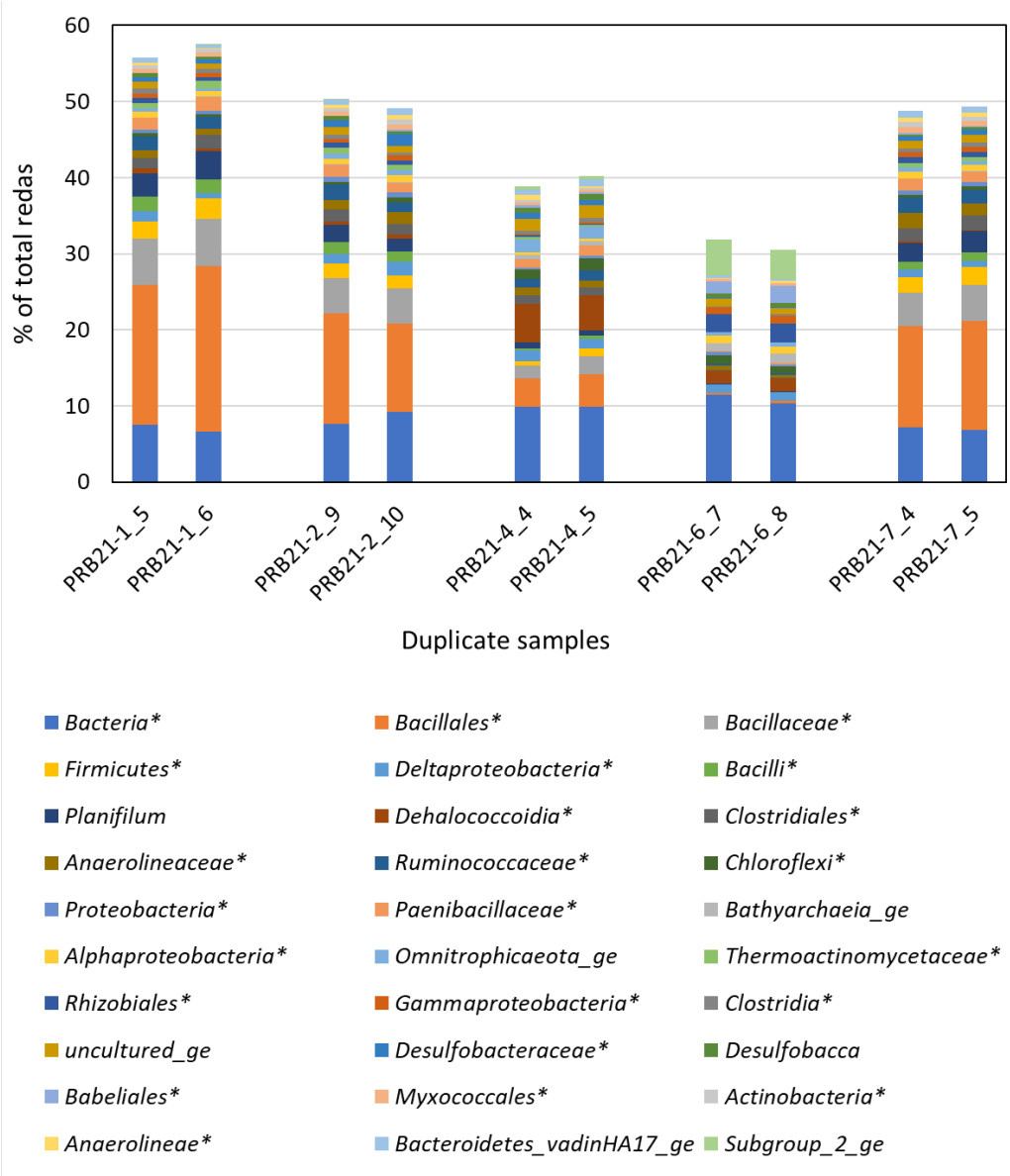


Figure A3. Proportions of total reads of major genera (relative abundance > 0.5% of total reads) in duplicate samples. Higher taxa are marked with an asterisk.

A3. Microbiology 16s rRNA amplicon sequencing statistical overview

In total 2,690,426 raw sequence reads were obtained, with an average of 68,985 ± 3,425 reads per sample (mean ± standard error; confidence level 95%). Five sets of samples were analyzed in duplicate, and due to a high level of similarity, as shown in Supplemental Figure A3, were merged before further analysis. About 29.6% of sequences were lost during quality trimming. A total effective sequence number was 1,892,180 with 55,652 ± 4,657 reads per sample, and an average of 2,177 ± 152 OTUs (97% sequence similarity) per library. Good's coverage (calculated for an OTU definition of 0.03) ranged from 90.5 to 99.4%. Sequence data statistics are summarized in Supplemental Table A1.

Table A1. Total numbers of raw and effective sequences, OTU (operational taxonomic unit) counts, and alpha-diversity indices (Good's coverage, Chao's and Gini-Simpson's indexes).

Location	Depth (m)	Total raw sequences	Effective sequences for analysis	OTU counts	Good's coverage	Chao's index	Gini-Simpson's index
PRB21-1	0.855	58,993	36,886	2,589	0.921	6,604	0.977
	1.334*	80,077	94,371	2,551	0.919	7,160	0.963
		75,545					
	1.731	115,339	71,772	2,181	0.93	5,958	0.957
	2.059	46,253	30,748	2,266	0.931	5,440	0.972
	2.335	74,652	44,664	2,956	0.905	7,856	0.968
	2.923	71,036	43,381	2,544	0.921	6,557	0.96
PRB21-2	0.548	44,913	27,283	3,054	0.908	7,403	0.978
	0.674	48,454	30,120	2,897	0.91	7,696	0.977
	1.073	58,924	35,857	2,853	0.912	7,147	0.978
	1.61*	90,358	90,427	2,644	0.921	6,632	0.983
		53,379					
	2.027	43,599	26,769	2,801	0.914	7,417	0.983
	2.36	79,292	48,676	2,730	0.916	6,747	0.978
	2.871	75,552	44,930	2,921	0.907	7,948	0.98
PRB21-4	0.685	71,745	59,673	1,053	0.982	1,484	0.952
	1.192*	68,721	122,942	2,413	0.956	3,387	0.991
		83,932					
	1.675	73,598	59,829	1,129	0.979	1,712	0.967
	1.982	59,722	44,328	2,528	0.936	4,660	0.99
	2.252	66,402	52,479	2,094	0.958	3,226	0.977
	2.494	77,061	70,006	620	0.992	986	0.966
PRB21-5	0.981	80,342	56,346	2,970	0.917	6,542	0.991
PRB21-6	0.338	99,445	84,621	433	0.993	684	0.949
	0.996	51,195	35,318	1,424	0.96	3,291	0.932
	1.185*	87,649	103,843	1,814	0.945	4,889	0.983
		67,180					
	1.459	63,002	47,105	1,399	0.966	2,701	0.985
	1.85	127,532	109,913	571	0.991	925	0.977
	2.263	42,404	35,614	416	0.994	709	0.968
	2.67	120,481	104,906	444	0.993	726	0.973
PRB21-7	0.777	30,262	20,262	2,673	0.923	6,161	0.982
	0.908	52,539	33,662	3,008	0.908	7,322	0.984
	1.29*	53,588	66,675	2,581	0.924	5,831	0.975
		50,305					
	1.839	51,548	33,852	2,820	0.912	7584	0.98
	2.462	75,539	46,017	3,129	0.906	7981	0.993
	3.052	59,555	39,563	2,818	0.917	6667	0.981
	3.455	60,313	39,342	2,709	0.921	6133	0.978

**Duplicate samples*

A4. Acid Volatile Sulfides (AVS) and Chromium Reducible Sulfur (CRS) Extractions

The AVS and CRS extraction methods were designed to evaluate the depositional conditions and diagenetic history of ocean sediment and the sedimentary rock record. These materials have orders of magnitudes less reduced S species present compared to PRB material requiring modification of the methods for use in treatment system evaluations. These methods are useful for differentiating the solid-phase S speciation. While the AVS and total reducible sulfur (TRS) definitions often focus on mineral S phases, the dissolved phases can be a major constituent especially where pore-water SO_4 concentrations are high. The extraction schemes for TRS and AVS have been tested in many investigations and shown to yield reliable and reproducible results (Canfield et al., 1986; Cornwell & Morse, 1987; Morse & Cornwell, 1987). It is important to note that these selective extractions suffer from a lack of absolute specificity in mineral separation with the potential for overlap in operational categories that are not always consistent (due to different crystallinity, sample matrix, etc.). To determine the AVS fraction a hot 6N HCl with $SnCl_2$ extraction was conducted (Rice et al., 1993). A hot extraction utilized to determine the AVS fraction is expected to result in more complete recoveries of mackinawite and greigite compared to a cold extraction (Rice et al., 1993). This was the primary justification on transitioning from the cold 6N HCl $SnCl_2$ used in the past on PRB studies (Herbert et al., 1998, 2000). Importantly, the hot extraction has the potential to dissolve some pyrite particularly if the pyrite is freshly formed and poorly crystallized (Rice et al., 1993). A modified version of the CRS method was used to measure TRS within samples (Canfield et al., 1986).

Both the AVS and CRS method utilize the same digestion apparatus described by Canfield et al. (1986). Samples were added to a reaction flask with two ports to allow for the input of N_2 gas and solutions. A glass fitting on the reaction flask was connected to a West condenser that was cooled with circulating water. Anaerobic conditions were achieved by bubbling $N_{2(g)}$ from a Pasteur pipette in one of the ports for 10-15 minutes prior to adding the extraction solutions. Extraction solutions were added with a syringe and Luer Lock on a port to maintain anaerobic conditions. The reaction flasks were heated on a stir plate to maintain near boiling temperatures and agitate the sample during extraction. N_2 and the liberated H_2S from the extraction travel through the condenser and were bubbled through a Pasteur pipette at a rate of 2-3 bubbles per second into a labelled vessel filled with 0.3 M Zn acetate with 75mL L^{-1} acetic acid trapping solution. Initially, 15 mL trapping vessels were used but determined to be insufficient to effectively trap all the H_2S from samples and the vessel volume was increased to 50 mL. The vessels were chosen to maximize bubble contact time with the solution. 0.3 M $AgNO_3$ solution was pipetted into each trapping vessel to react with the ZnS and precipitate Ag_2S at the end of the extraction time. The vessels were stored covered and in the dark after extraction runs.

The amount of S trapped as Ag_2S was quantified gravimetrically. Labelled weigh boats with 0.2 µm mixed cellulose ester filter were pre-weighed. A vacuum filter apparatus was used to filter the trapping solution and capture the precipitated Ag_2S. The precipitate was rinsed with 50 mL of DI twice, then 15 mL of 1 M ammonium hydroxide before a final 50 mL rinse of DI. The filters and precipitate were allowed to dry under ambient room conditions for 24 hours prior to being reweighed to determine the mass of Ag_2S precipitated. The mass of the sample, the sample moisture content, the weigh boat and filter mass, and the precipitate Ag_2S mass was used to calculate the dry sample S concentration in µmol g^{-1}.

The AVS extraction was conducted on material freshly thawed in the glovebox. Depending on the expected S content 0.2-4 g of wet sample was added to the reaction flasks. After establishing anaerobic conditions on the extraction line, 60 mL of 6 N HCl containing 15% (by weight) $SnCl_2$ was added and allowed to react for 2 hours with heat for complete extraction of the AVS phase. Final S concentrations were corrected for using the measured moisture content for each sample.

For the CRS extraction, sampled material was cooled to -80 C°, transferred to the freeze dryer for 24 hours and then stored anaerobically. 0.2-4 g of dried material was added to each reaction flask based on previous AVS results. After the N_2 purge, 20 mL of 6 N HCl was added followed by 40 mL of 1.0 M chromic chloride and 0.5 M HCl solution. The chromic chloride solution was reacted with Zn anaerobically during preparation and used within a week with a blue color to indicate it was still sufficiently reduced. The CRS extraction ran for 2 hours at near-boiling temperature and the reaction flash was constantly stirred.

For column experiment samples the concentration of S captured ranged from 15-325 µmol for AVS extraction step and 29-520 µmol for the CRS extraction step. A series of internal standards were used to check the extraction apparatus and the AVS and CRS extraction solutions to ensure these ranges of S released to be reliably quantified. Initially the extraction apparatus with AVS extraction solutions was tested with Na_2S standard solutions. This solution was made adding $Na_2S \bullet 9H_2O$ to 0.1 M NaOH solution, that was purged with $Ar_{(g)}$ for 30 minutes. The base solution was used to avoid degassing H_2S and changing the initial concentration. This solution was added in different volumes to the extraction vessel to test the range of S mass that could be captured. No commercial diluted FeS or pyrite standard is readily available. Laboratory standard FeS was made with floured silica sand and FeS. The FeS was prepared anaerobically with $FeSO_4 \bullet 9H_2O$ and $Na_2S \bullet 9H_2O$, filtered, and freeze dried. Some oxidation was observed in SEM-EDX analysis of the FeS attributed to freeze drying. The laboratory standard with pyrite was made with floured silica sand and commercially sourced pyrite ground to a flour. These standards were measured in replicate with the C/S analyzer to evaluate reproducibility and wt. % S. It was assumed the wt. % S was entirely composed of FeS and FeS_2 for the respective laboratory standard. Both standards were tested through the AVS and CRS methods with the recovery statistics found in **Table A2**.

Table A2. CRS and AVS standard recoveries.

	FeS Lab Standard	FeS_2 Lab Standard
Gravimetric Calculated S Concentration (µmol/g)	398	1003
Eltra C/S S Concentration		
Number of Standards Analyzed (n)	6	10
Minimum (µmol/g)	363	946
Max (µmol/g)	374	1065
Mean (µmol/g)	370	980
Standard Deviation (µmol/g)	5	33
AVS S Concentration		
Number of Standards Analyzed (n)	6	-
Minimum (µmol/g)	305	-
Max (µmol/g)	391	-
Mean (µmol/g)	343	-
Standard Deviation (µmol/g)	28	-
Mean % Recovery Compared to Mean C/S Analyzer Result	93	-
CRS S Concentration		
Number of Standards Analyzed (n)	6	13
Minimum (µmol/g)	313	846
Max (µmol/g)	386	1,121
Mean (µmol/g)	346	980
Standard Deviation (µmol/g)	28	84
Mean % Recovery Compared to Mean C/S Analyzer Result	94	100

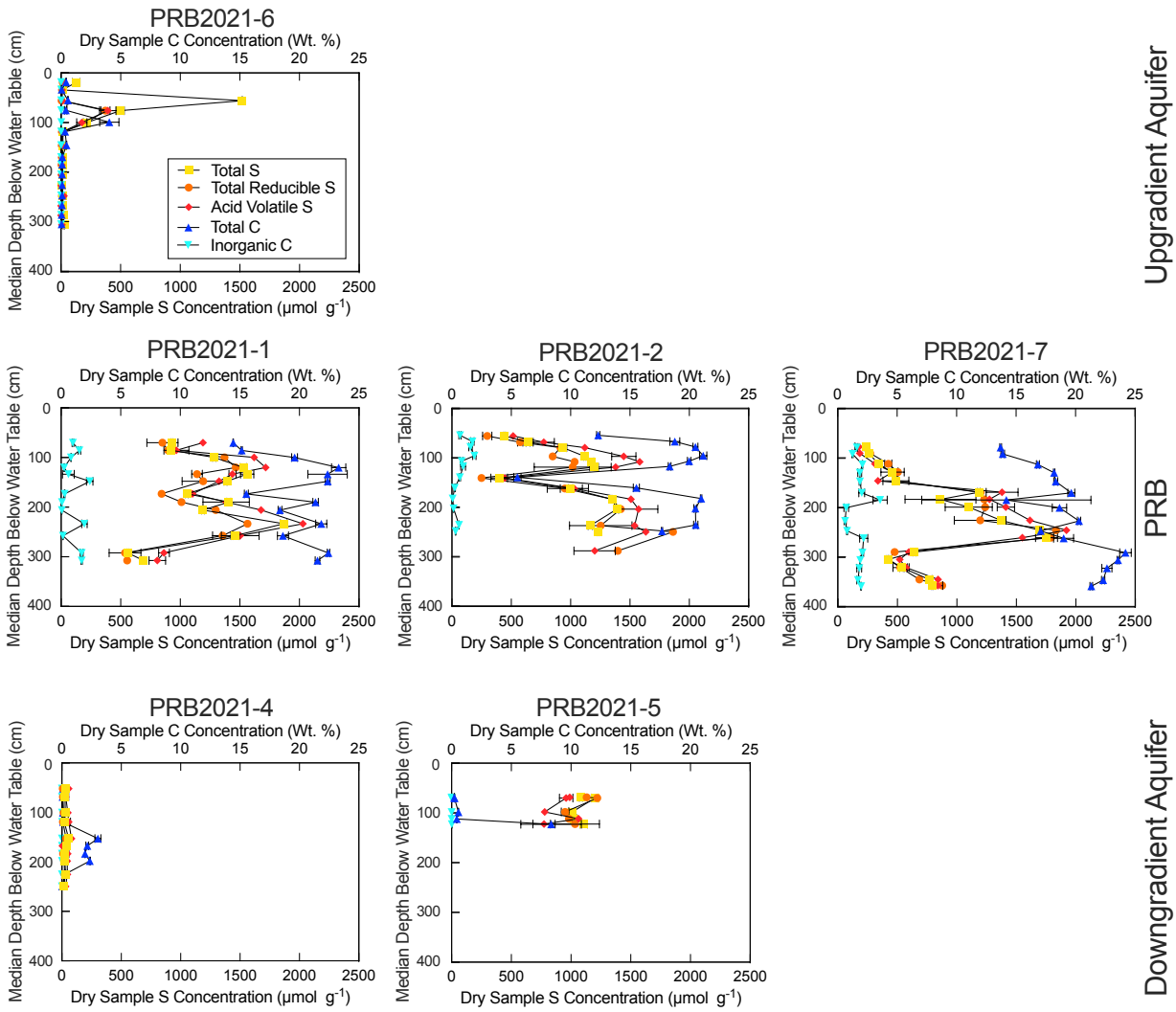


Figure A4. Total sulfur, total reducible sulfur (TRS), acid volatile sulfur (AVS) total carbon and inorganic carbon measured in sub-sampled core material from the upgradient aquifer, PRB and downgradient aquifer. Samples where more than one measurement was made for a parameter, the mean is plotted and error bars represent one standard deviation.

Table A3. Bulk removal rates for SO_4 and Fe based on aqueous concentrations and estimated residence times.

SO_4 removed (mg L^{-1} PV $^{-1}$)	Fe removed (mg L^{-1} PV $^{-1}$)	Residence time (days)	SO_4 removal rate (mg L^{-1} a^{-1})	Fe removal rate (mg L^{-1} a^{-1})	SO_4 removal rate (mmol L^{-1} a^{-1})	Fe removal rate (mmol L^{-1} a^{-1})	Ratio of SO_4: Fe
1,243[a]	402[a]	90[b]	4972	1,608	51.8	28.8	1.8 : 1

[a] Difference of mean influent (well nest PRB2021-8) and effluent (well nest PRB2019-2).

[b] Assume groundwater velocity of 16 m a^{-1} from initial estimates (Benner et al., 2002).

A5. Microbiology

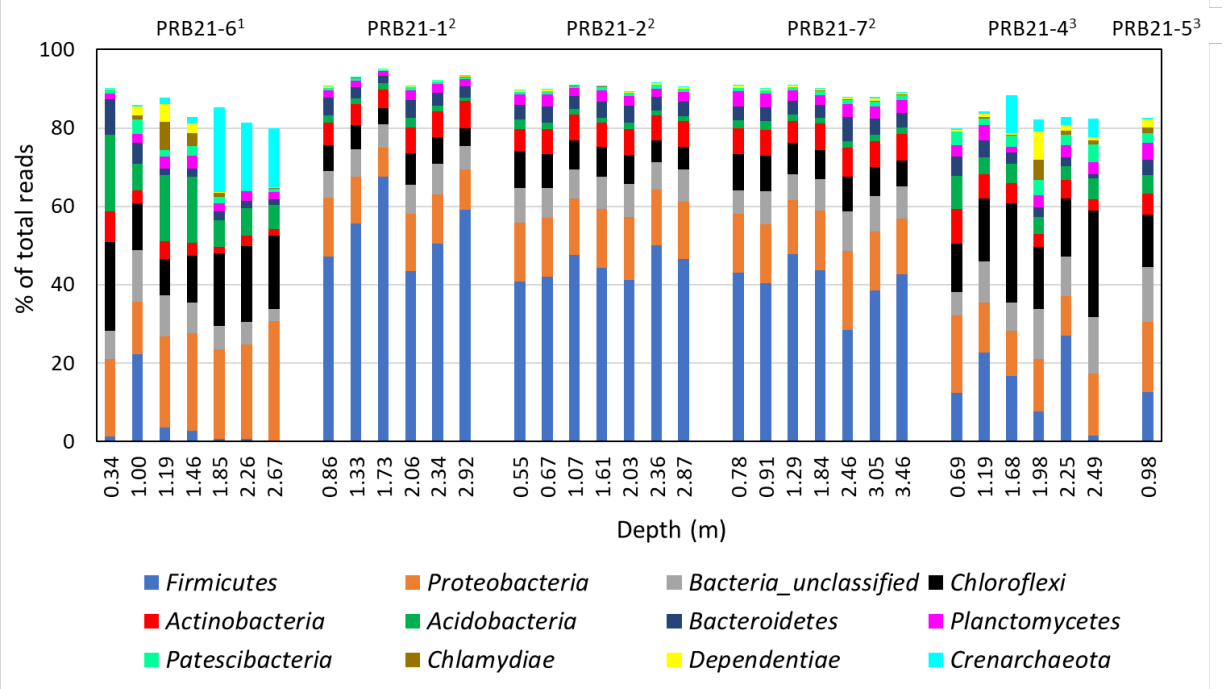


Figure A5. Proportions of total reads of major phyla (relative abundance > 1.0% of total reads). Legend: [1]upstream aquifer, [2]PRB, [3]downstream aquifer. Mean relative abundance of unclassified bacteria on the phylum level accounted for 13.3% of the total amplicons. Archaeal DNA constituted for only 2.5 % of the total amplified 16S rRNA genes.

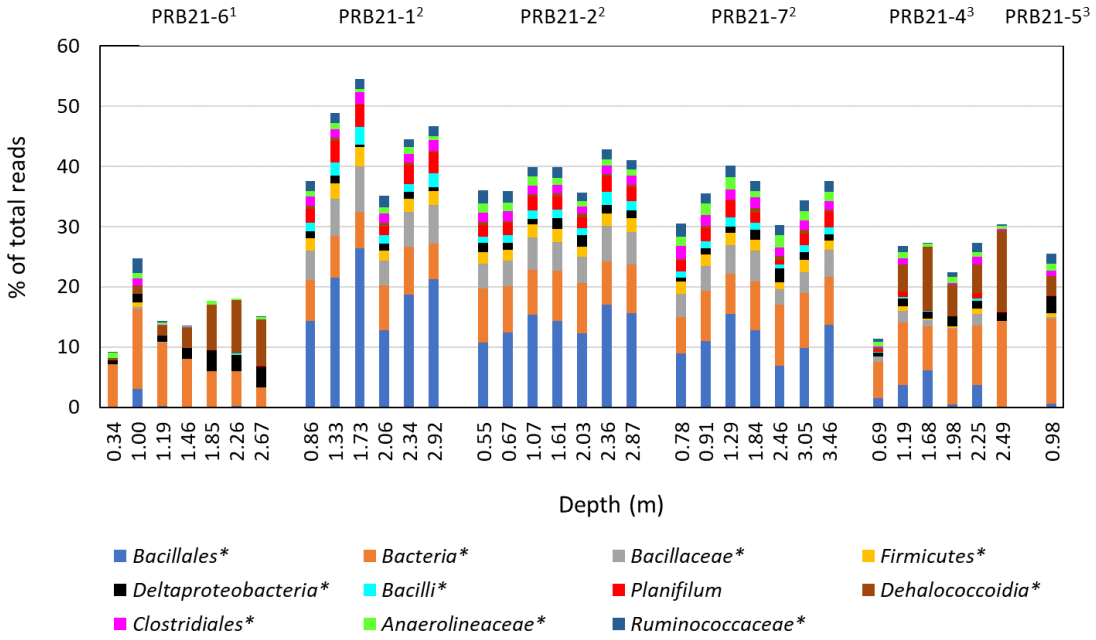


Figure A6. Proportions of total reads of major genera (relative abundance > 1.0% of total reads). Legend: [1]upstream aquifer, [2]PRB, [3]downstream aquifer. Higher taxa are marked with an asterisk when identification to the genus level was not possible.

Table A4. Mean proportions of total reads for genera of interest. Genera are separated into; sulfate reducing bacteria (SRB), sulfur- (SOP) and iron-oxidizing prokaryotes (IOP).

Genus	% of total reads in samples:			
	all	upstream aquifer	PRB	downstream aquifer
SRB:				
*Desulfobacteraceae**	0.63	0.15	0.77	0.45
Desulfobacca	0.61	1.69	0.38	1.09
*Desulfobulbaceae**	0.23	0.04	0.23	0.12
Desulfosporosinus	0.23	0.14	0.19	0.54
Desulfatiglans	0.19	0.29	0.39	0.39
Desulfomonile	0.19	0.26	0.23	0.39
*Desulfuromonadales**	0.09	<0.01	0.13	0.11
Desulfotomaculum	0.08	<0.01	0.16	0.05
Desulfitibacter	0.08	<0.01	0.14	0.03
Desulfatitalea	0.05	<0.01	0.05	0.01
Desulfurispora	0.04	<0.01	0.05	0.06
Desulfovirga	0.04	0.01	0.07	0.07
Desulfatirhabdium	0.04	0.03	0.08	0.1
Desulfoprunum	0.04	<0.01	0.07	0.01
Desulfovibrio	0.04	<0.01	0.1	0.03
Desulfitobacterium	0.03	<0.01	0.03	0.05
*Desulfobacterales**	0.03	0.01	0.02	<0.01
Dethiobacter	0.02	<0.01	0.07	0.04
*Desulfovibrionaceae**	0.02	<0.01	0.05	<0.01
Desulfonatronobacter	0.01	<0.01	0.01	<0.01
Desulfobulbaceae_ge	0.01	<0.01	0.01	<0.01
*Desulfovibrionales**	0.01	<0.01	0.01	<0.01
Desulfuromonas	0.01	<0.01	0.05	<0.01
Desulfurivibrio	0.01	0.05	<0.01	0.02
Desulfomicrobium	0.01	<0.01	0.03	<0.01
*Desulfarculaceae**	<0.01	<0.01	0.01	<0.01
Desulfatiferula	<0.01	<0.01	0.01	<0.01
Desulfobacula	<0.01	<0.01	0.02	0.01
Desulfococcus	<0.01	0.01	0.02	<0.01
Desulfobulbus	<0.01	<0.01	0.02	0.04
Desulforhabdus	<0.01	<0.01	<0.01	<0.01
Desulfuribacillus	<0.01	<0.01	<0.01	<0.01
Desulfarculus	<0.01	<0.01	<0.01	<0.01
Desulfofustis	<0.01	<0.01	<0.01	<0.01
Desulfovibrionaceae_ge	<0.01	<0.01	<0.01	<0.01
*Desulfuromonadaceae**	<0.01	<0.01	<0.01	<0.01
SOP/IOP:				
Alicyclobacillus	0.1	0.25	0.08	0.15
Acidibacillus	0.02	0.04	<0.01	0.03
*Alicyclobacillaceae**	0.02	0.04	<0.01	0.05
*Acidiferrobacteraceae**	0.01	0.01	<0.01	0.01
Acidithiobacillus	0.01	0.01	<0.01	0.01

Sulfobacillus	<0.01	<0.01	<0.01	0.01
SOP:				
Sulfurifustis	0.02	0.02	0.03	0.02
Acidiphilium	0.01	0.01	0.01	0.02
Sulfurovum	0.01	0	0.02	<0.01
Sulfuriferula	0.01	0.02	<0.01	0.02
Acidicaldus	0.01	<0.01	0.01	0.01
Thiomonas	0.01	<0.01	<0.01	0.01
Sulfuricella	<0.01	0.03	<0.01	0.02
Sulfuricurvum	<0.01	<0.01	<0.01	<0.01
Sulfurimonas	<0.01	<0.01	<0.01	<0.01
Thiobacillus	<0.01	<0.01	<0.01	<0.01
IOP:				
*Acidimicrobiia**	0.17	0.12	0.07	0.13
*Gallionellaceae**	0.09	0.26	<0.01	0.02
Ferrovibrio	0.01	<0.01	0.04	0.01
Leptospirillum	0.01	0.01	<0.01	0.03
Ferrithrix	0.01	0.01	<0.01	0.03
Acidithrix	0.01	<0.01	<0.01	0.01
Gallionella	<0.01	<0.01	<0.01	0.02
Ferrovum	<0.01	<0.01	<0.01	0.01
Ferritrophicum	<0.01	<0.01	<0.01	<0.01

Table A5. Total reducible sulfur (TRS) bulk accumulation rates.

Location	Source	Core	Time (months)	Time (a)	Average TRS (µmol g^{-1} S)[a]	Dry Bulk Density (g cm^{-3})	Average TRS Accumulation Rate (µmol cm^{-3} a^{-1})[b]
Upgradient PRB	Herbert et al., 1998	Core 9511	3	0.3	58.2	0.27[c]	63
	Herbert et al., 1998	Core 9610	14	1.2	112.6	0.27[c]	26
	Herbert et al., 1998, 2000	Core 9707-6	23	1.9	160.6	0.27[c]	23
	Eugnie Daignault BSc Thesis (unpublished)	NRW29-C	71	5.9	168.3	0.27[c]	8
	This study	PRB2021-1	314	26.2	1,083.3	0.41	17
Middle PRB	Herbert et al., 2000	Core 9707-7	23	1.9	93.0	0.27[c]	13
	Eugenie Daignault BSc Thesis (unpublished)	NRW30-C	71	5.9	229.0	0.27[c]	10
	This study	PRB2021-2	314	26.2	1,013.6	0.48	19
Downgradient PRB	Herbert et al., 1998	Core 9707-8	23	1.9	119.3	0.27[c]	17
	Eugenie Daignault BSc Thesis (unpublished)	NRW31-C	71	5.9	268.0	0.27[c]	12
	This study	PRB2021-7	214	17.8	838.0	0.27	13

[a] Average of the average TRS at each sampling depth

[b] Average TRS x Bulk Density / Time

[c] Bulk density from Herbert et al., 2000

Table A6. Bulk S K-edge XANES Linear Combination Fitting.

Core	Median Sample Depth Below Water Table (m)	Sample ID	χ^2	χ^2 Reduced	FeS	Cysteine	Ferrous Sulfate	Na-Sulfite	Pyrite	Elemental S	Na-Thiosulfate	Gypsum	K-Tetrathionate	Total
PRB21-1	1.2	PRB21-1-4	0.30	0.001	68%	21%	5%	0%	0%	4%	0%	3%	0%	100%
PRB21-1	2.92	PRB21-1-14	0.29	0.001	73%	16%	9%	0%	0%	0%	0%	2%	0%	100%
PRB21-2	0.96	PRB21-2-5	0.55	0.002	88%	6%	1%	1%	0%	0%	0%	3%	0%	100%
PRB21-2	2.49	PRB21-2-14	0.42	0.002	91%	5%	1%	1%	0%	0%	0%	1%	0%	100%
PRB21-7	1.69	PRB21-7-7	0.42	0.002	91%	5%	1%	1%	0%	0%	0%	1%	0%	100%
PRB21-7	2.9	PRB21-7-14	0.53	0.002	77%	14%	8%	1%	0%	0%	0%	0%	0%	100%

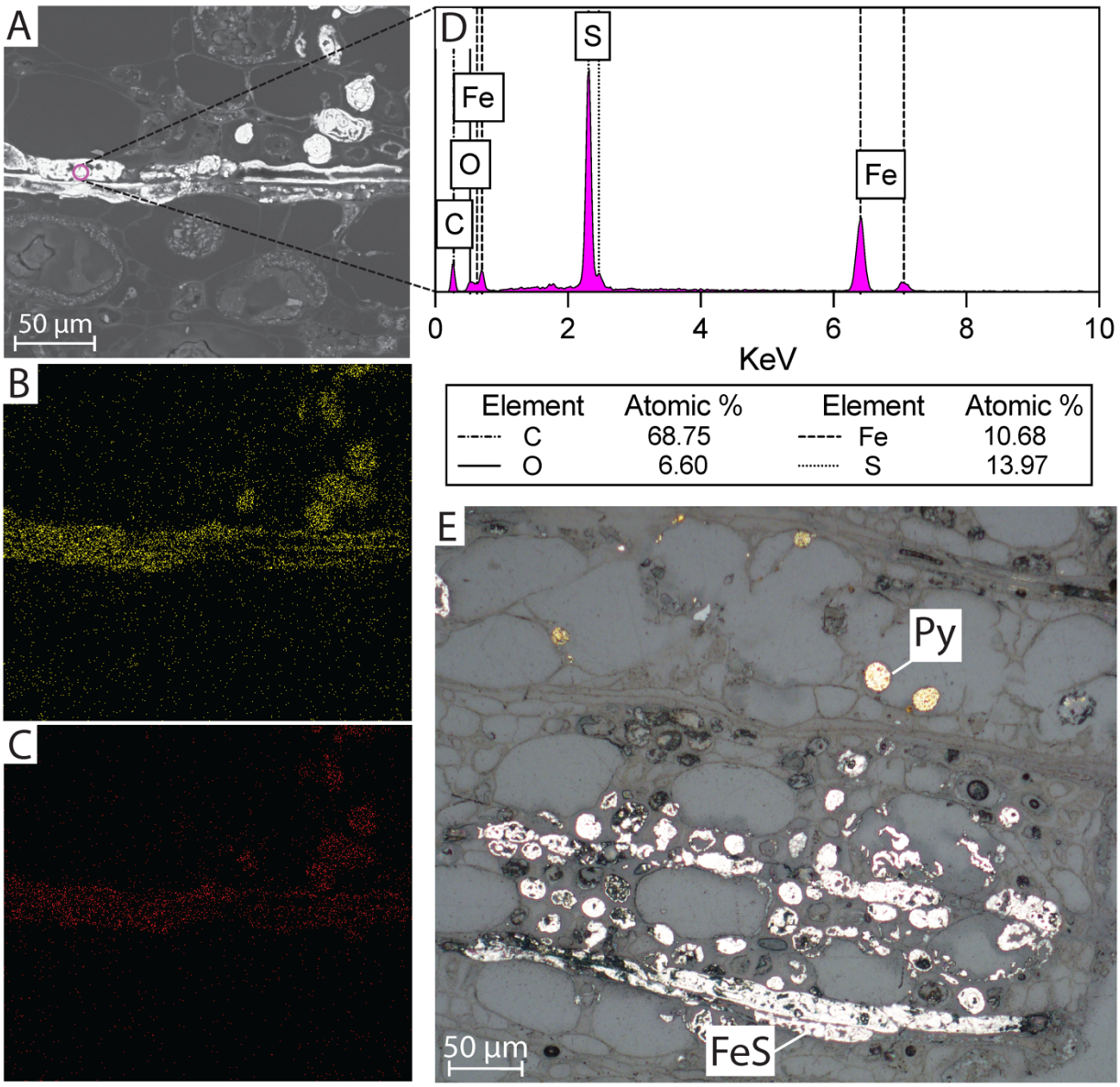


Figure A7. Optical mineralogy and SEM of organic material. A) backscatter image of organic carbon material with reflective region along plant cell wall; B) elemental map of S in this region showing accumulation in plant cell wall and nodules likely indicative of pyrite framboids; C) elemental map of Fe showing accumulation along plant cell wall and nodules; D) SEM-EDX spectrum from a location along plant cell wall, and E) Pictomicrograph showing distribution of FeS phases concentrated along plant cell walls and pyrite framboids within organic material in a similar location.

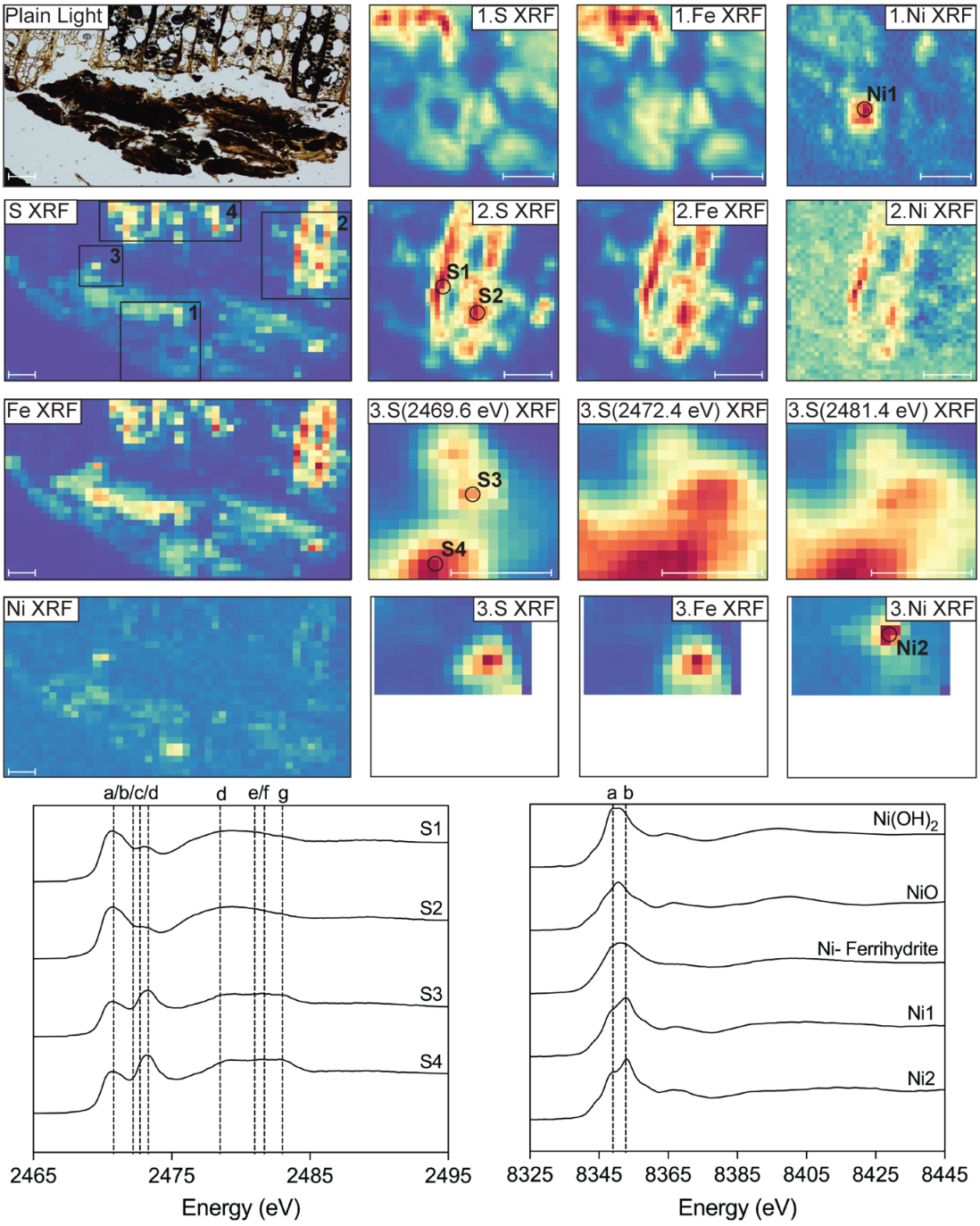


Figure A8. Location of interest examined with XRF maps at SXRMB and S and Ni K-edge μXANES spectra. Elemental heat maps are shown with three zoomed in regions indicating hotspots and locations where S and Ni μXANES spectra were collected. The S and Ni μXANES spectra are shown in the left and right below. Vertical lines in the S μXANES correspond to standards in Figure 2.6 A. Ni standards used in LCF fitting are shown. Region 3 had S phases mapped at different energies and full elemental maps developed for only a portion of the region.

Table A7. Linear combination fitting of S K-edge μXANES of samples collected.

Location	χ^2	χ^2 Reduced	Gypsum	FeS	Cysteine	Na-Sulfite	Ferrous Sulfate	Pyrite	Elemental S	K-Tetrathionate	Na-Thiosulfate	Total
S1	0.651	0.002	4%	91%	0%	2%	0%	0%	0%	0%	2%	100%
S2	0.901	0.003	4%	91%	0%	3%	0%	0%	0%	0%	3%	100%

Note: LCF attempted on S3 and S4. XANES could not be flattened to allow for LCF fitting due to organosulfur phases.

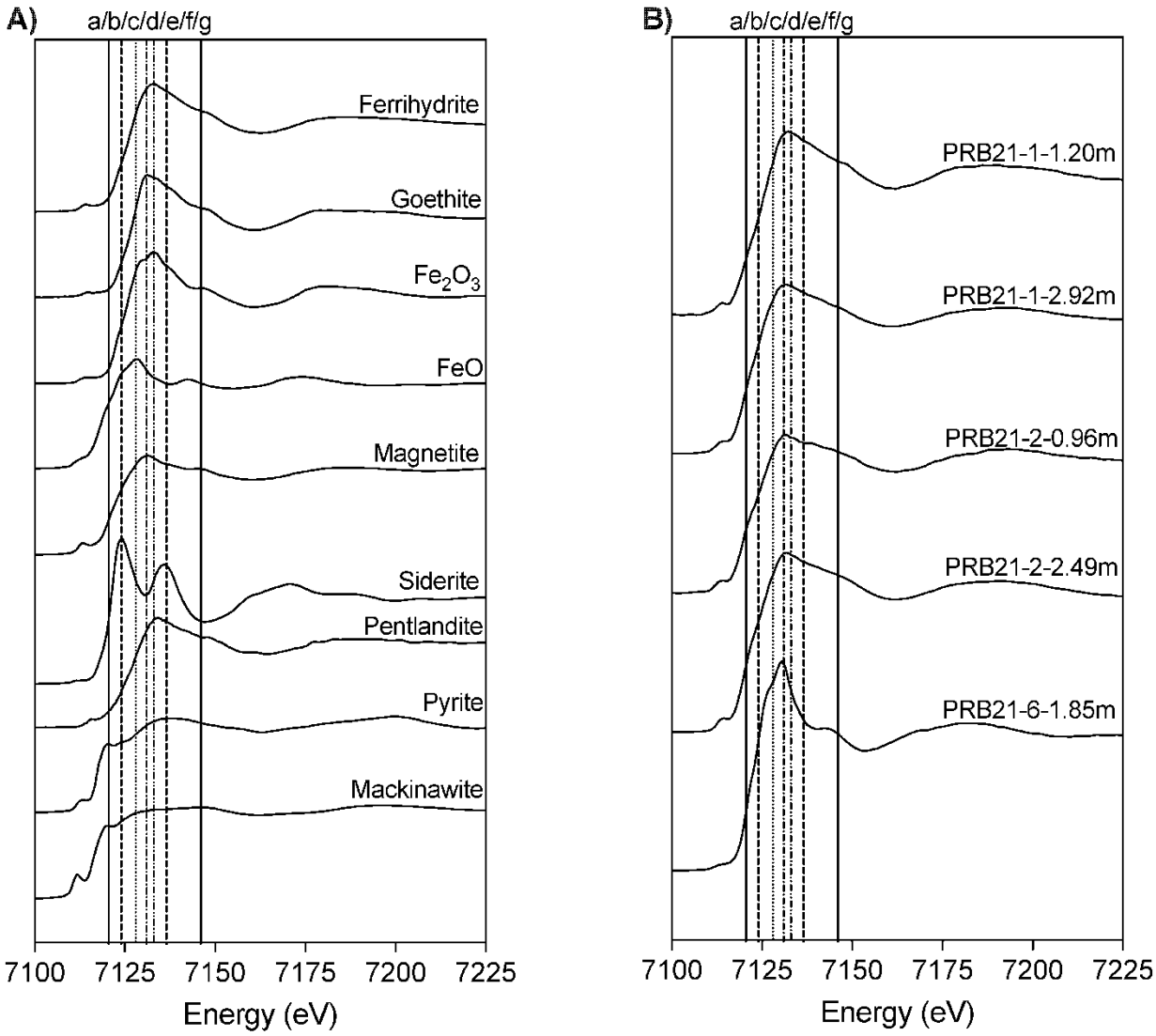


Figure A9. Bulk Fe K-edge XANES. Standard spectra used for LCF are illustrated on the left (A) with vertical lines identifying for prominent peaks in these standards. Sample spectra are illustrated on the right (B) with the same vertical lines to allow for fingerprinting.

Table A8. Bulk Fe K-edge XANES Linear Combination Fitting on sampled material from the PRB an downgradient aquifer.

Core	Median Sample Depth Below Water Table (m)	Sample ID	χ^2	χ^2 Reduced	Mackinawite	Pyrite	Pentlandite	Siderite	Magnetite	FeO	Fe_2O_3	Ferrihydrite	Goethite	Total
PRB21-1	1.2	PRB21-1-4	0.07	0.0003	0%	14%	0%	3%	0%	18%	0%	47%	17%	100%
PRB21-1	2.92	PRB21-1-14	0.07	0.0003	0%	14%	0%	3%	0%	18%	0%	47%	17%	100%
PRB21-2	0.96	PRB21-2-5	0.13	0.0005	0%	10%	17%	0%	66%	4%	0%	0%	4%	100%
PRB21-2	2.49	PRB21-2-14	0.16	0.0006	0%	11%	0%	4%	6%	27%	0%	52%	0%	100%
PRB21-6	1.85	PRB21-6-11	1.01	0.0039	0%	0%	0%	8%	0%	40%	48%	0%	5%	100%

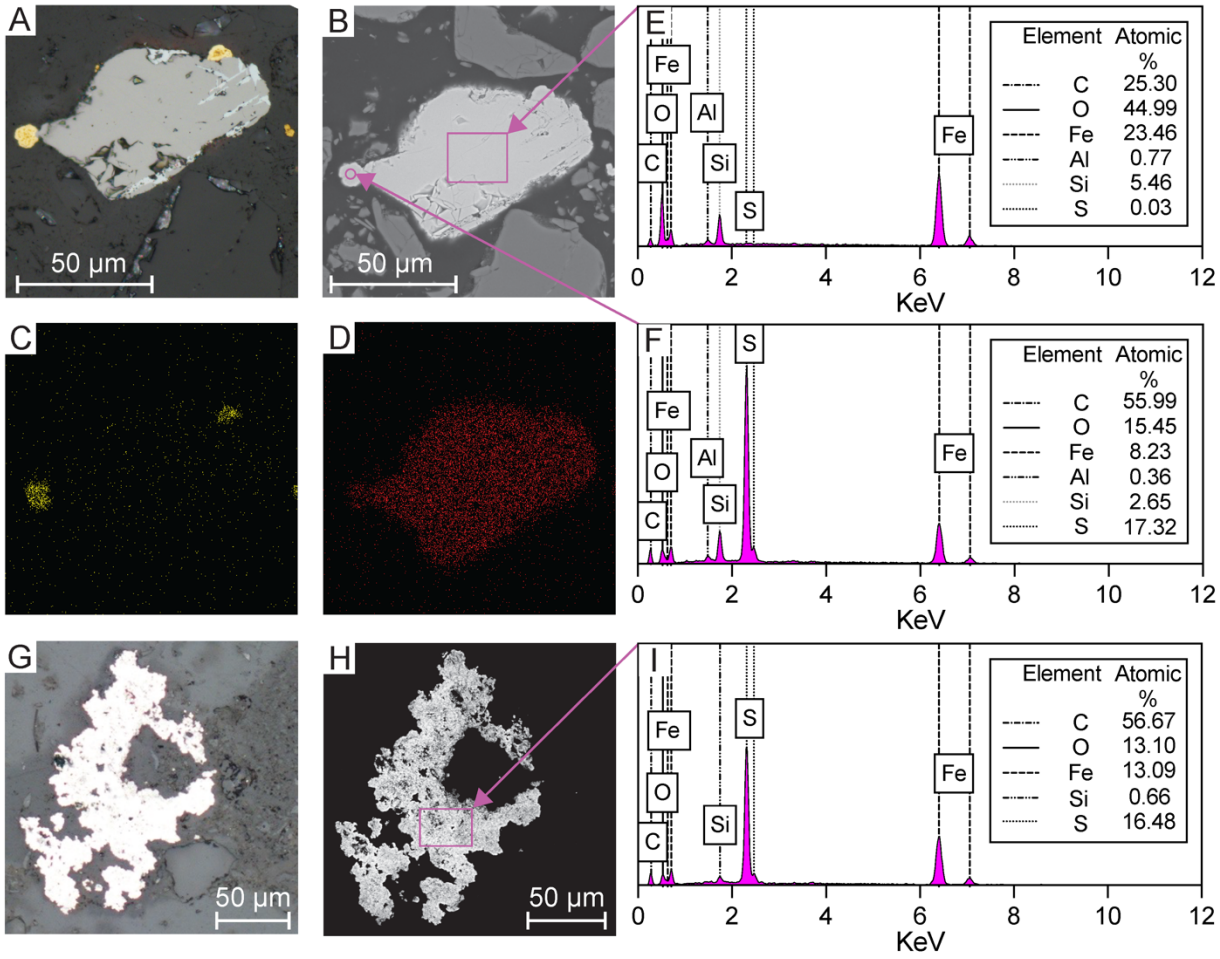


Figure A10. Optical mineralogy and SEM-EDX of S and Fe phases identified. Pictomicrograph (A) and backscatter image (B) illustrating the relationship between pyrite and an Fe-oxide phase as identified by EDX analysis (Fe-oxide phase (E) & pyrite phase (F)). Elemental maps of this same location are shown for S (C) and Fe (D). Below is a picotomicrograph (G) and backscatter image (H) of another location where FeS is present within the extracellular matrix in close association with organic carbon material. The elemental composition was confirmed with EDX (I).

Table A9. Ni K-edge μXANES LCF fittings of locations shown in figure A8.

Core	Median Sample Depth Below Water Table (m)	Location	χ^2	χ^2 Reduced	Millerite	$Ni(OH)_2$	$NiSO_4$	Ni Foil	NiO	NiS	NiS_2	Ni Sorbed to Ferrihydrite	Total
PRB2019-2	1.44	Hotspot 1	0.861	0.004	0%	12%	0%	0%	0%	0%	0%	88%	100%
PRB2019-2	1.44	Hotspot 2	1.888	0.009	0%	0%	0%	0%	9%	0%	0%	91%	100%

Appendix B: *Additional Data and Information Presented for Chapter 3*

Table B1. Mean moisture content of the reactive material components measured in triplicate.

< 3/8" Leaf Compost	< 3/8" Wood Chips	Silica Sand	Limestone
(Wt. %)	(Wt. %)	(Wt. %)	(Wt. %)
41	39	0.03	0.03

B1. pH and Eh measurement and calibration

The pH probe was calibrated using fresh pH 4, 7 and 10 buffers to start an influent, effluent and pore-water sampling event. Re-calibration occurred if the buffer 7 solution used as an initial calibration verification and as a continuing calibration verification came back >0.02 pH units from the temperature adjusted value or the Nerst slope was < 95% or > 102%. An Orion 3 Star meter with Orion 9678 BN redox electrode with Orion 900001 filling solution was used for measured potential. The probe response was checked daily with Zobell (D. K. Nordstrom, 1977) and Light's (Light, 1972) solution with the probe sensitivity confirmed with solution A and B. The redox electrode was changed to a VWR Symphony combination epoxy redox electrode at week 28 due to aberrant values when measuring daily standards and was used for the remaining duration of the study. Sample was dispensed into test tubes and both pH and Eh probes were conditioned with fresh sample prior to taking measurements. Samples were gently agitated and measurements were recorded every 2-4 minutes until stability was achieved or 15-30 minutes of measurement. Multiple refills of sample were measured to confirm results when volume was not limited. Both probes were submerged in DI adjusted to pH <2 with HCl, rinsed with deionized water and blotted dry before proceeding to the next measurement.

B2. $BaSO_4$ Precipitation

At the University of Waterloo, samples were prepared by acidification with 3 N trace metal grade (TMG) HCl to a pH <2 to drive off DIC before adding 20% (w/v) $BaCl_2$ solution to quantitively precipitate all SO_4 as $BaSO_4$. The $BaSO_4$ was collected on a 0.45 µm filter and rinsed with 18 MΩ H_2O to remove excess $BaCl_2$. The filter with precipitate was transferred to a watch glass and dried in a desiccator overnight. The precipitate was transferred using a clean razor blade to a borosilicate glass vial that were shipped to the University of Calgary for analysis.

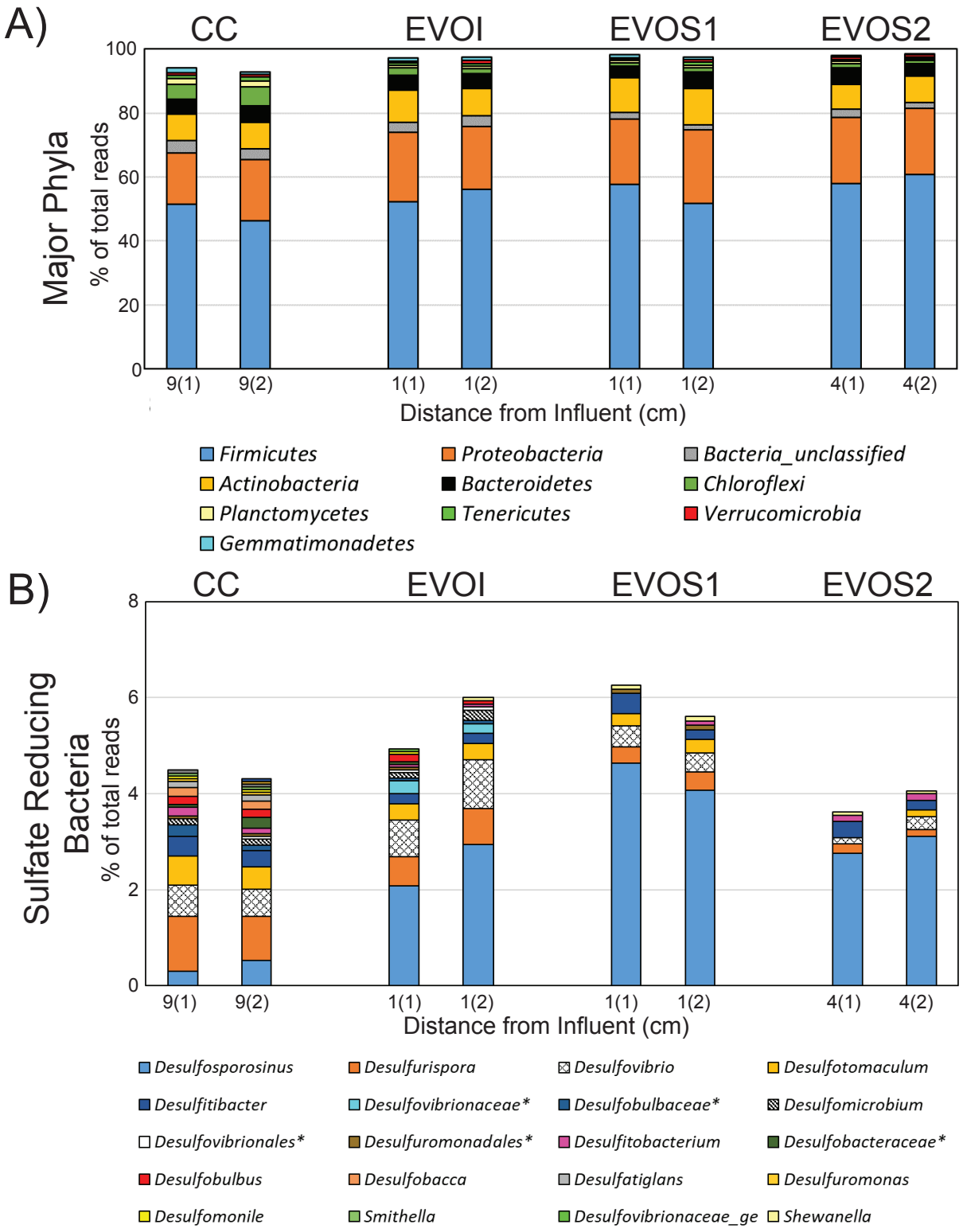


Figure B1. A) Comparison of major phyla in duplicate samples from each column (relative abundance > 0.5 % of total reads). B) comparison of sulfate reducing bacteria total reads in duplicate samples from each column.

B3. Overview of 16S rRNA gene sequence data statistics

In total 841,417 raw sequence reads were obtained, with an average of 23,373 ± 1,296 reads per sample (mean ± standard error; confidence level 95 %). About 5.68 % of sequences were flagged as chimeric and 26.25 % was lost to quality trimming. A total effective sequence number was 572,712 with 15,909 ± 1,307 reads per sample, and an average of 988 ± 61 OTUs (97 % sequence similarity) per library. Good's coverage (calculated for an OTU definition of 0.03) ranged from 89.0 to 96.6 %. Archaeal DNA constituted for only 0.3 % of total amplified 16S rRNA genes. Sequence data statistics are summarized in **Table B2**.

Table B2. Total numbers of raw and effective sequences, operational taxonomic unit (OTU).

Column	Sample Column Height (cm)	Total Raw Sequences	Effective Sequences for Analysis	OTU Counts	Good's Coverage	Chao's Index	Gini-Simpson's Index
CC	1.3	14,265	15,327	1,048	0.934	1,976.9	0.986
	3.8	19,503	11,975	1,224	0.922	2,352.9	0.986
	6.3	16,462	12,094	1,260	0.914	2,749.8	0.984
	8.8*	20,774	16,250	1,160	0.92	2,438.5	0.979
	8.8*	21,081	17,330	1,157	0.926	2,375.0	0.98
	11.3	16,070	12,527	1,045	0.93	2,195.0	0.958
	16.3	14,077	11,447	1,161	0.924	2,364.7	0.982
	23.8	18,925	14,624	1,079	0.929	2,104.5	0.979
	33.8	16,302	11,743	1,433	0.896	3,472.6	0.978
EVOI	1.3*	26,383	19,190	1,114	0.92	2,581.0	0.966
	1.3*	16,278	11,132	1,189	0.912	2,814.6	0.965
	3.8	17,226	11,959	1,105	0.917	2,690.9	0.953
	6.3	13,341	8,830	1,426	0.89	3,617.6	0.98
	8.8	25,392	18,399	1,076	0.923	2,456.3	0.968
	11.3	16,952	12,688	1,393	0.903	3,041.3	0.986
	16.3	28,863	21,239	1,304	0.913	2,714.2	0.987
	23.8	11,187	8,227	1,302	0.905	3,219.9	0.962
	33.8	21,914	14,991	1,460	0.895	3,411.0	0.985
EVOS1	1.3*	42,764	36,904	509	0.965	1,002.5	0.673
	1.3*	40,106	35,502	470	0.966	1,124.3	0.617
	3.8	26,842	20,252	842	0.938	1,956.5	0.864
	6.3	17,476	12,173	1,051	0.919	2,665.3	0.929
	8.8	26,672	20,306	901	0.937	2,102.7	0.955
	11.3	28,950	2,399	61	0.645	136.3	0.93
	16.3	17,540	12,109	1,123	0.921	2,549.0	0.973
	23.8	22,981	16,507	928	0.935	2,132.9	0.965
	33.8	17,171	11,636	1,203	0.91	3,025.6	0.979
EVOS2	1.3	22,720	18,115	556	0.958	1,406.4	0.567
	3.8*	25,756	18,580	971	0.932	2,139.1	0.945
	3.8*	28,571	21,544	871	0.938	1,905.3	0.942
	6.3	29,166	1,384	65	0.628	141.2	0.956
	8.8	27,559	121	71	0.537	225.0	0.956
	11.3	27,896	20,508	1,003	0.935	1,974.7	0.973
	16.3	35,400	25,659	1,011	0.931	2,260.2	0.982
	23.8	31,925	22,977	988	0.932	2,245.8	0.98
	33.8	36,927	26,064	1,014	0.931	2,185.5	0.977

**Duplicate samples*

B4. Stanmod and CXTFIT modeling

The effluent bromide concentration data was fit with both the deterministic equilibrium convection dispersion equation (CDE) transport model and the deterministic nonequilibrium CDE two-region transport model using CXTFIT code (Toride et al., 1995) and STANMOD computer software (Simunek et al., 1999). The equilibrium CDE model was chosen due to a lack of improved fit using the nonequilibrium CDE two-region model. Initial condition for the column was:

$$C_r(0.5\ mg\ L^{-1}, 0) = C_i(0.5\ mg\ L^{-1})$$

Where the initial concentration C_i was constant and set as half the lower detection limit for Br. There was no production, and a Dirichlet multiple input pulse condition was used based on influent batch Br concentrations measured. The model was run with the retardation factor fixed at 1 and no decay.

Table B3. Sulfur XANES liner combination fitting results.

Sample	Column	Depth (cm)	χ^2	χ^2 Reduced	Gypsum	Ferrous Sulfate	K-Tetrathionate	Na-Sulfite	Na-Thiosulfate	Cysteine	Elemental S	Pyrite	FeS	Total
CC-S2	CC	4	8.75	0.0297	0%	43%	0%	0%	0%	13%	0%	7%	37%	100%
CC-S7	CC	24	5.27	0.0179	15%	31%	0%	0%	0%	16%	3%	0%	35%	100%
EVOI-S2	EVOI	4	1.70	0.0057	17%	0%	0%	0%	0%	0%	0%	2%	82%	100%
EVOI-S7	EVOI	24	5.22	0.0178	4%	32%	0%	0%	0%	16%	2%	0%	46%	100%
EVOS1-S2	EVOS1	4	4.79	0.0162	0%	0%	0%	2%	13%	0%	0%	14%	71%	100%
EVOS1-S7	EVOS1	24	7.92	0.0269	0%	29%	3%	0%	5%	36%	0%	0%	27%	100%
EVOS2-S2	EVOS2	4	0.82	0.0028	36%	4%	0%	1%	3%	0%	0%	9%	47%	100%
EVOS2-S7	EVOS2	24	0.99	0.0034	26%	14%	0%	0%	0%	13%	3%	0%	44%	100%

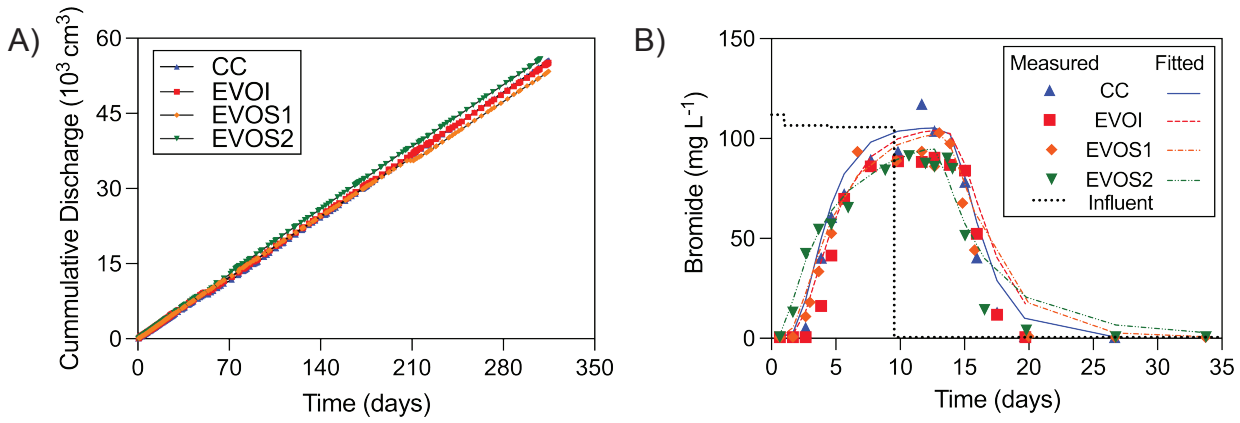


Figure B2. A) Cumulative discharge for each column measured gravimetrically over the experiment duration. B) measured Br tracer test breakthrough curves and influent concentrations for each column along with CXTFIT modeled results.

Table B4. Column experiment duration, flow parameters, and gravimetric pore volume measurements.

Column	Experiment Run Time	Cumulative Discharge	Average Flow Rate	Pore Volume Gravimetric
	(d)	10^3 cm^3	(mL h^{-1})	(mL)
CC	315	57.1	7.6	723
EVOI	315	56.9	7.5	811
EVOS1	315	54.7	7.2	649
EVOS2	309	57.2	7.7	635

Table B5. CXTFIT modeling fits *vs.* observed values and calculated pore-water velocity, pore volume, porosity, residence time, and total pore volumes.

Column	CXTFIT R^2 for Regression of Observed *vs.* Predicted	Pore Water Velocity	Dispersion	Pore Volume CXTFIT	Porosity	Residence Time	Total Pore Volumes
	(-)	(cm d^{-1})	(cm^2 d^{-1})	(mL)	(-)	(d)	(-)
CC	0.94	8.9	40.8	804	0.39	4.4	71.1
EVOI	0.86	7.4	37.4	972	0.45	5.4	58.6
EVOS1	0.94	7.8	65.4	960	0.35	5.5	57.0
EVOS2	0.93	7.1	159.8	1084	0.34	5.8	52.8

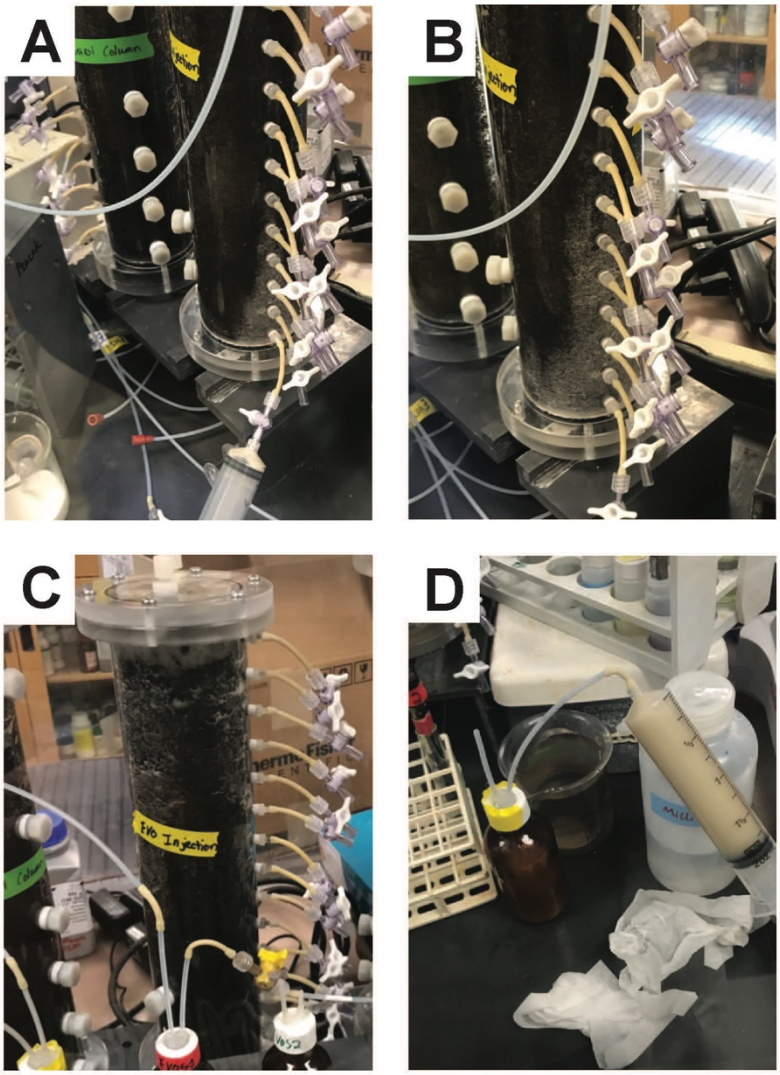


Figure B3. A) EVOI column after 50 ml EVO-influent mixture injected at beginning of the experiment. B) EVOI column after 100 ml EVO-influent mixture injected at the beginning of the experiment. Note the preferential flow through the column. C) Rapid migration of EVO to the upper portion of the EVOI column ~12 hours after injection. D) The EVOI effluent sample collection vessel with EVO clearly in the effluent after 1 day.

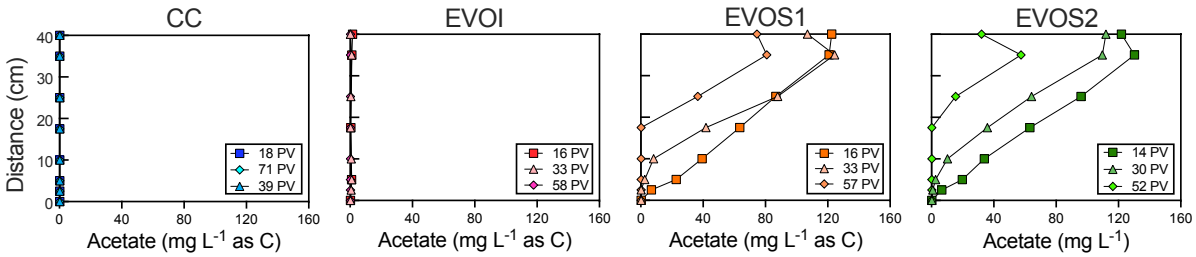


Figure B4. Column profile acetate concentrations. The sampling events for each column, labeled according to the approximate PV during sampling, are differentiated by both color shade and shape. Distance 0 cm represents the influent and 40 cm represents the effluent.

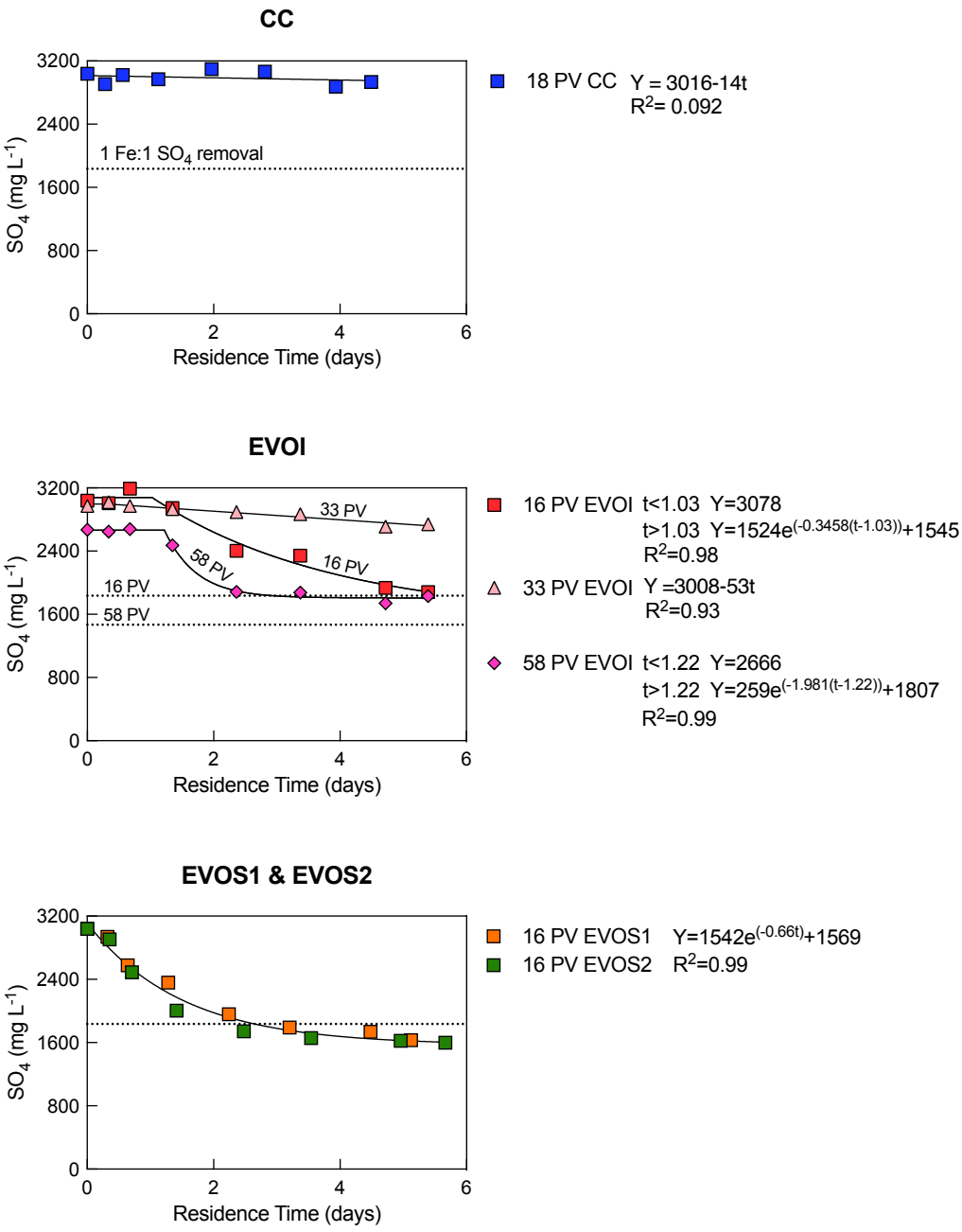


Figure B5. Profile sampling event pore-water SO_4 *vs.* residence time (t). These results were fit with different types of models to determine bulk SO_4 removal rates. The coefficient of determination describes (R^2) the fit of each model.

Table B6. Mean proportions of total reads of sulfate reducing bacteria in each test condition. EVOS1 and EVOS2 are combined into EVOS.

Taxon	% of total reads in:			
	all samples	CC	EVOI	EVOS
Desulfosporosinus	1.93	0.36	1.39	2.4
Desulfurispora	0.85	0.99	1.21	0.12
*Desulfovibrionales**	0.61	0.84	0.88	0.37
Desulfotomaculum	0.36	0.53	0.57	0.13
Desulfitibacter	0.3	0.41	0.39	0.26
*Desulfobulbaceae**	0.13	0.21	0.14	0.06
Desulfomicrobium	0.09	0.19	0.18	0.05
*Desulfuromonadales**	0.08	0.16	0.15	0.02
Desulfitobacterium	0.06	0.13	0.11	0.08
*Desulfobacterales**	0.05	0.15	0.15	0.01
Desulfobacca	0.03	0.16	0.08	0
Smithella	0.03	0.04	0.04	0.01
Desulfatiglans	0.02	0.09	0.02	0.01
Shewanella	0.02	0.01	0.04	0.06
Desulfoprunum	0.01	0.07	0.04	0
Desulfomonile	0.01	0.06	0.05	0
Desulfonatronobacter	0.01	0	0	0
Desulfuromusa	0.01	0.02	0.02	0

** Higher taxa that could not be identified at the genus level.*

Table B7. Column moisture content summary statistics.

Column	Count	Moisture Content Mean (%)	Moisture Content Standard Deviation (%)
CC	10	26.2	1.8
EVOI	10	27	1.4
EVOS1	10	24.5	1.5
EVOS2	10	24.7	1.1

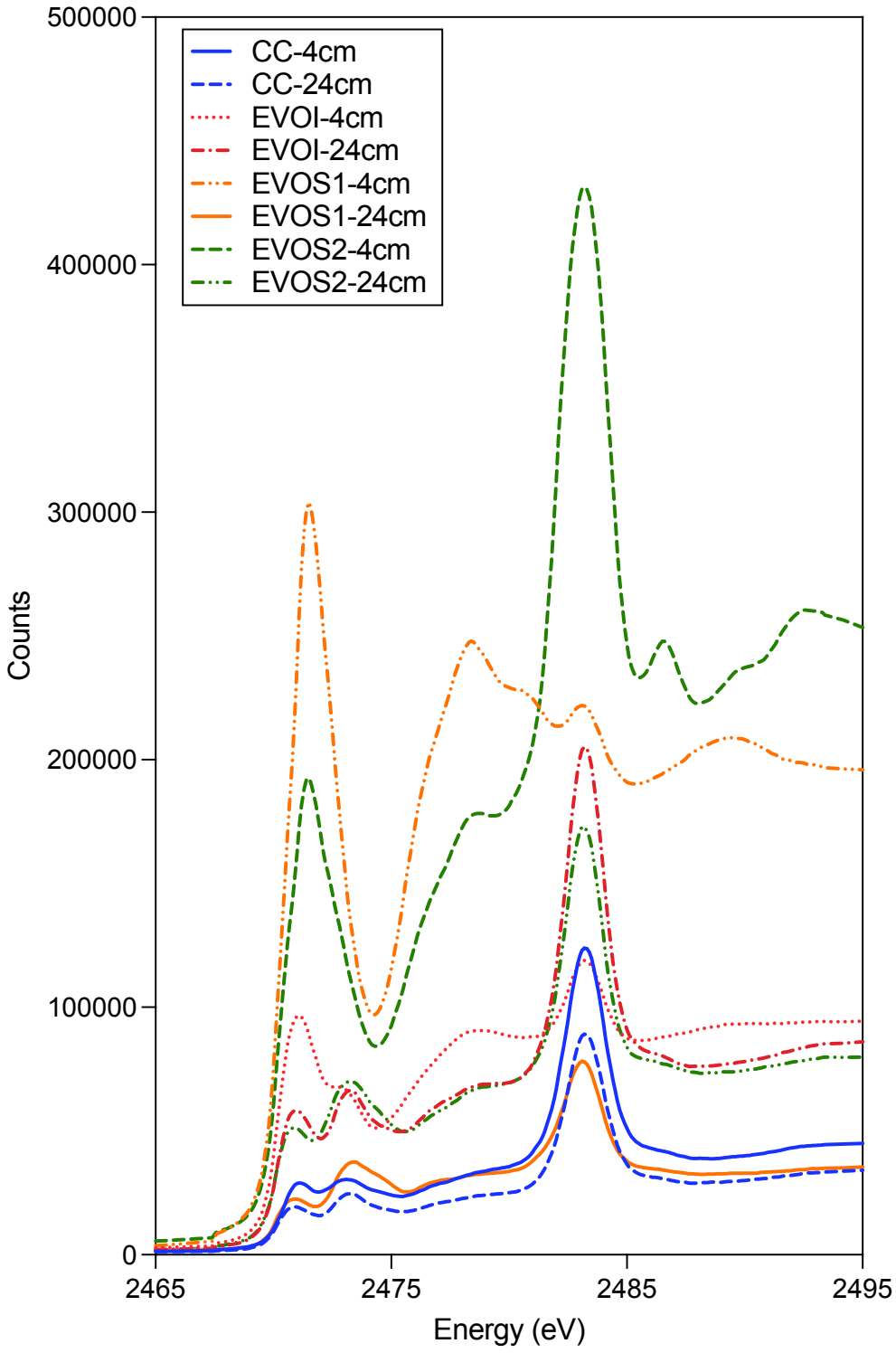


Figure B6. Raw counts of bulk S XANES spectra of samples collected from the column experiments during the experiment.

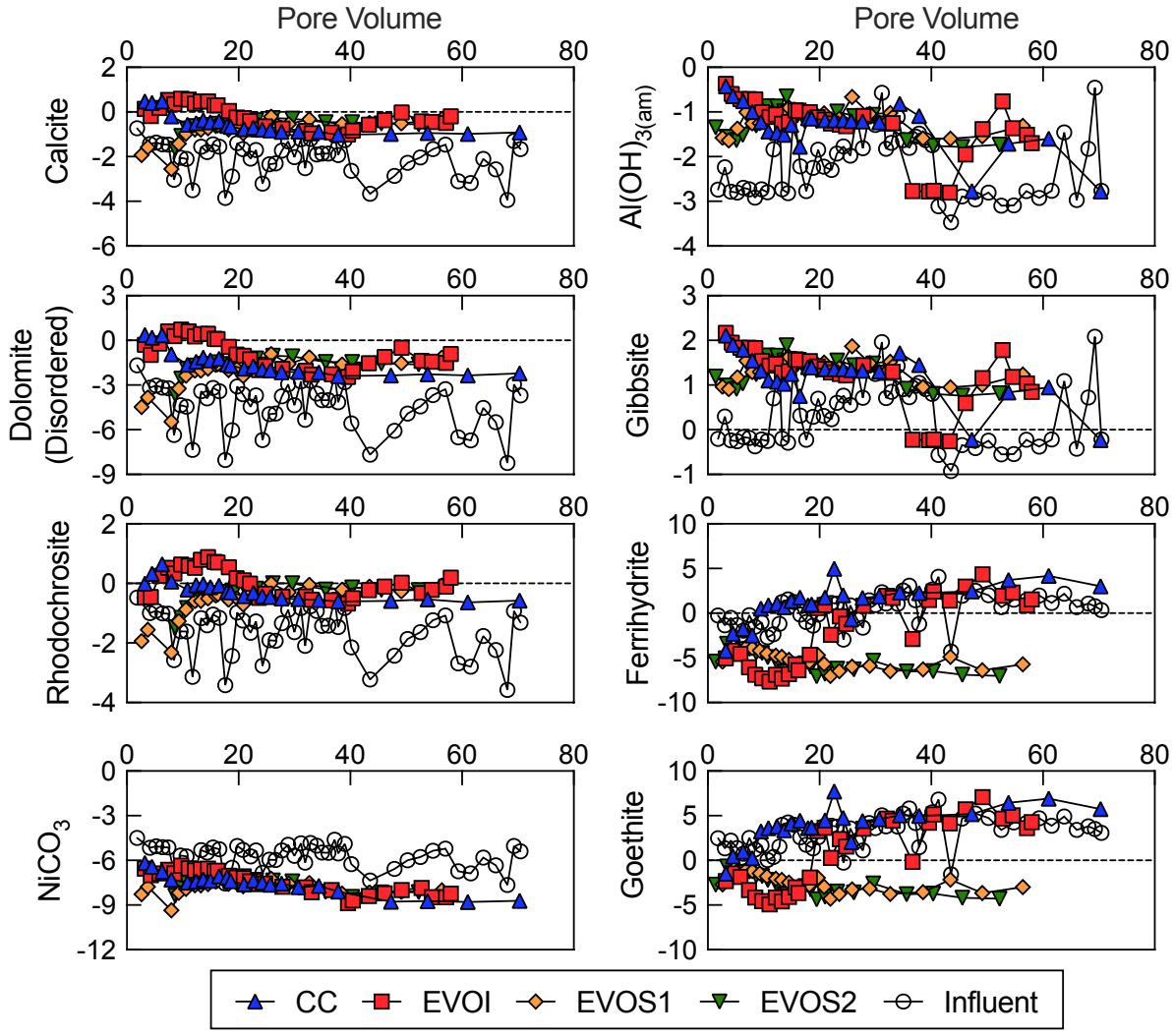


Figure B7. Saturation indices calculated for column effluent and influent samples using PHREEQC and the Minteq V4 database for secondary reaction products. Columns and influent are differentiated by color and shape. Samples with percent error > 20% (n = 5) and SI = -999.999 were not plotted.

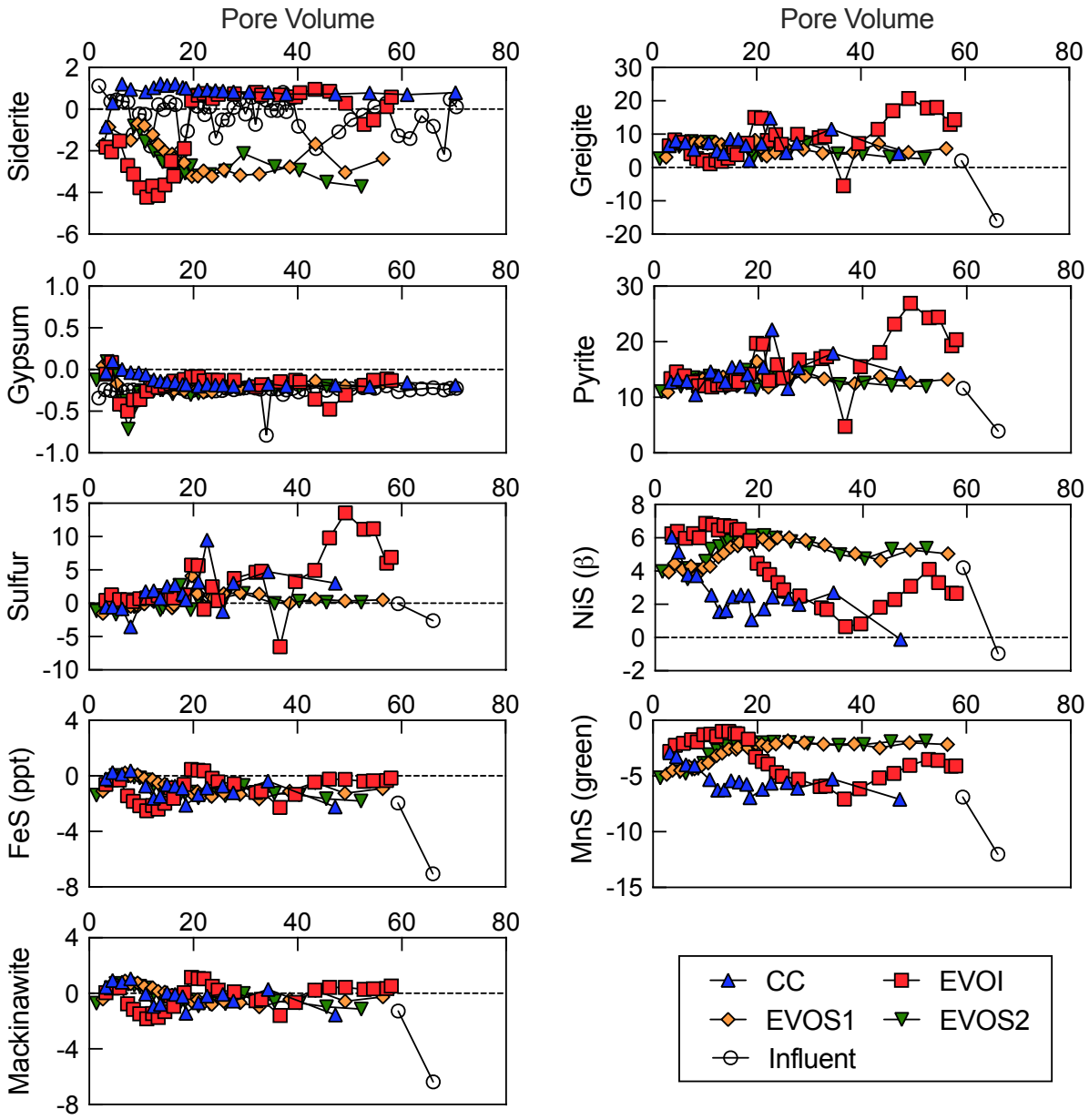


Figure B8. Influent and effluent sample saturation indices calculated using the PHREEQC database and Minteq V4 database for siderite, gypsum, elemental S and sulfide phases. The columns and influent are differentiated by different colors and shape. Samples with percent error > 20% (n = 5) and SI = -999.999 were not plotted.

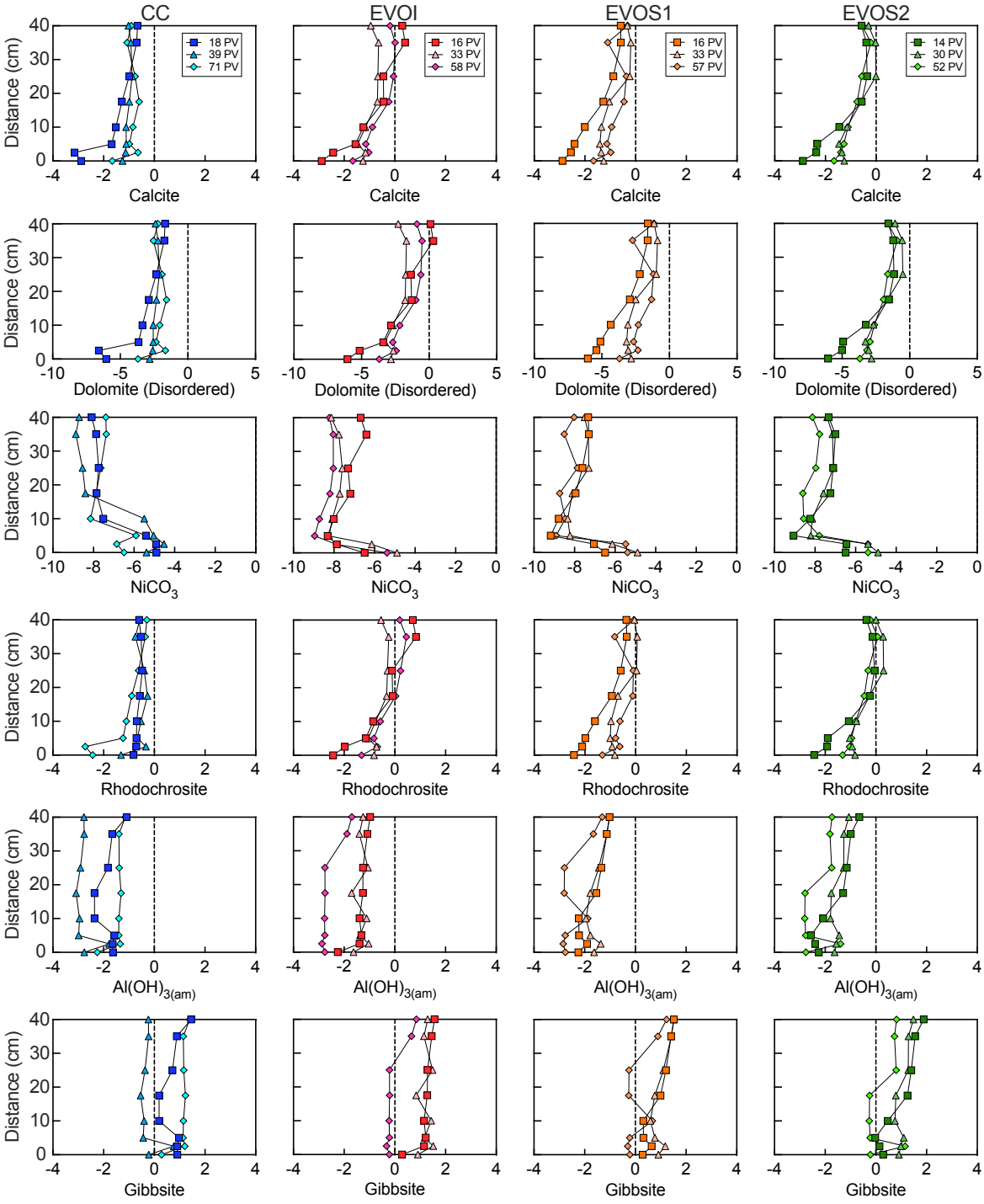


Figure B9. Column profile sampling saturation indices calculated using PHREEQC and Minteq V4 database for secondary reaction products. The three profile sampling events are plotted for each column and geochemical parameter. Within each plot sampling events are differentiated by shape and color shade. Samples with percent error > 20% (n = 5) and SI = -999.999 were not plotted.

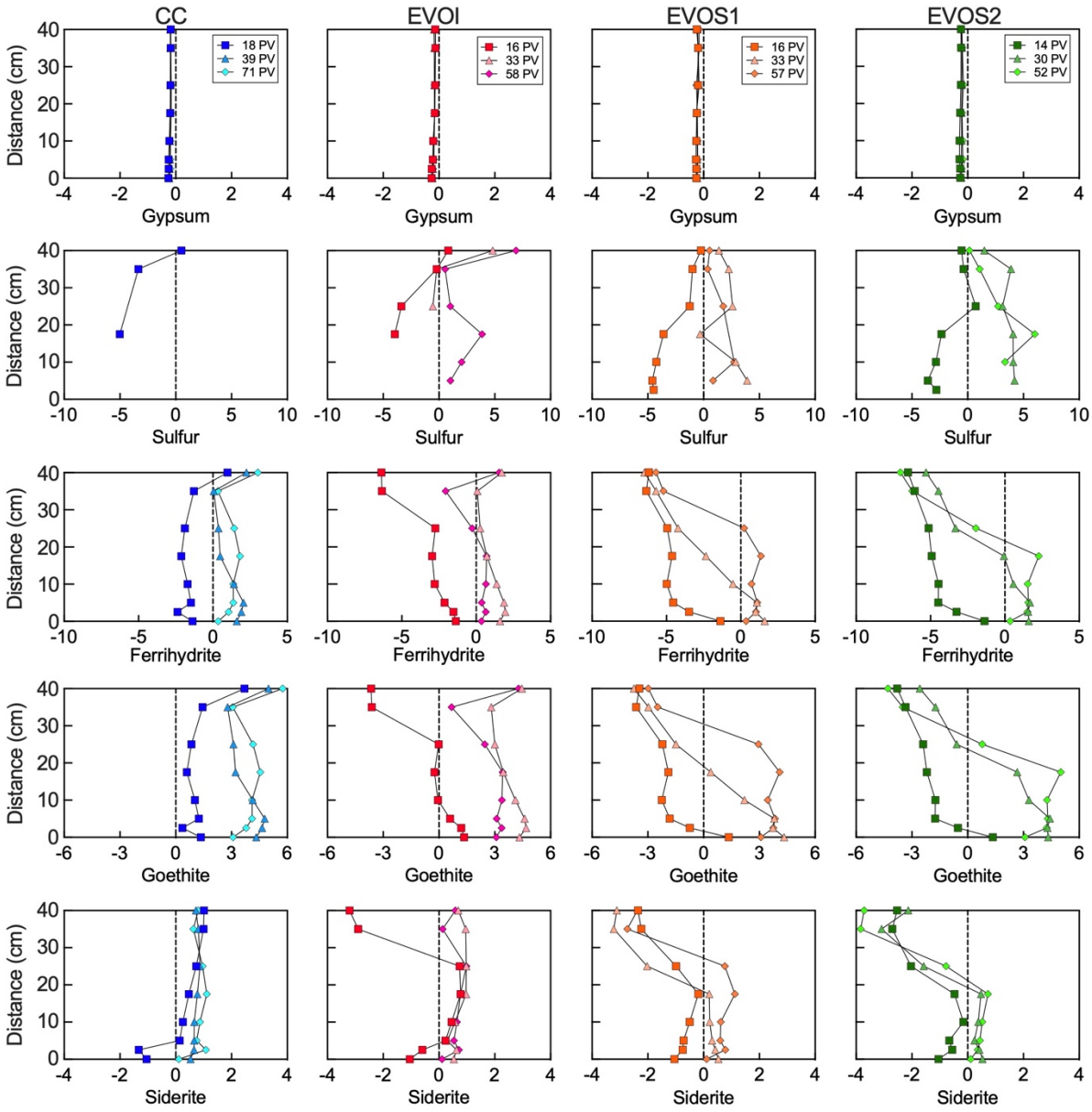


Figure B10. Column profile sampling saturation indices calculated using PHREEQC and Minteq V4 database for reaction products. The three profile sampling events are plotted for each column and geochemical parameter. Within each plot sampling events are differentiated by shape and color shade. Samples with SI=-999.999 were not plotted.

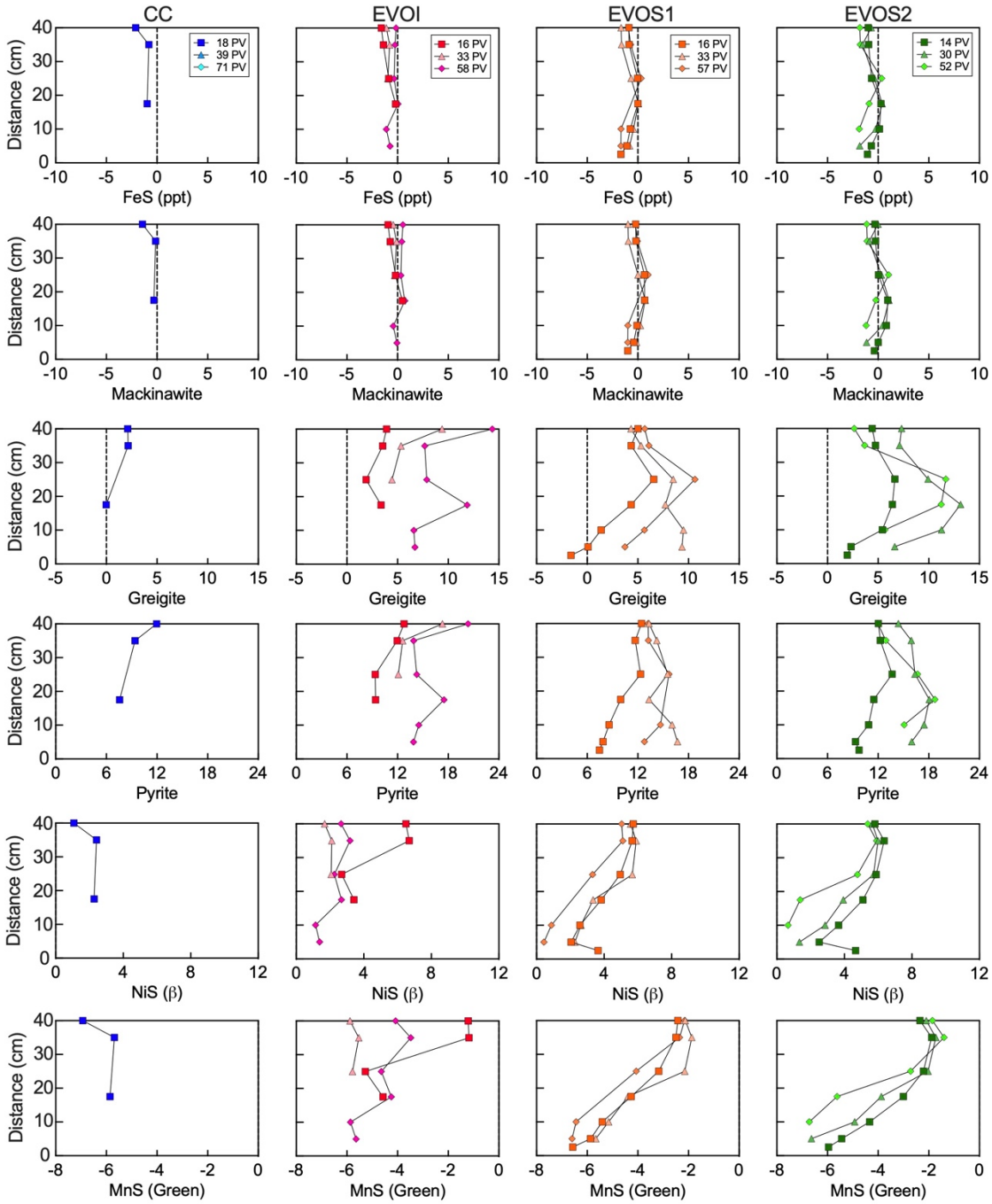


Figure B11. Column profile sampling saturation indices calculated using PHREEQC and Minteq V4 database for sulfide phases. The three profile sampling events are plotted for each column and geochemical parameter. Within each plot sampling events are differentiated by shape and color shade. Samples with SI = -999.999 were not plotted.

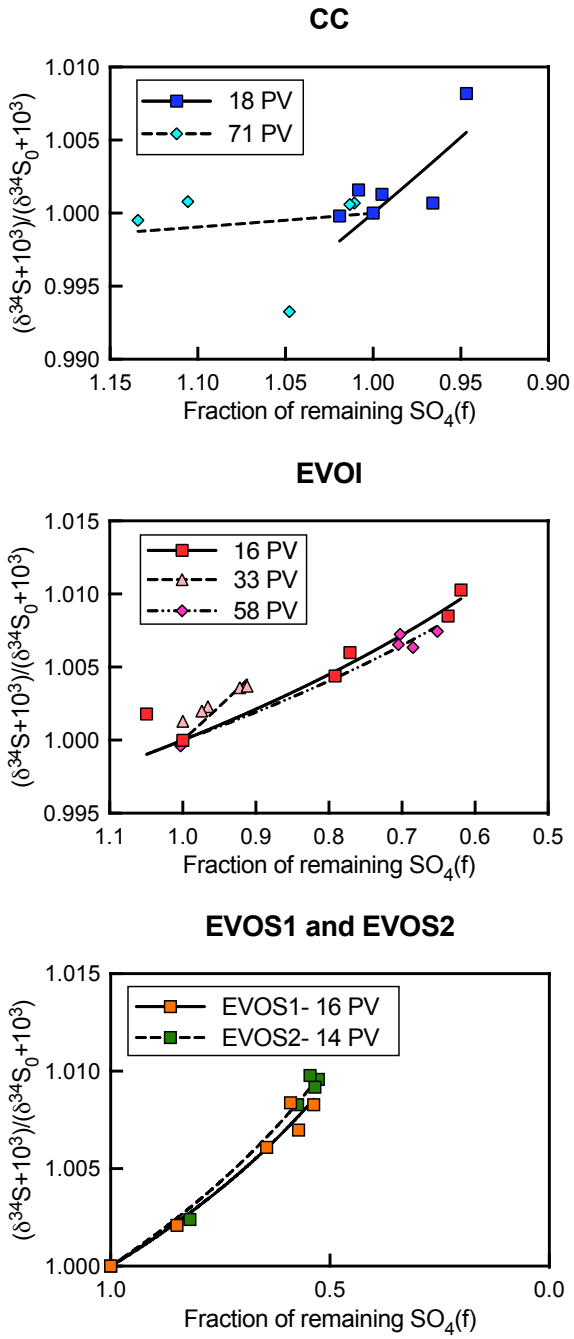


Figure B12. $(\delta^{34}S+10^3)/(\delta^{34}S_O+10^3)$ *vs.* fraction of remaining SO_4. $\delta^{34}S_O$ and $\delta^{34}S$ are the $\delta^{34}S$ of the influent and pore-water samples taken along the column length, respectively. The best-fit curves are used to calculate the instantaneous fractionation factor (α; Guo & Blowes, 2009**)**.

Table B8. Comparing the best linear combination fitting (LCFs) results of S XANES spectra for samples where pyrite was included in the best fit results. Spectra for standards used in LCF fitting are shown in Figure 3.11.

Sample ID	Fit #	χ^2	χ^2 Reduced	Gypsum	Ferrous Sulfate	K-Tetrathionate	Na-Sulfite	Na-Thiosulfate	Cysteine	Elemental S	Pyrite	FeS	Total
CC-S2	1	8.75	0.03	0%	43%	0%	0%	0%	13%	0%	7%	37%	100%
	2	8.73	0.03	2%	42%	0%	0%	0%	13%	0%	7%	36%	100%
	3	8.78	0.03	0%	44%	0%	0%	0%	12%	5%	0%	39%	100%
	4	8.75	0.03	3%	42%	0%	0%	0%	11%	5%	0%	38%	100%
	5	8.73	0.03	2%	42%	0%	0%	0%	13%	1%	6%	36%	100%
EVOI-S2	1	1.70	0.01	17%	0%	0%	0%	0%	0%	0%	2%	82%	100%
	2	1.71	0.01	17%	0%	0%	0%	0%	0%	0%	0%	83%	100%
	3	1.71	0.01	17%	0%	0%	0%	0%	0%	1%	0%	83%	100%
	4	1.71	0.01	17%	0%	0%	0%	0%	0%	0%	0%	83%	100%
	5	3.70	0.01	0%	9%	0%	0%	0%	0%	0%	3%	88%	100%
EVOS1-S2	1	4.79	0.02	0%	0%	0%	2%	13%	0%	0%	14%	71%	100%
	2	4.87	0.02	0%	0%	0%	0%	15%	0%	0%	13%	73%	100%
	3	5.55	0.02	0%	0%	0%	1%	15%	0%	4%	0%	79%	100%
	4	5.58	0.02	0%	0%	0%	0%	16%	0%	4%	0%	80%	100%
	5	5.55	0.02	0%	0%	0%	1%	15%	0%	4%	0%	79%	100%
EVOS2-S2	1	0.819	0.003	36%	4%	0%	1%	3%	0%	0%	9%	47%	100%
	2	0.848	0.003	36%	4%	0%	0%	4%	0%	0%	8%	47%	100%
	3	0.884	0.003	35%	5%	0%	2%	0%	0%	0%	10%	49%	100%
	4	0.929	0.003	41%	0%	0%	1%	4%	0%	0%	9%	44%	100%
	5	0.964	0.003	41%	0%	0%	0%	6%	0%	0%	8%	45%	100%
	6	0.984	0.003	35%	5%	0%	0%	0%	0%	0%	9%	51%	100%
	7	1.049	0.004	37%	4%	0%	1%	4%	0%	4%	0%	50%	100%
	8	1.062	0.004	37%	4%	0%	0%	5%	0%	3%	0%	50%	100%

Table B9. Calculated instantaneous fractionation factor (α) and enrichment factor (ε) for different column pore-water sampling events using Rayleigh fractionation model (Guo & Blowes, 2009). The goodness-of-fit is described by the coefficient of determination (R^2).

Column and Sampling Event	α	ϵ(‰)	R^2
CC- 18 PV	0.899	-100.9	0.41
CC- 71 PV	0.990	-9.9	0.04
EVOI- 16 PV	0.980	-20.1	0.88
EVOI- 33 PV	0.955	-44.7	0.69
EVOI- 58 PV	0.982	-18.1	0.98
EVOS1- 16 PV	0.986	-13.7	0.97
EVOS2- 14 PV	0.985	-15.0	0.99

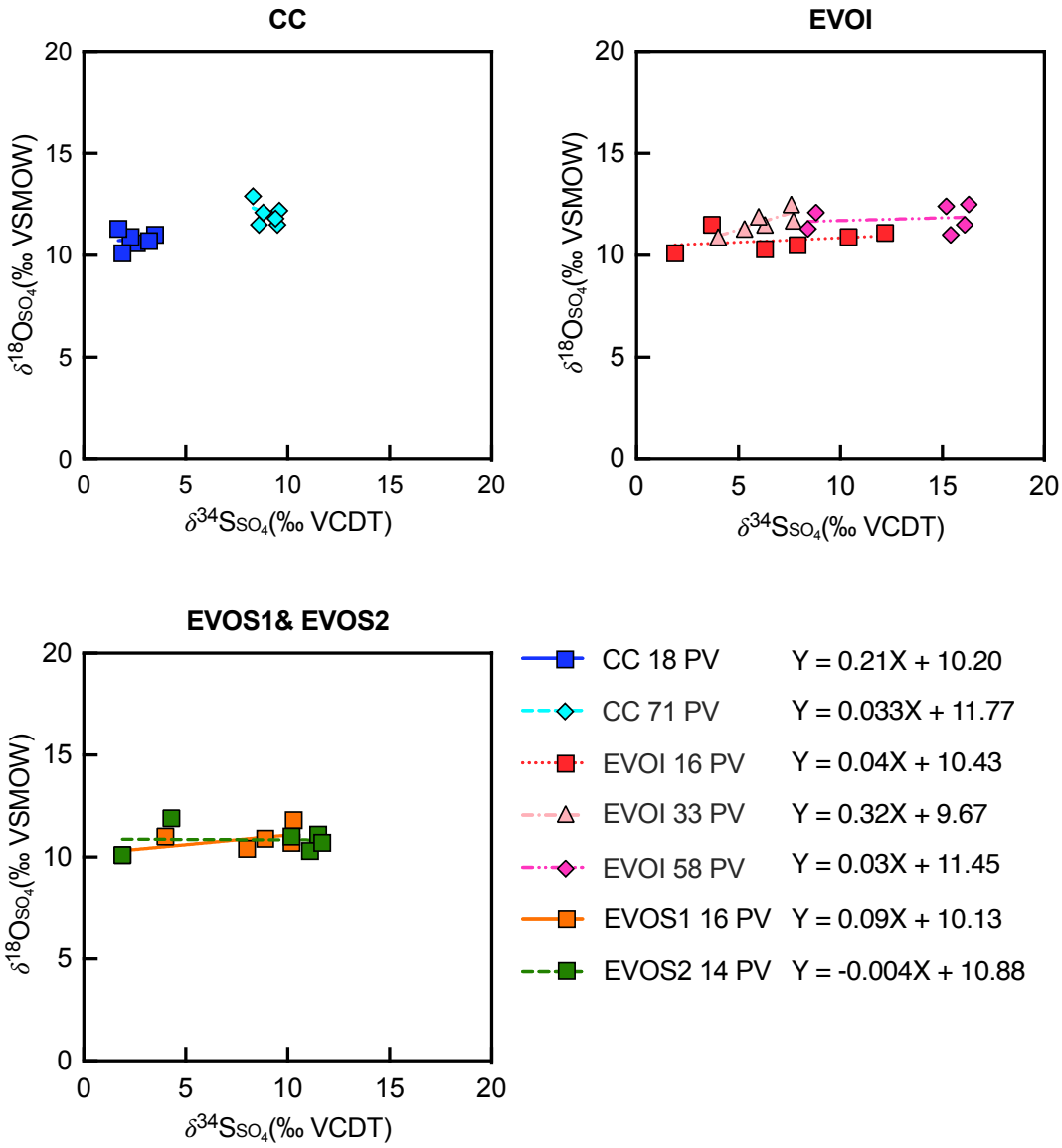


Figure B13. Aqueous sulfate $\delta^{34}S$ and $\delta^{18}O$ cross-plots of samples collected from influent effluent and pore-water. Samples from CC, EVOI and EVOS columns are grouped in individual plots for comparison. Each column profile sampling event is represented by a different color and shape. Each sampling event was fit with a simple linear regression and equations of these fits are shown.